Summer 2021

Colloidal Semiconductor Quantum Dots: Solution Processing and Heterostructure-Based Optoelectronics

Mathew L. Kelley

COLLOIDAL SEMICONDUCTOR QUANTUM DOTS: SOLUTION PROCESSING AND HETEROSTRUCTURE-BASED OPTOELECTRONICS

by

Mathew L. Kelley

Bachelor of Science
Appalachian State University, 2016

Master of Science
University of South Carolina, 2018

Submitted in Partial Fulfillment of the Requirements

For the Degree of Doctor of Philosophy in

Chemistry

College of Arts and Sciences

University of South Carolina

2021

Accepted by:

Andrew B. Greytak, Major Professor

Dmitry V. Peryshkov, Committee Member

Donna A. Chen, Committee Member

M.V.S. Chandrashekhar, Committee member

Tracey L. Weldon, Interim Vice Provost and Dean of the Graduate School

DEDICATION

I dedicate this thesis to my family, including those who were unable to see the end of this journey. I am nothing without you. I thank you endlessly for all of the wonderful opportunities, support, and encouragement for continuous learning and curiosity. Thank you.

ACKNOWLEDGEMENTS

First, I must give infinite thanks to my thesis advisor, Dr. Andrew B. Greytak, for his helpful advisement and inspiration throughout the duration of my graduate career. I am very grateful for all of the opportunities to learn and collaborate on a multitude of interdisciplinary research projects with talented teams. I could not have asked for a richer research experience. In addition, I must give thanks to my co-advisor, Dr. M.V.S. Chandrashekhar, for his unwavering guidance, insights, and patience along the way. It has been a true privilege working with you and your research team. I am also very thankful to Dr. Donna A. Chen and Dr. Dmitry V. Peryshkov for their support and valuable insights. Thank you all very much for your time!

Immense thanks must also go to all members of the Greytak lab for their endless support, collaborative contributions, and sense of humor. In no specific order: ***Thank you*** Dr. Bobby Barker, Dr. Megan Gee, Dr. Adam Roberge, Dr. Preecha Kittikhunnatham, Fiaz Ahmed, Sakiru Abiodun, Nuwanthaka Jayaweera, John Dunlap, and Cole Love-Baker. I am very grateful for your enthusiasm and mastery of cultivating a positive environment for learning and growth. I also thank Dr. Yi Shen for his helpful advice and insights. I also thank Josh Letton, Kamal Hussain, and Mohi Uddin Jewel for their collaborative expertise and contributions to this work. This work could not have been completed without you all!

Many thanks must also be given to my IGERT internship host, Dr. Sohee Jeong. I am very humbled to have had the opportunity to work with your research team and

collaborate with Dr. Munseok Jeong and Dr. Wan Ki Bae's research teams. ***Thank you*** Dr. Hyekyoung Choi, Dr. Ju Young Woo, Dr. Taewan Kim, Dr. Anh Nguyen, Dr. Hyojung Kim, Dr. Joongpill Park, Dr. Byeong Guk Jeong, Youngsik Kim, Yujeong Jung, Seongmin Park, Youngsang Park, Byunghui Yoon, Mahnmin Choi, Hamin Kim, Jueun Han, and Youngwook Chung. It was a pleasure to have met you all and I am eager to see what you all do in the future!

I am also very appreciative of the wonderful people that I had to opportunity to meet during my graduate career. ***Thank you*** Shelby Dickerson, Grace Hollenbeck, and Abby Waldron-Bush for your humor, support, and directness in telling me how it is. I wish you all the very best and cannot wait to see what awaits you after graduate school!

I am also thankful for support from Taylor Morris, Zachary Sherbondy, Connor Hamilton, Connor Kusilek, Raphael Rojas, and Dillon Carns along the way. I am very glad to have met you all and we have some serious catching up to do!

I must also thank Dr. Carol Babyak and the rest of the faculty at Appalachian State University for their guidance in preparing me for graduate studies. Thanks must also go to Steve Padgett, PhD for his advice on graduate school and professional endeavors as well.

A sincere and final thank you goes to all educators that I have had the opportunity to work with. ***Thank you*** for your time, patience, and inspiration.

ABSTRACT

Colloidal semiconductor quantum dots (QDs) are attractive candidates for high-efficiency solar cells and uncooled multiplexed photodetectors due to their favorable characteristics including large absorption cross-sections, size-tunable bandgap energies spanning the ultraviolet (UV) to short wave infrared, and solution processability. These QD-based optoelectronic devices operate on the basis of efficient photogenerated charge migration within QD solids and charge separation and recombination at electrical junctions, underscoring the need for (1) processing strategies that facilitate charge transport and (2) characterization techniques that robustly interrogate charge separation at QD interfaces. Here, my work on the post-synthetic processing and surface modifications of several semiconductor QDs, as well as investigations on charge transport and separation in a multitude of optoelectronic device architectures will be presented.

This thesis is divided into four parts. First, I introduce low dimensional materials and post-synthetic purification strategies en route to device fabrication. Second, I describe my work on the formation and study of novel PbS QD/epitaxial graphene/SiC (QD/EG/SiC) optoelectronic devices, where we electrically isolate and characterize previously unreported QD/SiC heterojunctions and achieve NIR responsivity due to the incorporation of NIR bandgap (~1300 nm) PbS QD films. Scanning photocurrent microscopy acquired with a home-built MATLAB GUI application reveals that the transfer length is the characteristic length scale for charge carrier collection across the QD/SiC interfaces, which allowed extraction of the QD film resistivity (~18 kΩ-cm) by

analyzing the QD/SiC junction as a lumped element transmission line. Thirdly, I introduce spatially resolved Fourier transform impedance spectroscopy as a novel technique to quickly build and map the frequency response of optoelectronic devices using optical probes. My collaborative work on environmentally benign QDs will then be discussed with focus on the formulation of ligand-exchanged AgBiS2 nanocrystal inks for photoconductive devices and the development of hybrid III-V QD/2D material phototransistors for amplified NIR detection. Finally, collaborative research on the hydrophobic self-assembly and uptake of visible bandgap, fluorescent QDs onto patterned magnetic nanoparticle templates will be described.

TABLE OF CONTENTS

LIST OF FIGURES

LIST OF ABBREVIATIONS

AC ..... Alternating Current

ATR-FTIR..... Attenuated Total Reflectance Fourier Transform Infrared

AFM ..... Atomic Force Microscopy

BJT ..... Bipolar Junction Phototransistor

BTU ..... British Thermal Unit

CAD ..... Computer-Aided Design

CNP ..... Charge Neutral Point

CVD ..... Chemical Vapor Deposition

DLTS..... Deep Level Transient Spectroscopy

DMF ..... *N,N*-dimethylformamide

EDX ..... Energy Dispersive X-Ray Spectroscopy

EG ..... Epitaxial Graphene

FTIS ..... Fourier Transform Impedance Spectroscopy

GPC..... Gel Permeation Chromatography

Gr ..... Graphene

GUI ..... Graphical User Interface

i-DLTS ..... Current Deep Level Transient Spectroscopy

I_{DS} ..... Drain-Source Current

IMPS ..... Intensity-Modulated Photocurrent Spectroscopy

IR..... Infrared

IS ..... Impedance Spectroscopy

L_T .....Transfer Length

MDH ..... Mixed-Dimensional Heterostructure

m_0 .....electron rest mass

m_e .....electron effective mass

MeOAc.....Methyl Acetate

m_h .....hole effective mass

ML.....Monolayer

NIR.....Near Infrared

NMR ..... Nuclear Magnetic Resonance

$NOBF_4$..... Nitrosonium tetrafluoroborate

NP .....Nanoparticle

ODE 1-octadecene

PCR.....Precipitation-Centrifugation-Resdispersion

PMMA .....Poly(methyl methacrylate)

PPL..... Polymer Pen Lithography

PT .....Phase Transfer

QD.....Colloidal Quantum Dot

SEM .....Scanning Electron Microscopy

SPCM.....Scanning Photocurrent Microscopy

SSLE .....Solid State Ligand Exchange

TDPA ..... tetradecylphosphine

TEM ..... Transmission Electron Microscopy

TLM ..... Transmission Line Model

UV ..... Ultraviolet

UPS ..... Ultraviolet Photoelectron Spectroscopy

V_{bi} ..... Built-in Voltage

V_{GS} ..... Gate-Source Current

VPS ..... Vacuum Probe Station

WBG ..... Wide Bandgap

W_D ..... Depletion Width

XPS ..... X-ray Photoelectron Spectroscopy

CHAPTER 1: INTRODUCTION

1.1: ENERGY DEMANDS AND AN INTRODUCTION TO COLLOIDAL QUANTUM DOTS

As energy consumption continues to increase, the urgency to develop innovations that meet and exceed them rises in parallel. Although energy consumption from petroleum and coal demonstrated slight decreases associated with the global COVID-19 pandemic, energy consumption in the Unites States is projected to increase in the approaching decades (**Figure 1.1**). Steady rises in natural gas and renewable energy sources including solar, wind, and geothermal are anticipated to accompany declines in electricity generated from coal.[1] Notably, within the renewable energy sector, solar energy is projected to lead electricity generation in the Unites States through the year 2050: nearly half (47 %) of all total renewable energy generation is expected to originate from solar, with wind coming in second at 34 %.[1] Given recent growth and anticipated utilization of solar energy technologies in the near future, it would be prudent to further develop existing solar technologies to maximize performance and minimize production costs.

Currently, commercial solar photovoltaic technologies are dominated by silicon (Si) based devices, but there are key opportunities to improve them. For example, the semiconductor bandgap of Si is 1.1 eV (1120 nm), which almost completely renders the near infrared (NIR) portion of the sun's spectral irradiance inaccessible because photons below the Si bandgap are not absorbed. Tandem solar cells that incorporate a second

and/or third solar cell with materials of different bandgap energies from Si may be used to overcome spectral limitations of Si, but current matching between must be optimized

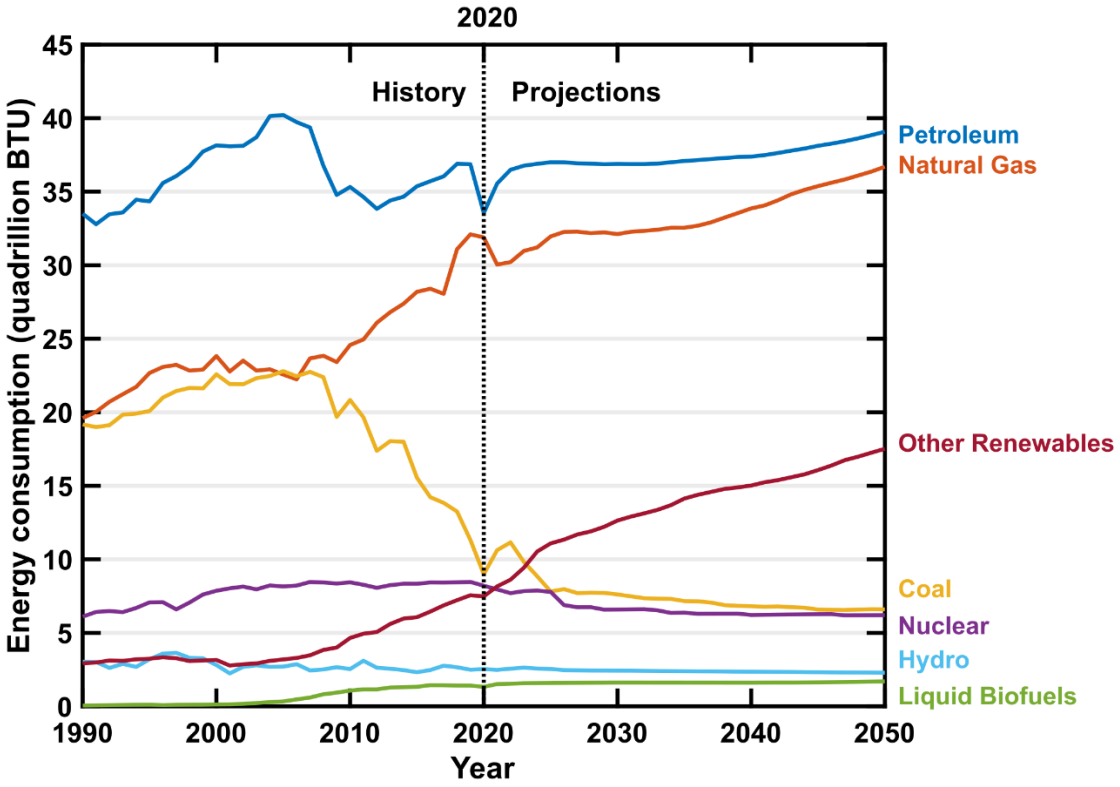

Figure 1.1: Reported and projected energy consumption by fuel for the United States. Data obtained from the U.S. Energy Information Association.[1] BTU is British Thermal Units.

to ensure maximal power conversion and the additional cells pose nontrivial fabrication complexities. In addition, the preparation of Si for solar energy conversion requires costly high purity and high temperature fabrication conditions, and it would be highly advantageous to mitigate the energetic burdens associated with these challenges.

There is also motivation to develop materials beyond silicon in electronic and optoelectronic device areas other than solar photovoltaics (e.g. thin film transistors, photodetection). Indeed, silicon currently dominates electronic and optoelectronic device

domains, and the same challenges associated with photovoltaic devices are encountered. Taking these factors into consideration, novel solution processed materials such as organic semiconductors, perovskites, and colloidal semiconductor quantum dots are attractive materials to fulfill these application needs and exploit exotic emergent properties for realms previously inaccessible with silicon including flexible, transparent, and freeform devices.[2] Organic semiconductors offer optical transparency and tunable bandgap energies, but their long term stability and charge transport characteristics are currently limited. Perovskites offer excellent charge transport and perovskite-based solar cells have demonstrated exceptionally rapid growth in recent years, but the stability of current state-of-the-art devices challenges widespread deployment. On the other hand, colloidal semiconductor quantum dots (QDs) offer spectral accessibility beyond silicon, solution processability, and charge carrier mobilities comparable to organic semiconductors.[3] These tradeoffs in merits favor QDs over other novel materials and make them prime candidates for electronic and optoelectronic spaces beyond silicon. Here, a brief introduction to QDs and processing steps along the way to device fabrication will be presented.

QDs are nanoscale particles composed of an inorganic, crystalline semiconductor core terminated by surface ligands that preserve the colloidal stability in solution-phase dispersions. It is noted that epitaxial QDs are another type of QD, but all references to QDs within this work pertain to colloidal QDs. The small size of QDs compared to bulk semiconductor phases induces quantum confinement of electrons and holes, which gives rise to deviations in the electronic structure. The characteristic length scale for confinement is dictated by the exciton Bohr radius (a_B), which is dependent on properties

that are specific to a semiconductor such as the dielectric constant and the effective masses of the electrons (m_e) and holes (m_h).[2] The relationship between a_B and these parameters is displayed in **Equation 1**, where ϵ is the dielectric constant, m_0 is the rest mass of electrons, μ is the reduced mass of an electron-hole pair, and a_o is the Bohr radius. **Equation 2** displays the relationship between μ, m_e, and m_h.

$$a_B = \frac{\epsilon m_0}{\mu} a_0 \quad (Equation\ 1)$$

$$\frac{1}{\mu} = \frac{1}{m_e} + \frac{1}{m_h} \quad (Equation\ 2)$$

Thus, the a_B of several commonly studied semiconductors for QDs is 18 nm for PbS, 5 nm for CdSe, 15 nm for InP, and 34 nm for InAs. Particles of size smaller than a_B are in

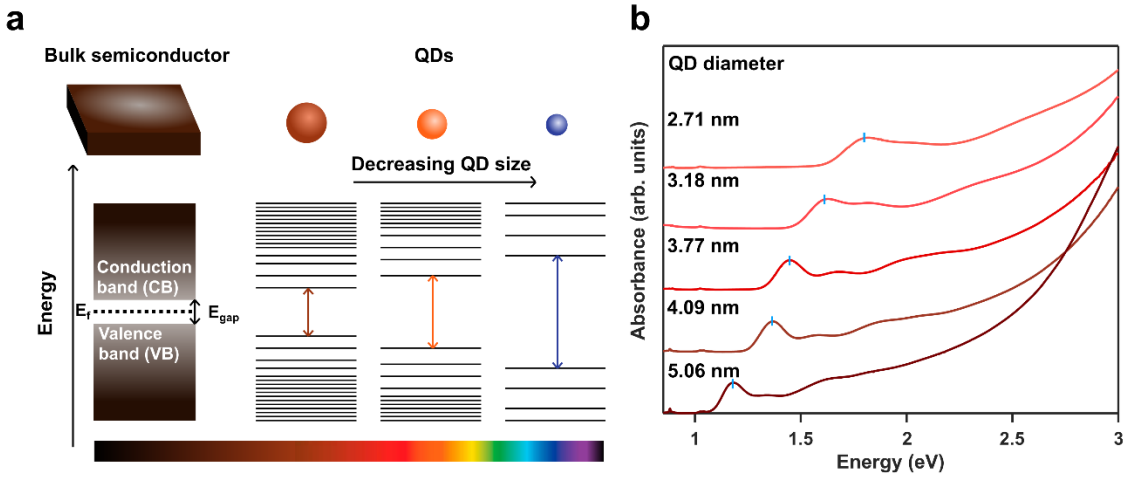

Figure 1.2: Quantum dot concept graphic. (a) energy band diagram for a semiconductor in the bulk and for corresponding QDs within the confinement regime. (b) absorbance spectra for InAs QDs showing the evolution of the effective bandgap with particle size. Blue ticks indicate the lowest energy excitonic peak maxima corresponding to effective bandgaps.

the strong confinement regime, which where the effects of quantum confinement dominate the electronic structure. This concept is shown graphically in **Figure 1.2**, where

the continuum of states in a bulk semiconductor's valence and conduction bands is replaced by discrete energy levels reminiscent of atomic orbitals. Because of the quantization effects, the effective bandgap of QDs is size-dependent and may be modified through synthetic control over the particle sizes. This effect may be visualized conceptually in the optical absorbance spectra shown in **Figure 1.2**, where the evolution of the lowest energy excitonic absorption peak with particle size is shown for a InAs QDs and indicates tunability in the effective bandgap over the NIR wavelength regime. This control over the effective bandgap energy also engenders flexibility in the emission profile of QDs, solidifying their applicability in technologies utilizing light absorption and emission.

In addition to the exotic optical properties showcased by QDs, solution-phase processing routes are appealing for low cost and large area fabrication. Following synthesis, QD films may be assembled through large scale means such as inkjet printing,

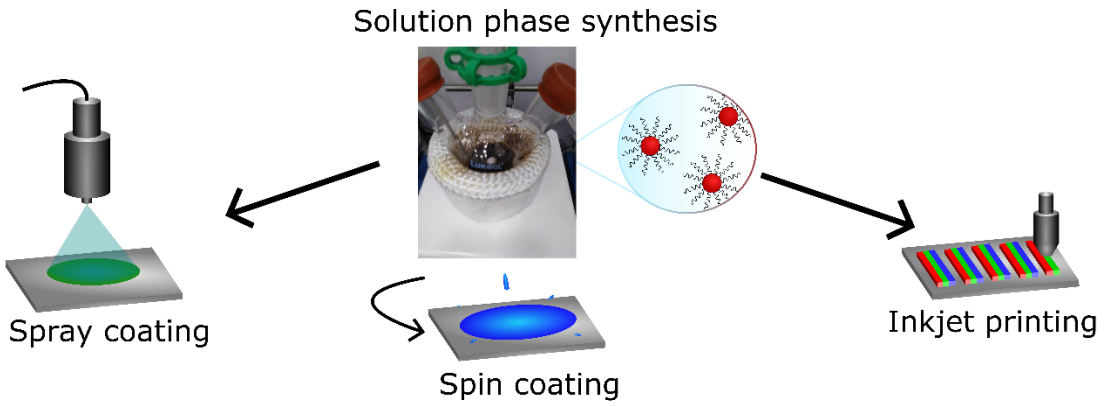

Figure 1.3: Assembly of quantum dot solids for devices. Center photo shows a representative laboratory glassware setup for the colloidal synthesis of InAs QDs using Schlenk line techniques.

spray coating, or roll-to-roll printing (**Figure 1.3**) or studied in laboratory prototype scales and deposited by spin coating, dip coating, or drop casting. This compatibility with

solution-processing techniques is favorable for forming standalone QD devices or incorporation with streamlined technologies.

All of these characteristics make QDs strong candidates for use in a variety of applications that underpin modern society including displays, photodetectors, and solar energy conversion devices, among others (**Figure 1.4**). In addition, emerging

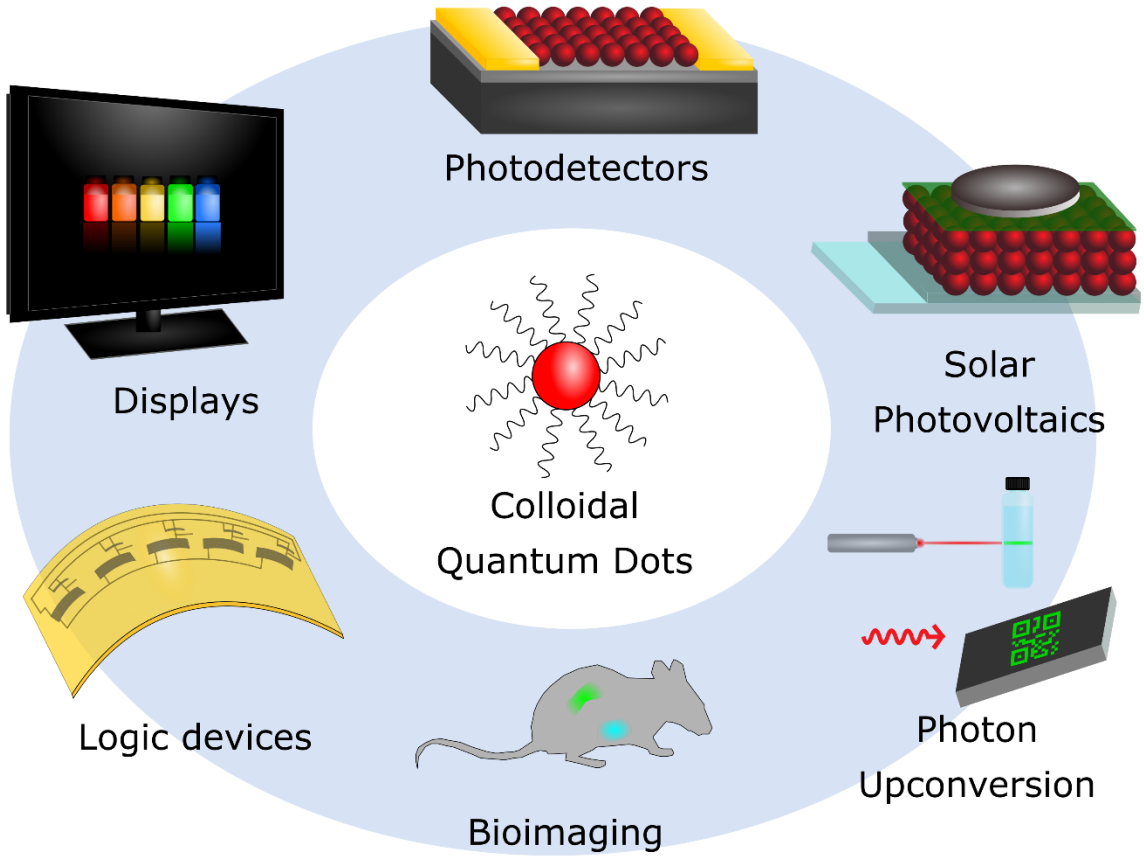

Figure 1.4: Concept graphic for various QD applications. Selected optoelectronic applications and emerging technologies featuring QDs are shown.

technologies such as flexible circuity, biological imaging, and photon upconverters may readily capitalize on the exotic properties of QDs. However, the road to device fabrication is a complex one, and several pathways may be undertaken to achieve

success. Here, the post-synthetic processing methods and film formation strategies used in this work will be introduced.

1.2: PURIFICATION OF COLLOIDAL QUANTUM DOTS BY GEL-PERMEATION CHROMATOGRAPHY

En route to device formation, post-synthetic purification of QDs is a post-synthetic processing step taken to eliminate extraneous molecular species such as residual growth solvent, unreacted precursors, impurities, and reaction byproducts.[4] QDs are typically synthesized in non-coordinating, high boiling point solvents such as 1-octadecene (ODE) to facilitate growth across a broad range of temperatures. These

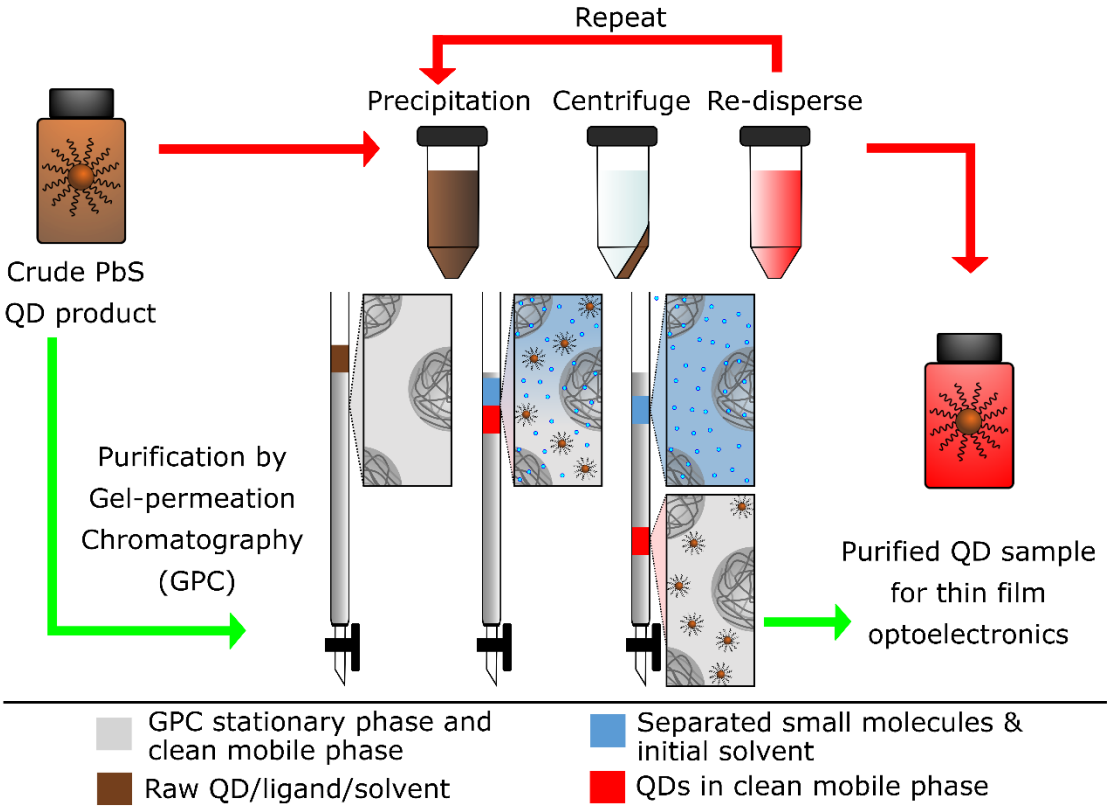

Figure 1.5: QD purification by liquid chromatography and precipitation methods. Green arrows indicate the pathway for GPC purification, and the red arrows indicate steps for conventional precipitation-based purification.

solvents are unsuitable for the deposition of uniform films, and in the case of ODE, serves as electrical insulators that will impede efficient charge transport.

Many methods exist and are used for the purification of QDs. Most commonly, a precipitation-centrifugation-redispersion (PCR) based method is undertaken to isolate QDs. The PCR method is undertaken by introducing antisolvent or poor solvent such as acetone, methanol, or methyl acetate that induces flocculation of QDs. The sample is then centrifuged, and flocculated QDs sediment while unwanted molecular species remain dispersed in the supernatant. The supernatant is discarded, and sedimented QDs are re-dispersed in a suitable solvent. This process is repeated iteratively (**Figure 1.5**) to obtain purified QDs. While effective, separation of QDs from undesired species by the PCR method can be challenged if the impurities hold similar solubilities to the QDs.[4] In addition, caution must be taken in the choice of antisolvent because harsh solvents may strip ligands from the surface of the QDs[5], which may compromise the colloidal stability and detrimentally alter the luminescent and electrical transport characteristics of QDs originating from the formation of surface dangling bonds.

To overcome these limitations, PbS QDs used in the work described in Chapters 2 and 3 were purified by gel-permeation chromatography (GPC).[4,6–8] GPC is a form of size-exclusion chromatography where separation is achieved on the basis of size. The separation of QDs from unwanted species is illustrated in **Figure 1.5**. Conceptually, QDs with nanometer scale cores are much larger than unwanted molecular impurities, and the relatively smaller molecular species are able to enter pores within the GPC media while QDs transit the void space between GPC media. The relatively longer path for molecular species translates to longer elution times and effective separation from QDs that elute on

shorter timescales. The method is repeatable[8,9] and may be conducted without successive changes in the solvent often required in PCR approaches. Proton nuclear magnetic resonance (NMR) spectroscopy confirmed the efficacy of the purification technique in isolating oleate-capped PbS QDs (**Figure 1.6**), as the separation of the QDs from the ODE growth solvent and unbound olefin species was achieved. In addition, the absorptive properties of the QDs were maintained after GPC purification, and a purified QD product suitable for film formation was generated.

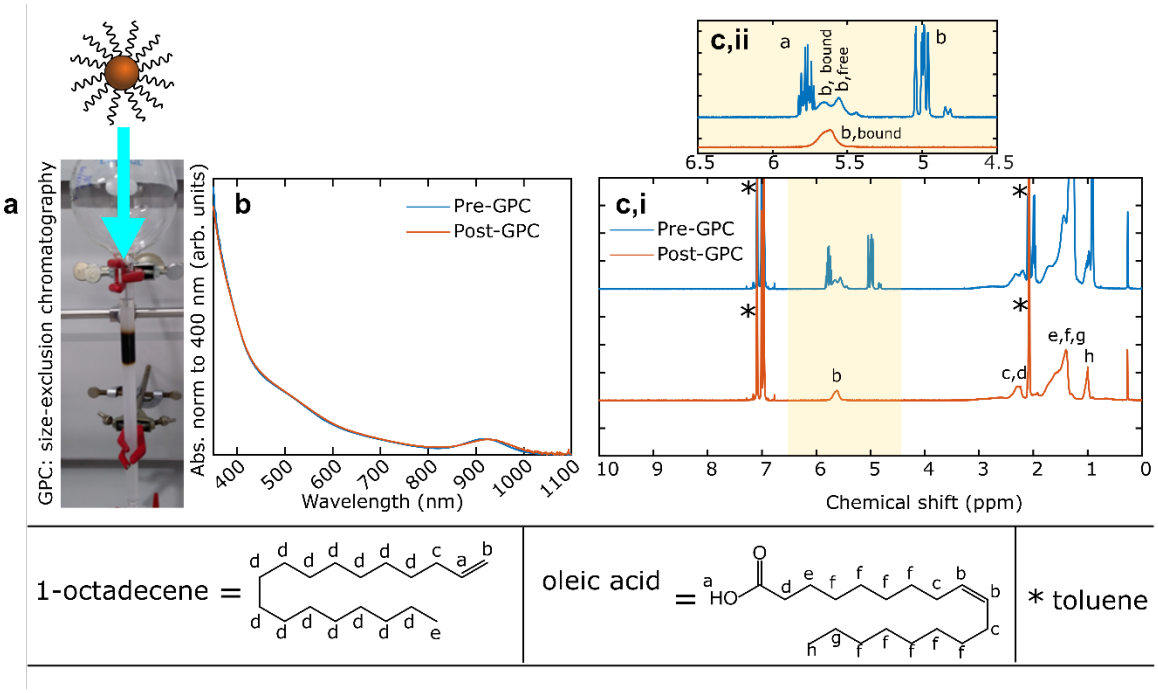

Figure 1.6: Purification of QDs by GPC. (a) GPC. (b) absorbance spectra. (c,i) shows NMR. (c,ii) shows closeup of olefin region. Bottom shows the legend for NMR resonances. Labels in (c,i) correspond to oleic acid. Sharp peaks a and b in (c,ii) refer to 1-octadecene, and remaining labels are oleic acid. The star indicates solvent resonances.

1.3: ASSEMBLY OF QUANTUM DOT SOLIDS FOR DEVICES

Efficient charge transport in QD films is necessary to minimize recombination losses that hinder the performance of solar photovoltaics and photodetectors. Typically, following the purification of QDs the long chain, electrically insulating ligands are

replaced in a ligand exchange reaction to reduce the interparticle spacing, increase dot-to-dot electronic coupling, and facilitate charge transport.[10] For the collaborative work described in chapters 2 and 3, a layer-by-layer solid state ligand exchange (SSLE) protocol was conducted to exchange native oleate ligands with short chain, bidentate 1,2-ethanedithiol ligands at the surfaces of PbS QDs.[11,12] A schematic showing the general spin coating process is displayed in **Figure 1.7**. In brief, deposition of QDs directly to substrates forms a thin film of oleate-capped QDs. The addition of incoming ligand solutions promotes the exchange reaction, and subsequent rinsing steps relieve the sample of excess incoming ligand and unbound oleate ligands. This process is repeated iteratively to achieve multilayer exchanged QD films suitable for electronic and

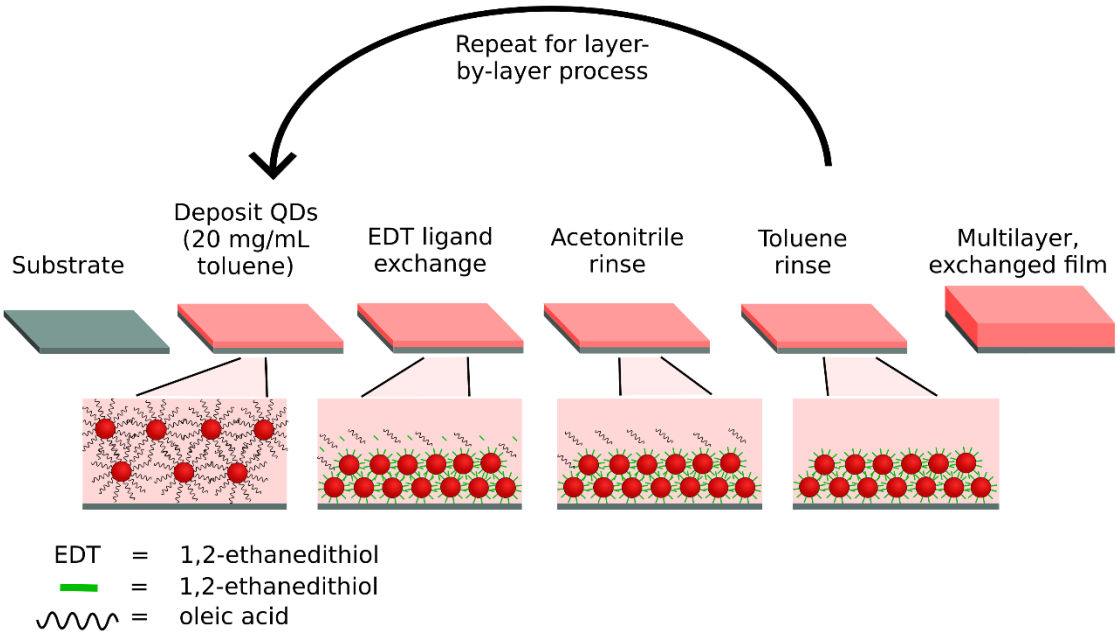

Figure 1.7: Solid-state ligand exchange flowchart for QD films.

optoelectronic device testing. Although SSLE processes are acceptable for laboratory scale prototypes, ligand exchange processes in solution that may be directly deposited to

form conductive QD layers are mandatory to realize commercial scale deployment. My work on formulating inks in this manner will be described in chapter 4.

Finally, for efficient electrical transport in QD solids, achieving smooth film morphologies free of cracks is necessary. Due to the stochastic formation of voids and cracks that form in SSLE processes as interparticle spacings are reduced, multiple layer cycles are conducted to successively infill the empty spaces. This also minimizes pathways for electrical shorts in vertical device geometries when evaporating top metal contacts to QD films. PbS QDs purified by GPC and exchanged with 1,2-ethanedithiol in a SSLE process similar to that illustrated in **Figure 1.7** yielded thin films with smooth morphologies as shown in the scanning electron microscopy images in **Figure 1.8**. This milestone confirmed that state-of-the art preparatory methods including GPC purification and dithiol ligand exchange protocols were suitable for device fabrication and characterization. Further details on the optimization of film assembly using GPC-purified

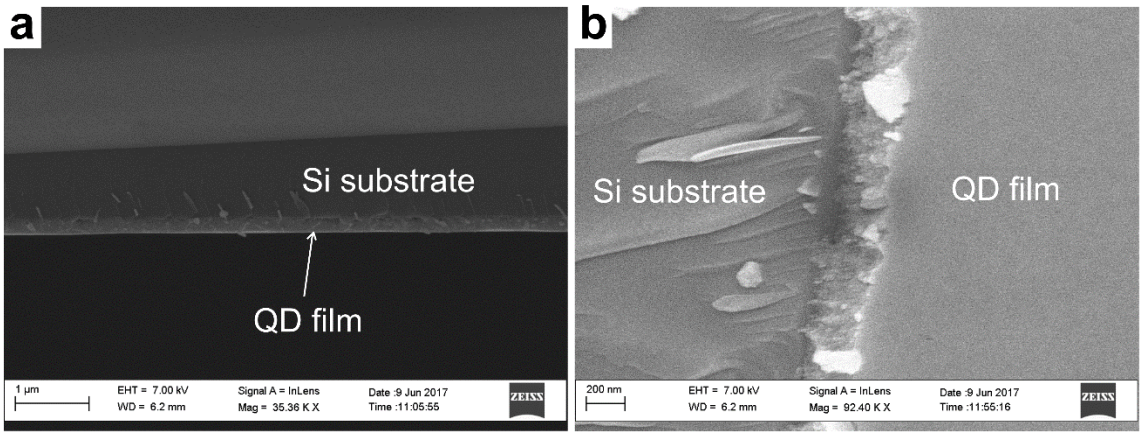

Figure 1.8: SEM images of GPC-purified, EDT exchanged PbS QD films. (a) cross-sectional SEM image. (b) off-angle SEM image of a QD film.

PbS QDs is discussed in my previous work.[6] The processing methods for GPC purification and SSLE film formation introduced here were applied to optoelectronic

studies described in **Chapter 2** and **Chapter 3**, where hybrid PbS QD/epitaxial graphene/SiC (QD/EG/SiC) devices were fabricated and characterized in detail.

1.4: DISSERTATION OVERVIEW

Overall, this thesis will introduce my work on QD-based optoelectronics in a variety of device architectures, the formulation of ligand-exchanged QD inks for photoconductor devices, and research efforts on QD self-assembly. Chapter 2 and chapter 3 will focus on collaborative work with Dr. M. V. S. Chandrashekhar's research team (UofSC, Electrical Engineering) where we fabricate and characterize novel QD/epitaxial graphene/SiC photosensors and develop a new technique to characterize composite interfaces using optical probes. Chapter 4 will describe research focusing on environmentally-benign QDs where we formulate ligand exchanged $AgBiS_2$ inks and study fundamental electronic properties of thin films deposited in a single step process. Collaborative work undertaken during my international internship at Sungkyunkwan University in Suwon, South Korea under the supervision of Dr. Sohee Jeong and Dr. Munseok Jeong (Department of Energy Sciences) will also be described, where we form InAs/graphene hybrid phototransistors for NIR detection. Finally, our collaborative work with Dr. Thomas Crawford's research team (UofSC, Physics) will be described, where we investigate the uptake and fluorescence characteristics of self-assembled QD arrays using magnetic nanoparticle templates.

CHAPTER 2: PHOTOVOLTAIC AND PHOTOCONDUCTIVE ACTION DUE TO PbS QDS ON GRAPHENE/SiC SCHOTTKY DIODES FROM NIR TO UV[1]

2.1: INTRODUCTION

This work describes the published results[7,13] of a research collaboration with the M.V.S. Chandrashekhar laboratory at the University of South Carolina. We demonstrate photovoltaic and photoconductive responses to NIR light in devices formed by depositing a film of GPC purified PbS QDs on top of n-SiC epitaxial layers with natively grown, low-leakage 10–15 monolayer thick EG Schottky contacts. The QD film layer was removable by selective chemical etching, resetting the EG/SiC Schottky diode: the sub-bandgap response could be restored in subsequent PbS-QD depositions. The EG in these devices simultaneously forms Schottky contacts to SiC and ohmic contacts to PbS-QD, enabling electrical screening and isolation of these interfaces from each other. After PbS-QD deposition, the diodes exhibit photovoltaic and photoconductive responses at photon energies far below the SiC bandgap, extending to the NIR gap of the QD film. Scanning photocurrent microscopy illustrates that this is due to charge transfer from the QD film to to the n-type 4H-SiC through a trap-limited, rectifying PbS-QD/SiC heterojunction with ideality n = 2 in parallel with the EG/SiC Schottky diode. The photoconductive gain at

[1] Reprinted with permission from Kelley, M. L.; Letton, J.; Simin, G.; Ahmed, F.; Love-Baker, C. A.; Greytak, A. B.; Chandrashekhar, M. V. S. Photovoltaic and Photoconductive Action Due to PbS Quantum Dots on Graphene/SiC Schottky Diodes from NIR to UV. ACS Appl. Electron. Mater. 2020, 2 (1), 134–139. https://doi.org/10.1021/acsaelm.9b00651.Copyright 2020, American Chemical Society.

this QD/SiC interface could be useful for IR detection in wide-bandgap platforms. Response times as fast as 40 ms are suitable for imaging applications, although careful contact design is required to optimize work-function matching and spreading resistance.

Colloidal semiconductor QDs such as PbS[14,15] notably demonstrate size-tunable luminescence and optical absorption with effective bandgaps spanning from violet to mid-infrared. These characteristics together with solution processability have sparked interest in QDs as the absorber in thin film and hybrid devices such as solar cells and infrared focal plane array detectors.[16] The most successful QD solar cell designs currently rely on photoinduced electron transfer across a heterojunction with a reducible (n-type) wide-bandgap (WBG) metal oxide (e.g., TiO2 or ZnO) as a key driver of charge separation. The demonstration of >10% efficiency in QD solar cells has shown the promise of this approach,[16,17] but open circuit voltages and short circuit currents remain below theoretical limits. It is thus important to consider junctions between QD films and other WBG semiconductors favorable for charge separation and strategies for making ohmic contacts for high carrier extraction. However, small variations in dimensional control and surface termination during the synthesis of QDs and formation of QD solids can have large effects on performance.[18,19]

The goal of this work was to investigate charge separation due to light at a wide bandgap SiC/PbS QD film interface. The introduction of narrow-gap materials such as PbS onto WBG materials is compelling as it introduces the potential for engineered near-infrared (NIR) optoelectronic functionality in WBG devices. By using spin-coated QD-films, we eliminate the need for the constraints of epitaxial registry in more traditional thin film crystal growth. Other nonepitaxial deposition techniques such as chemical vapor

deposition and sputtering also suffer from high cost and restrictions with material compatibility due to thermal budget and contamination issues.[20]

One challenge with electrical characterization of WBG/QD structures such as PbS-QD/SiC is the difficulty in forming reproducible contacts to composite materials such as the QD-film. Depending on the morphology of the PbS-QD film on SiC, contacts such as evaporated top metals have the potential to short through the QD films and create uncertainties in interpretation of optoelectronic data. Other challenges stem from uncertainties in the work function of the PbS-QD film. Depending on the ambient condition, the effective polarity of QD films with the same nominal surface termination can vary from n-type in vacuum photoelectron spectroscopy[21,22] to p-type after exposure to humid air.[11,12] There may also be carrier trapping at rectifying regions in the metal/QD film interface, leading to poor ideality.[23] These major issues present a serious challenge in the choice of metallization for characterization of QD/WBG heterojunctions.

We have recently explored optoelectronic properties of Schottky diodes and bipolar phototransistors based on the tetrafluorosilane (SiF4, TFS) grown contacts of epitaxial graphene (EG) on a SiC substrate to form a graphene/WBG interface.[24–26] These devices are sensitive to ultraviolet light based on the bandgap of 4H-SiC. Here, we demonstrate that these devices respond to NIR light as a direct consequence of the rectifying junction formed between the QD film and n-type 4H-SiC. The QD-graphene interface has been examined in other recent studies wherein charge transfer FETs built with QDs and exfoliated or deposited graphene[11,19] demonstrated an optical responsivity up to 10^8 A/W. The QD-graphene interface was also examined in similar devices utilizing single-layer epitaxial graphene (EG),[27–29] and additionally in barristor-type devices in

which the graphene–Si Schottky barrier height is modulated by charge transfer from QDs.[30,31] In many of these studies the varying carrier density in the graphene is the key mode of operation. However, the lone remaining junction of QD/WBG-SiC has not been isolated, partly due to the complexity of the interplay between the various junctions.

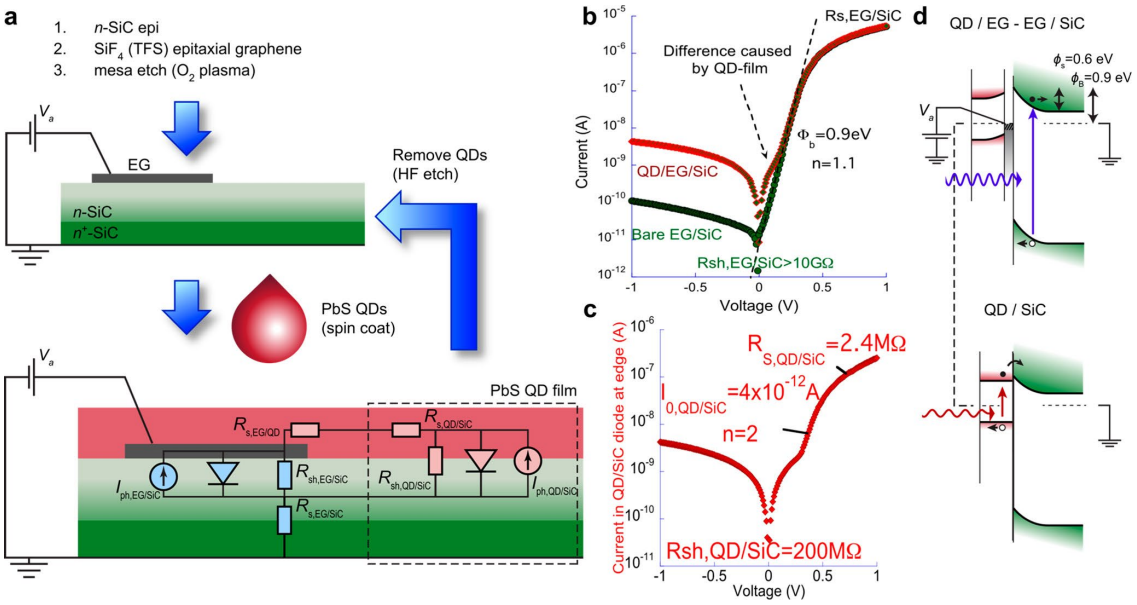

Figure 2.1: Device fabrication schematic and equivalent circuit diagram. (a) Device assembly and architecture indicating continuous QD film and n-SiC epilayer with patterned EG mesa. Superimposed is an equivalent circuit representation of the EG/SiC and QD/SiC interfaces indicating the spreading resistance of the QD film and shunt resistance contributed by the QD/SiC interface (dashed box). (b) Dark DC *I–V* characteristics for the bare and QD-coated devices. (c) Isolated QD/SiC junction *I–V* behavior. (d) Energy band diagrams of the constituent diodes shown in (a) illustrating ohmic contact between QDs and EG.

In this paper, we create spatially and electronically separated QD/EG and QD/SiC junctions to isolate the remaining PbS-QD/SiC interface. This enabled separate examination using localized illumination for scanning photocurrent microscopy (SPCM).[25,26] The architecture presented in **Figure 2.1** enabled us to exploit the following phenomenological observations to achieve this: (i) ohmic contacts of graphene to ethanedithiol (EDT)-capped PbS QDs in air, consistent with p-type conduction reported

previously,[32] which was also verified in the current work; (ii) a robust and ideal Schottky diode of EG/SiC[33] that is shown in this paper to be completely recoverable by selective chemical removal using hydrofluoric acid; (iii) a 10–15 monolayer (ML) EG film that achieves optical transparency for optoelectronic characterization,[25] while having a thickness greater than 1–2 ML screening length, such that electrostatic screening of the EG/SiC rectifying junction from the ohmic EG/PbS-QD film junction is achieved, precluding any potential barristor action.[30,31] This confluence of favorable conditions eliminates uncertainties stemming from the reproducibility of contacts between samples and between successive PbS-QD film depositions.

Our group has previously shown that gel permeation chromatography (GPC) is a precise and repeatable method for removing small molecule impurities from many types of QD samples.[8,34,35] Here, we employ GPC-purified PbS QDs to form spin-coated layers, in contrast to previous work on QD optoelectronic devices that has relied on precipitation and redissolution steps employing polar antisolvents.

2.2: RESULTS AND DISCUSSION

The device structure (**Figure 2.1a**) starts with EG/SiC Schottky diodes created by growing a homoepitaxial layer of n-type 4H-SiC, unintentionally doped to 1.6×10^{14} cm^{-3} on a n^+-SiC substrate by chemical vapor deposition (CVD) in a hot wall reactor with SiF4 and propane precursors in a hydrogen atmosphere, as described elsewhere.[36–39] Graphene was then formed natively on the previous homoepitaxial layer through exposure to SiF_s in an Ar atmosphere.[38] EG showed the key Raman peaks at ~1580, ~1350, and ~2650 cm^{-1} with a D/G ratio of ~0.1, indicating good quality. The thickness from X-ray photoelectron spectroscopy was ~15 monolayers.[36,40] Individual circular

device mesas with diameters ~250 μm were fabricated by using standard photolithography and O_2-plasma reactive ion etching.

PbS QDs with a diameter of ~4.5 nm and lowest energy exciton peak position at 1280 nm (~0.97 eV) (**Figure 2.2**) were synthesized by following Zhang et al.[14] Following

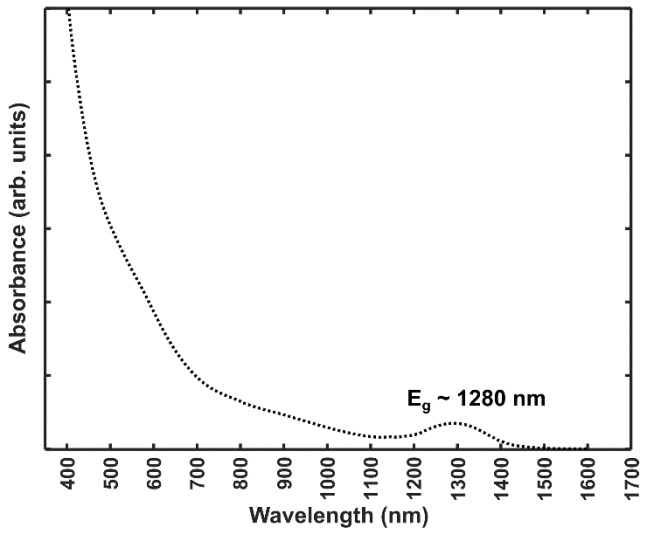

Figure 2.2: Representative absorption spectrum of purified PbS QDs in octane. The effective bandgap of ~1280 nm (E_g) is noted.

synthesis, the QDs, initially protected by alkyl carboxylate (oleate) surface coating, were purified by GPC.[8] A thin film was formed on the bare Schottky device by spin-coating, followed by in situ ligand exchange with ethanedithiol (**Figure 2.3**)[41] in a N2-filled glovebox. Following QD film deposition, contact was made to EG by locally puncturing the film with a tungsten probe tip and contact to the n^+-SiC substrate as made by using carbon tape.

The resulting film had a thickness of 90 nm, determined from atomic force microscopy (AFM). Fourier-transform infrared spectroscopy was employed to confirm removal of the initial oleate ligand coating as has been reported previously for EDT solid-

state exchange.[11,41,42] We found the QD film could be removed using 51% aqueous hydrofluoric acid and a new QD-film re- spun with qualitatively reproducible results (**Figure 2.5c**) where the device responsivity at photon energies

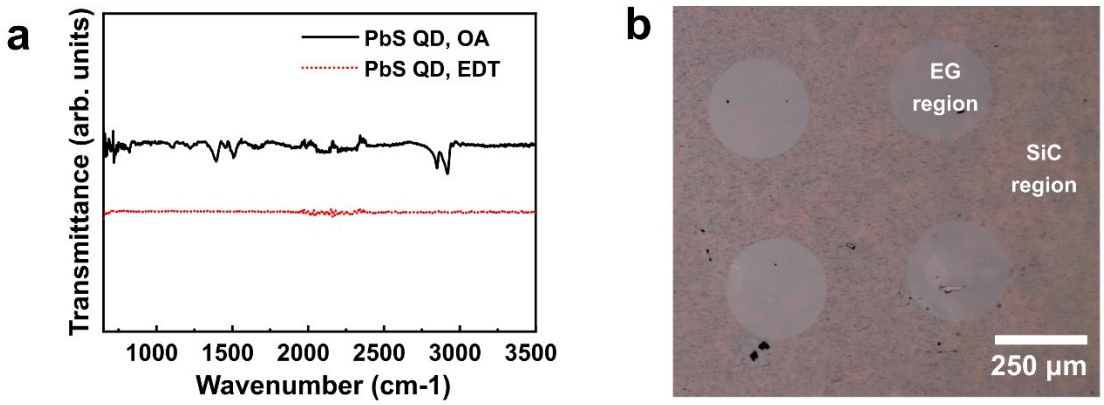

Figure 2.3: QD film FTIR spectra and QD/EG/SiC optical microscope image. (a) Fourier transform infrared spectra of oleic acid (OA) capped and EDT-exchanged PbS QD films. Carbonyl and C-H stretches associated with OA are greatly diminished following ligand exchange. (b) Optical microscope image (true color, reflected light, normal incidence) of QD/EG/SiC chip. Circular regions correspond to individual EG mesas.

below the SiC bandgap is dependent on the presence of the QD film. An optical microscope image of the hybrid device is shown in **Figure 2.3b**.

The EG/SiC Schottky diodes prior to QD deposition were evaluated by DC current–voltage ($I-V$) measurements (**Figure 2.1b**), and they displayed rectification in accordance with thermionic emission:

$$I = AA^*T^2 exp\left(-\frac{\Phi_b}{k_B T}\right)\left[exp\left(\frac{qV_a}{nk_B T}\right) - 1\right] = I_0\left[\left(\frac{qV_a}{nk_B T}\right) - 1\right] \quad (Equation\ 3)$$

giving a Schottky barrier height of $\Phi_b \sim 0.9$ eV and an ideality of $n \sim 1.1$.[43] Upon the addition of the QD film, the hybrid diodes demonstrated higher reverse leakage, ~102 more than without QDs, suggesting the presence of trap states.[44] The current under forward bias indicated the presence of a second, parallel barrier interface leading to

additional forward current at <0.2 V. We associate this with carrier transport through the QD film at the diode periphery. Upon removal of the QD layer with HF, this feature disappeared and the reverse leakage reverted to the bare state, indicating the changes were due to the QD film. We note that ultraviolet photoelectron spectroscopy measurements have revealed an electron affinity of 3.6 eV for 4H-SiC and a work function of ~4.5 eV for EDT-exchanged PbS QDs in previous reports.[21,22,45] Consistent with these findings, we propose band alignments as shown in **Figure 2.1d**.

To obtain the effective *I–V* curve of the parallel current, the bare EG/SiC current was subtracted from the total current in the hybrid case (**Figure 2.1b**), isolating the behavior of an additional QD/SiC diode at the edge of the device (**Figure 2.1c**). This parallel diode had a series resistance, $R_{s,QD}$, of 2.4 MΩ, a shunt resistance, $R_{sh,QD/SiC}$, of 200 MΩ attributed to trapping at the interface and a diode element with a reverse saturation current, $I_{0,QD/SiC}$, of 4 pA, and an ideality n = 2, obtained by subtracting the $R_{s,QD}$ voltage drop. This indicates that the QD/SiC diode exhibits Shockley–Read–Hall (SRH) trap-assisted recombination,[46] in contrast to the n ≈ 1 ideal behavior from the EG/SiC diode. At diode voltage V_a < 0.2 V, $R_{sh,QD/SiC}$ dominates the current and is likely due to a field-activated trapping mechanism at the QD/SiC interface. Trapping effects are further supported by the emergence of Lorentzian $1/f^2$ noise compared to 1/f flicker noise for the bare diode (**Figure 2.4**). The $1/f^2$ Lorentzian noise is an indicator of well-defined trap levels causing noise from variations in carrier concentration due to trapping and detrapping.[44,47,48]

The bare EG/SiC diodes displayed a photovoltaic response at photon energies above the 4H-SiC bandgap (3.2 eV) (**Figure 2.5a**), giving an open circuit voltage (V_{OC})

of ~0.25 V with 13 nW of 350 nm illumination. This agrees with the I_0 measured from the forward *I–V* curves:

$$V_{oc} = \frac{nk_bT}{q} ln\left(\frac{I_{sc}}{I_0} + 1\right) \quad (Equation\ 4)$$

With the addition of the QD film, V_{OC} and I_{SC} both decrease under the same UV illumination conditions. This is expected due to filtering of the incident light by the QD

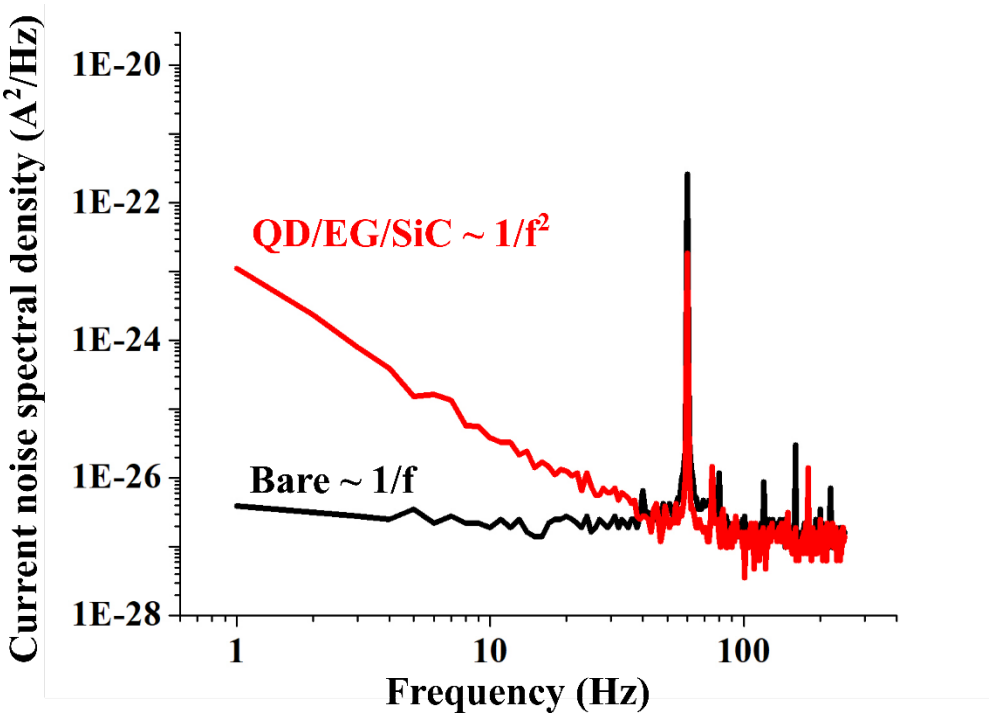

Figure 2.4: Dark current noise spectral density (A^2/Hz) for both the bare and hybrid QD-:film devices

layer. Additionally, the QD layer introduces parallel conduction via $R_{sh,QD/SiC}$, with V_{OC} approximated by $V_{OC} \approx I_{SC}R_{sh,QD/SiC}$ in the limit of low I_{SC}.

Upon illumination with visible light below the SiC bandgap, parallel conduction via $R_{sh,QD/SIC}$ similar to the UV case is seen, but a photovoltaic effect is retained, attributed to the low-barrier rectifying QD/SiC junction after QD deposition. To confirm that the photocurrent was associated with light absorption in the QD layer, three LEDs

were used with λ_{max} = 655, 843, and 1550 nm, adjusted so ~180 nW fell within the EG mesa. The measured I_{SC} (**Figure 2.5b**) were 50, 15, and <1 pA, respectively, with

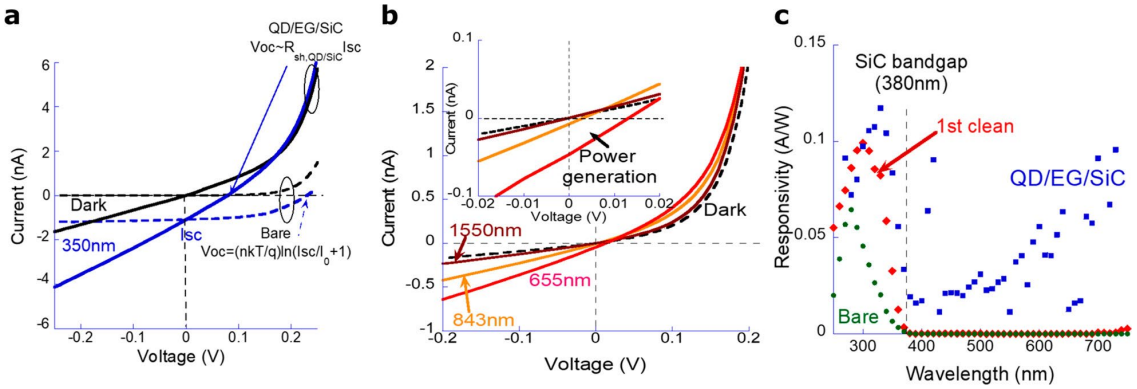

Figure 2.5: Device photovoltaic response and spectral responsivity. (a) Dark and 350 nm (UV) illuminated *I–V* curves for the bare EG/SiC and hybrid QD film devices. (b) Dark and illuminated *I–V* curves for the hybrid QD film device under 1550, 843, and 655 nm illumination at ~0.36 mW/cm2. Inset: magnified view of power-generating quadrant. (c) Responsivity vs wavelength at low frequency under wide-area illumination for EG/SiC Schottky diode before application of the QD film, after QD film deposition, and after removal of QD film via chemical etching. All data were collected at V = −1 V.

the trend in photocurrent matching the absorption spectrum of the QD film, which shows an effective bandgap of ~1350 nm corresponding to the lowest-energy electronic transition of the QDs (**Figure 2.6**).

The QD film also exhibits significant photoconductivity with reverse bias. Both the dark current (I_{dark}) and photocurrent ($I_{ph} = I(\lambda) - I_{dark}$) of the hybrid device increase monotonically with voltage, indicating the presence of carrier traps and leading to the observed photoconductive gain.[44] This increase in I_{ph} was accompanied by an increase in the lifetime measured by transient photocurrent decay under wide-area illumination at 444 nm (**Figure 2.7**). For short circuit conditions, a lifetime of ~40 ms described the

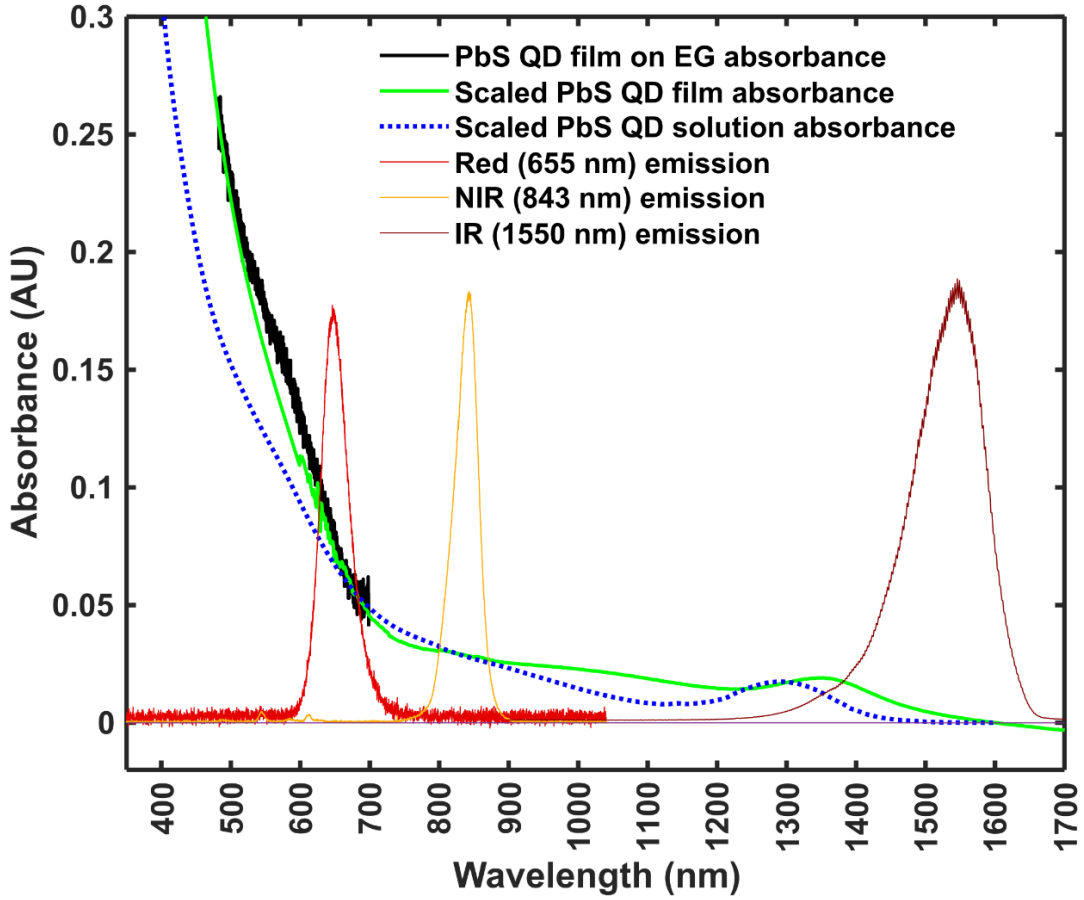

Figure 2.6: QD film absorbance and LED emission spectra. (a) Absorption spectrum of PbS QD film deposited on top of EG/SiC Schottky devices as illustrated in Fig. 1. Visible absorbance is measured directly using a micro-spectrophotometer equipped with high-NA objective lens and condenser in transmission mode. Infrared absorbance is inferred from the absorbance of a comparable film deposited on a glass substrate, shown here scaled for comparison in addition to a scaled solution phase absorption spectrum. The measured emission spectra of red and NIR LEDs used to characterize sub-bandgap PV response in **Figure 2.5b** are also overlaid for comparison.

decay well (**Figure 2.7**). As the reverse bias was increased, an additional slower lifetime emerged, increasing to 4.1 s at −1.0 V, but the faster component continued to dominate the photocurrent decay amplitude, increasing to 130 ms over the same bias range.

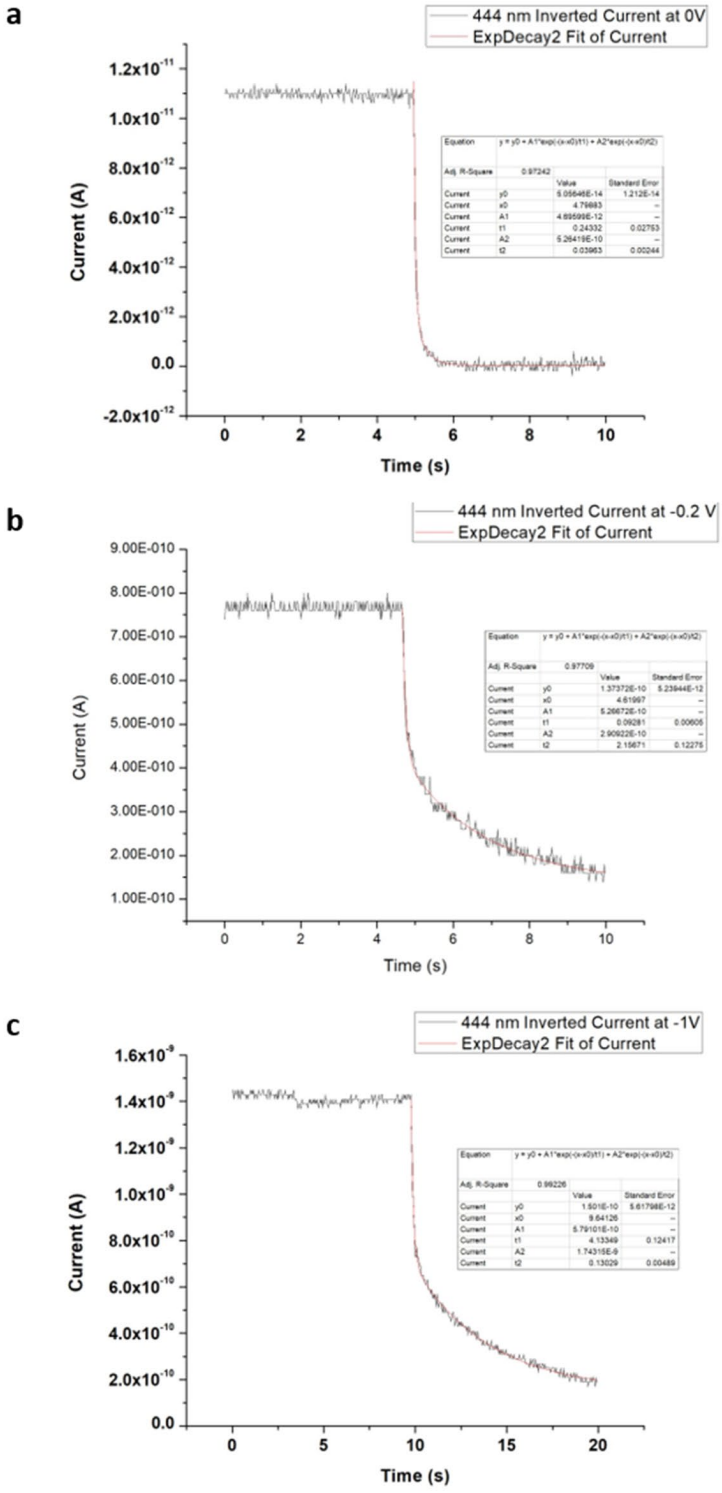

Figure 2.7: QD/EG/SiC device photocurrent transients. Illumination-to-dark transient current decays as light (444 nm) is switched off at $V_a = 0$ (a), −0.2 V (b), −1.0 V (c).

Figure 2.10 shows SPCM maps of a representative hybrid device, measured with 444 nm light chopped at 113 Hz. Without the QD layer, the SPCM signal was confined

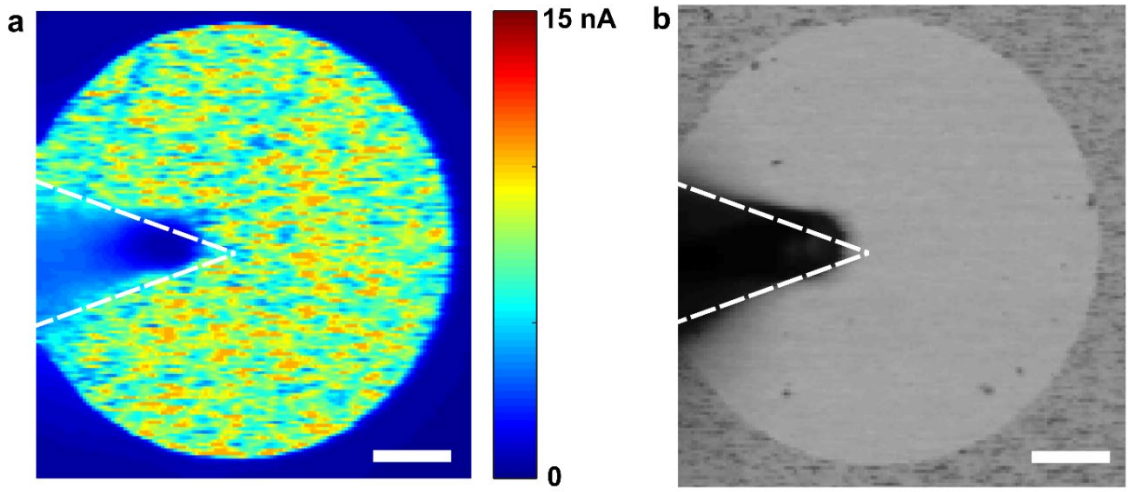

Figure 2.8: SPCM of EG/SiC Schottky diode without QD film. (a) SPCM amplitude image for a bare EG/SiC device under visible (444 nm, 616 µW) excitation and reverse bias (5 V). (b) Reflected light signal. Location of tungsten probe tip is indicated. White scalebars 50 µm.

to the EG mesa (**Figure 2.8**). After QD deposition, there was a sharp increase in I_{ph} near the periphery that was much greater than within the EG/SiC mesa. Outside the mesa, I_{ph}

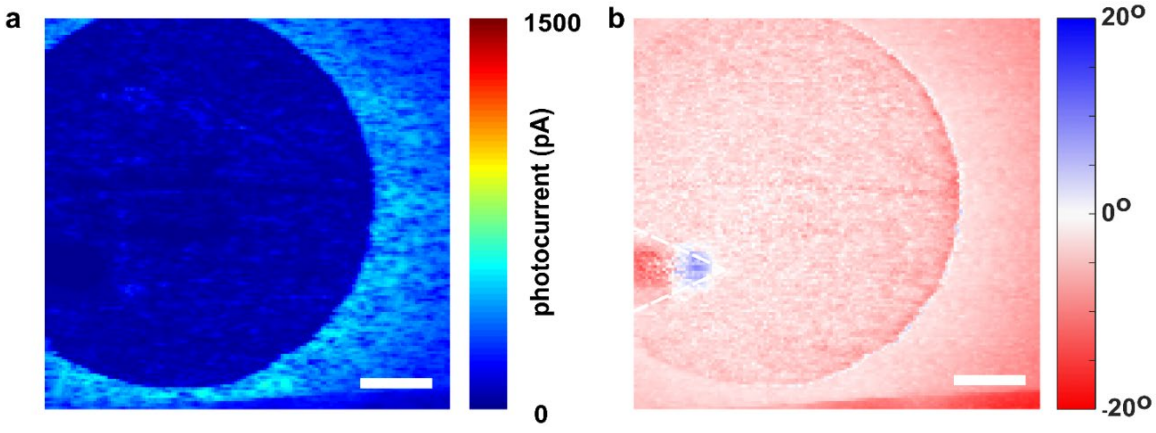

Figure 2.9: Phase map of QD/EG/SiC device. Representative SPCM (a) amplitude and (b) relative phase images for QD/EG/SiC device at short circuit (0V), scaled by the preamp and lock-in sensitivities. (a) corresponds to Fig. 3d in the main text. Phase is zeroed at the device perimeter. White scalebars 50 µm.

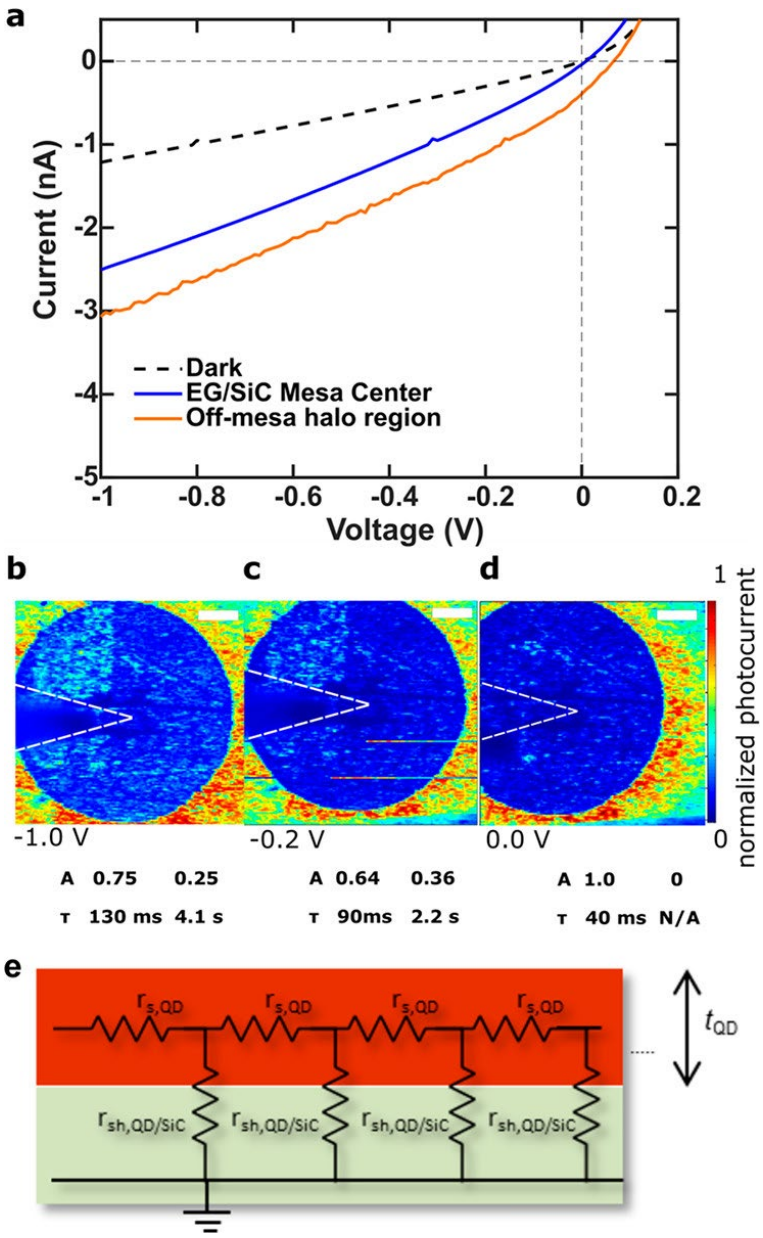

Figure 2.10: Spot *I-Vs*, bias-dependent SPCM, and TLM resistor network. (a) Current–voltage response under localized 444 nm excitation (~15 μW) for hybrid device; SPCM maps recorded at −1.0 V (b), −0.2 V (c), and 0 V for a short circuit (d) illustrating the spatial dependence of ac photocurrent from chopped light. Color scale is normalized to peak ac value at the edge of the mesa. The dashed line indicates the location of tungsten probe contact. White scale bars: 50 μm. Characteristic lifetimes and relative amplitudes for photocurrent decay accompany each image. (e) Transmission line model for series and shunt resistance contributions of the QD film.

decays slowly with distance, retaining half its value at ~80 µm at short circuit. The decay in I_{ph} with distance was accompanied by only a small change in phase (**Figure 2.9**), suggesting the decay is not of capacitive origin.

The diminished signal from on-mesa excitation indicates that the QD/EG junction is not responsible for the I_{ph} and I_{SC} under wide-area illumination: instead, the junction between the QD film and the n-type 4H-SiC epilayer is the active region. This effect is particularly notable at short circuit and under ac excitation as employed in SPCM, where photoconductive behavior is less significant. The considerable distance over which charge can be collected and the insensitivity of the decay length to applied bias (**Figure 2.10** and **Figure 2.11**) suggest that the decay is not the minority carrier diffusion length

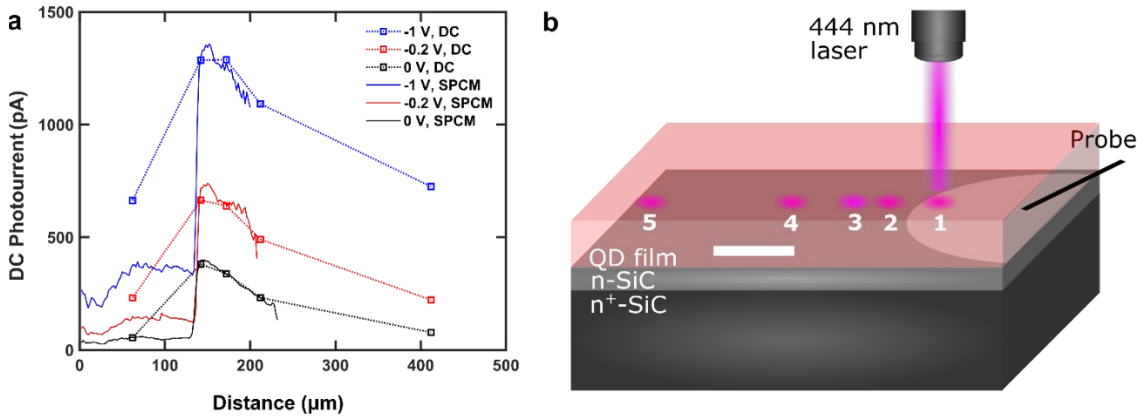

Figure 2.11. Localized excitation and AC/DC comparison. (a) Spatial dependence of DC and AC photocurrent as a function of distance from the mesa center at short circuit (V_a=0 V) and at reverse bias (V_a=−0.2V, −1.0V). DC values represent illuminated minus dark current at several locations graphically represented in (b). AC traces represent SPCM data averaged over all angles as a function of distance, and are scaled to match the peak DC photocurrent value at each voltage to facilitate comparison. Scalebar in (b) is 100 µm.

but instead reflect an increasing series resistance for excitation further away from the EG contact. In this case, a transmission line model (TLM, **Figure 2.10e**)[49] can be applied to

describe the equivalent circuit in **Figure 2.1**. Here, we assume that currents are low enough that $R_{sh,QD/SiC}$ and $R_{s,QD}$ dominate the behavior, meaning the diodes have not turned on. Under these conditions the TLM predicts an exponential decay of photocurrent with distance from the EG mesa contact, with characteristic (1/e) length L_T:[50]

$$L_T = \sqrt{\rho_{sh,QD/SiC}\left(t_{QD}/\rho_{s,QD}\right)} \quad (Equation\ 5)$$

where t_{QD} is the thickness of the QD film, $\rho_{s,QD}$ is the (3D) resistivity of the QD film, and $\rho_{sh,QD/SiC}$ is a specific interface resistance at the QD/SiC interface, defined such that $R_{sh,QD/SiC} = \rho_{sh,QD/SiC}/A_{QD/SiC}$, with $A_{QD/SiC}$ the effective interface area. The SPCM maps in **Figure 2.11** give $L_T \sim 115$ µm near $V_a = 0$ V. To approximate the effective interface area,

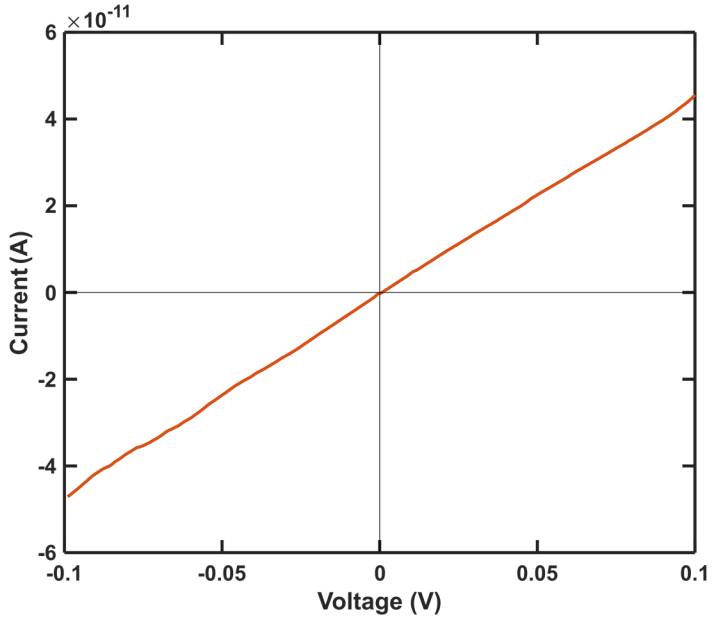

Figure 2.12: Lateral dark *I-V*s. Measurement taken between neighboring EG mesas separated by ~500 µm on a QD/EG/SiC chip.

we consider a ring of width L_T surrounding the mesa of radius r so that $A_{QD/SiC} = 2\pi r L_T + \pi L_T^2$. Using $R_{sh,QD/SiC} \sim 200$ MΩ (**Figure 2.1**), $\rho_{sh,QD/SiC} \sim 260$ kΩ·cm^2, $t_{QD} \sim 90$ nm, and solving eq 3 for $\rho_{s,QD}$ gives $\rho_{s,QD} \approx 18$ kΩ·cm, which is consistent with lateral *I–V*

measurements of the resistance between two neighboring EG mesas, conducting through the QD film (**Figure 2.12**).

In measurements of PbS QD films prepared using the same procedure on insulating substrates[51], we found ohmic contacts to evaporated top electrodes composed of high-workfunction metals, notably Au, in addition to remarkable optoelectronic responses in standalone PbS QD devices. Taken together, these observations identify the PbS QD film as a p-type semiconductor. Considering that field-effect hole mobilities $\mu \sim 10^{-3}$ cm^2/(V·s) have been reported for EDT-capped PbS QD films,[12] the bulk resistivity identified from L_T corresponds to a hole concentration $\sim 10^{17}$–10^{18} cm^{-3} in the present case.

Based on the above insights, there are design considerations that emerge for making practical solar cells and detectors from hybrid QD/EG/SiC devices: First, the highest I_{ph} comes from the QD/SiC junction, and designs should aim to maximize the incident light on this junction while maintaining charge collection via contacts. In this study, the EG forms an effective ohmic contact to EDT-terminated PbS, while forming a Schottky junction to the SiC substrate with a very high shunt resistance. The observation of minimal charge separation at the PbS QD-EG junction is consistent with some previous work on PbS QD-EG that found photoinduced charge transfer to be localized to the first few QD layers,[29] but we also observe lateral charge transport within the QD film over large distances. This indicates that EG electrodes in an interdigitated or grid structure separated by $\sim L_T$ could maximize both light absorption and charge collection. Third, the QD film thickness affects light absorption and charge transport but has not been optimized in the present devices. Films thinner than the diffusion length of carriers

will collect the majority of photogenerated carriers, but if too thin, surface recombination[52,53] effects may suppress charge collection, particularly given the observed recombination in the presence of the QD film. The measured absorbance of ~0.1 AU at λ = 655 nm for the 90 nm thick film indicates an absorption length $\alpha^{-1} \approx 390$ nm. Assuming L_T^2 scales linearly with t_{QD} as described by the TLM model in equation 3, a larger t_{QD} could enable a larger pitch between contacts. Finally, the measured lifetime ~40 ms at short circuit would yield an electron diffusion length of ~10 μm for a typical carrier mobility (μ) of ~10^{-3} $cm^2/(V \cdot s)$ in PbS-EDT. Independent measurement of carrier mobilities and diffusion lengths in QD films as a function of surface passivation and film deposition methods is an important target for future study.

2.3: CONCLUSION

We have shown that by integrating cheaply synthesized and tunable PbS QDs with a wide bandgap support, visible and IR functionality can be achieved in contexts previously not envisioned. By using QD films with EG/SiC Schottky diodes, we demonstrate photovoltaic action from IR to UV, both above and below the bandgap of SiC. The below-bandgap photovoltaic action is due to the formation of a parallel QD/SiC diode at the edge of the EG mesa, displaying above bandgap photovoltaic action. Because of the unoptimized nature of the QD/SiC interface, the specific interface resistance limits the open circuit voltage, attributed to trapping at the interface. Improvements can be made by increasing charge separation at the QD/SiC interface through optimized band alignment and surface treatment, reducing the resistivity of the QD film and increasing its thickness while maintaining a sufficiently large diffusion length. Importantly, new strategies are emerging for deposition of wide-bandgap materials of high quality

including SiC[54] as well as patterning of EG films of sufficient quality to display quantum transport behavior.[29,55] With these insights, useful photovoltaic devices and photodetectors may be realized for QD/EG/SiC hybrid architectures, particularly in the IR, where wide-bandgap materials' advantages cannot often be exploited.

2.4: EXPERIMENTAL

Materials: All reagents for synthesis were used as received. Lead (II) oxide (PbO, 99.9 %), anhydrous acetonitrile (ACN, 99.8 %), anhydrous toluene (99.8 %), and 1,2-ethanedithhiol (EDT, 98 %) were purchased from Alfa Aesar. Bis(trimethylsilyl) sulfide ($(TMS)_2S$, 95 %) and 1-octadecene (ODE, 90 %) were purchased from Acros Organics. Molecular sieves (4Å) were purchased from Mallinckrodt and activated by heating under vacuum prior to transferring into a nitrogen glovebox.

For purification, methyl acetate (MeOAc, 99 %) was purchased from Millipore Sigma and dried under activated molecular sieves in a nitrogen glovebox following degassing under partial vacuum. Polystyrene Bio Beads (S-X1, 200-400 mesh) were purchased from Biorad. Bio-Beads were used to pack a GPC column following Shen et al.1 with modifications as follows. Bio-Beads were swollen under ambient conditions with toluene. Next, toluene was evacuated from the swollen Bio-beads under partial vacuum and the medium was transferred to a nitrogen glovebox. The Bio-Beads were swollen a second time in the glovebox with anhydrous toluene and used to prepare the purification column following Shen et al.[8]

QD synthesis, purification, and analysis: Oleate-capped, colloidal PbS quantum dots (QD) were synthesized following a reported method with slight modifications, as follows[9,14]. The as-synthesized QDs were initially purified by precipitation and

redissolution (PR) using dried MeOAc and anhydrous toluene under air-free conditions. The sample was then dried under partial vacuum, transferred to a nitrogen glovebox, and re-dispersed in anhydrous toluene. QDs were then purified by gel-permeation chromatography (GPC) in the glovebox using reported methods1. An estimated concentration of 20-30 mg/mL for the GPC-purified QDs in anhydrous toluene was achieved by volume reduction under partial vacuum. The sample was filtered through a syringe filter (0.1 μm PTFE membrane) prior to the deposition of thin films.

Routine absorbance spectra were obtained on a Cary 5000 UV-vis-NIR spectrometer in dual beam mode. For samples in solution, a quartz cuvette with a path length of 1 cm was used. For thin films, glass slides were used as substrates on a solid sample holder.

Epitaxial substrates: All SiC substrates used for epitaxial growth were highly doped (~10^{19}) n^+ 4H-SiC 8°offcut, diced into 1 x 1 cm^2 samples from a 3-inch wafer purchased from Cree (www.cree.com). The substrates were degreased with organic solvents, deoxidized with hydrofluoric acid and rinsed with de-ionized water before being blown dry with Argon for growth.

Formation of QD films by spin coating: QD thin films were deposited following a layer-by-layer (LBL) spin coating and ligand exchange procedure using EDT as the exchange ligand. In a typical thin film, formation of a layer of the LBL ligand-exchanged film was conducted as follows. First, ~15-25 μL of GPC-purified PbS QDs in anhydrous toluene (20-30 mg/mL) were deposited on a rotating substrate at 3000 rpm in a nitrogen glovebox. Next, 3 drops of an EDT/anhydrous ACN solution (1 % *v/v*) were administered to the rotating substrate followed by 2 drops of anhydrous ACN and anhydrous toluene.

Solvent was allowed to dry on the rotating substrate between each step for approximately 30 seconds. For films deposited on glass or SiO2/Si substrates, the substrates were cleaned by successive sonication in detergent/deionized water, acetone, isopropyl alcohol, ethanol, and deionized water prior to film deposition.

Light Dependent Measurements: Photocurrent measurements under wide area and localized illumination were performed to evaluate infrared sensitivity and confirm the mode of operation of the devices. To evaluate the spectral response from UV and visible, light from a xenon source was passed through a monochromator to select wavelengths 250-700 nm, with a bandwidth of 5 nm. The optical power at each wavelength was measured with a commercial Si photodiode. Transient and noise measurements were conducted with the ground current routed through a trans-impedance preamplifier to convert the current to a voltage displayed on an oscilloscope. Noise spectra were obtained by taking the Fourier transform of the dark current signal. The NIR response was probed using a series of red and NIR LEDs at calibrated optical power densities.

Conductivity Measurements on Insulating Substrates: PbS-EDT films were deposited on Si/SiO_2 substrates as described above. Au metal contacts were evaporated on top of the film through a shadow mask, forming devices 50 nm thick and 4 cm wide at various spacings of 200-400 μm. Contact pads were gently probed with flexible tungsten microprobes to avoid damage to films. Measurements at low bias (< 1 V) displayed linear *I-V* relationships with resistance proportional to contact separation, characteristic of ohmic contacts.

Kelley, M. L.; Letton, J.; Simin, G.; Ahmed, F.; Love-Baker, C. A.; Greytak, A. B.; Chandrashekhar, M. V. S. Photovoltaic and Photoconductive Action Due to PbS Quantum Dots on Graphene/SiC Schottky Diodes from NIR to UV. ACS Appl. Electron. Mater. 2020, 2 (1), 134–139. https://doi.org/10.1021/acsaelm.9b00651.). Copyright 2020 American Chemical Society.

CHAPTER 3: SPATIALLY RESOLVED FOURIER TRANSFORM IMPEDANCE SPECTROSCOPY: A TECHNIQUE TO RAPIDLY CHARACTERIZE INTERFACES, APPLIED TO A QD/SIC HETEROJUNCTION[2]

3.1: INTRODUCTION

This work describes the results of our ongoing collaborative efforts with the M. V. S. Chandrashekhar laboratory at the University of South Carolina. We demonstrate a technique to quickly build and spatially map the frequency response of optoelectronic devices. The transfer function of a linear system is the Fourier transform of its impulse response. Such an impulse response is obtained from transient photocurrent measurements of devices such as photodetectors and solar cells. We introduce and apply Fourier Transform Impedance Spectroscopy (FTIS) to a PbS colloidal quantum dot (QD)/SiC heterojunction photodiode and validate the results using intensity-modulated photocurrent spectroscopy. Cutoff frequencies in the devices were as high as ~10kHz, showing their utility in advanced thin film and flexible electronics. The practical frequencies for FTIS lie in the mHz-kHz range, ideal for composite materials such as QD films that are dominated by interfacial trap states. These can lead to characteristic lengths for charge collection ~20-500 μm dominated by transmission line effects, rather than

[2] Reprinted from Kelley, M. L.; Simin, G.; Hussain, K.; Khan, A.; Greytak, A. B.; Chandrashekhar, M. V. S. Spatially Resolved Fourier Transform Impedance Spectroscopy: A Technique to Rapidly Characterize Interfaces, Applied to a QD/SiC Heterojunction. Appl. Phys. Lett. 2021, 118 (22), 223102. https://doi.org/10.1063/5.0046439 with the permission of AIP Publishing.

intrinsic diffusion and drift length scales, enabling extraction of interfacial capacitances and series/parallel resistances.

Rapid characterization of junction parameters and film properties is crucial for optimizing optoelectronic devices. This is particularly relevant for novel materials and thin film devices such as colloidal quantum dot (QD) photovoltaics and mixed-dimensional heterostructures, where interfaces and structural imperfections can dominate.[26,57,58] In this regard, frequency domain and time domain characterization methods are commonly employed to obtain information on defects[59], trapping[60], and recombination[61], making them valuable tools for such purposes. Most commonly, impedance spectroscopy (IS) is an appealing nondestructive ensemble technique performed in the frequency domain. An IS experiment is undertaken by applying a sinusoidal input voltage to the sample and measuring the output sinusoidal current response as a function of frequency. By modeling the device with equivalent circuit elements, details on resistive and capacitive quantities, such as the series resistance or charge transfer resistances of solar photovoltaics[62–64] can be obtained. From quantities such as these, IS is used to optimize devices by studying these characteristics sensitivity to device parameters, such as contact metals or chemical modifications to active layers. Intensity modulated photocurrent spectroscopy (IMPS) is a closely related technique to IS that employs light-induced perturbations at varying frequency to extract information on resistive and capacitive elements and charge transport processes within an optoelectronic device.

Despite the merits of these frequency domain methods, characterizing composite materials holds challenges. For example, IS and IMPS require small signals to be

linearized with circuit elements, presenting a tradeoff in terms of signal level with accuracy. In addition, for low dimensional materials such as QDs, capacitive elements manifesting from trap states[65] and interfaces impart slow device bandwidths[66] and necessitate low frequency perturbations, compounding the experimental run time. These challenges are also encountered in scanning measurement techniques such as scanning photoinduced impedance spectroscopy[67] and scanning IMPS[68] methods, where the appeal of establishing spatial correlation with localized impedances are hindered by the time investment of multiple scans in the low frequency regime.

Beyond the frequency domain methods of IS and IMPS, pure time domain techniques such as deep level transient spectroscopy (DLTS)[69,70] or current-deep level transient spectroscopy (i-DLTS) provide information on trap states, but they require temperature dependent measurements, which are time-consuming and challenging. Due to the tradeoffs and time required for these techniques, exploring alternative methods to characterize interfaces in a rapid manner are useful.

Here, we introduce a method in the time domain to quickly build the frequency response of a device by computing the Fourier transform of a transient photocurrent. In any linear, time invariant system[71] (or any system that can be linearized by operating at small signals[71,72]), the output response, $x_{out}(t)$ to an input signal, $x_{in}(t)$ is characterized in the time domain by the impulse response $h(t)$, which is the output when the input is a Dirac delta function, $\delta(t)$. The output $x_{out}(t)$ is given by the convolution of $x_{in}(t)$ with $h(t)$,[71]

$$x_{out}(t) = \int_{-\infty}^{+\infty} x_{in}(t-\tau)h(\tau)d\tau \quad (Equation\ 6)$$

For a sinusoidal input, $x_{in}(t) = exp(j\omega t)$, the output can be written as:

$$x_{out}(\mathrm{t}) = \exp(j\omega t)\int_{-\infty}^{+\infty}\exp\left(-j\omega\tau\right)h(\tau)d\tau \quad (Equation\ 7a)$$

$$x_{out}(\mathrm{t}) = H(\omega)x_{in}(t) \quad (Equation\ 7b)$$

so that the system is represented in the frequency domain by the transfer function *H(ω)*, which is shown to be the Fourier transform of the broadband impulse response *h(t)*, i.e.

$$H(\omega) = \mathcal{F}\big(h(t)\big) = \int_{-\infty}^{+\infty}\exp(-j\omega\tau)\,h(\tau)d\tau \quad (Equation\ 8)$$

In practice, it is difficult to generate an impulse input. Using the linearity of the devices under study, we instead use the step response*, s(t)*, which is the output for a unit step input, *u(t)*, provided by turning an electrical or an optical source on (or off). Just as *δ(t)* is the derivative of *u(t)*, the impulse response, *h(t)* is computed by:

$$h(t) = \frac{ds(t)}{dt} \quad (Equation\ 9)$$

Once *h(t)* is obtained, the frequency response *H(ω)* is directly known via a numerical Fourier transform (**Figure 3.1**). The frequency limits of this measurement are determined by how quickly x_{out} can be measured. If the transient is sampled every T_s~1 ms (i.e. sampling frequency of 1 kHz) a high frequency Nyquist[71] limit $f_{max}=1/2T_s$ ~500 Hz is obtained. The lower frequency limit, f_{min} is determined by the overall transient acquisition time. For an acquisition time T_a of 10 s at T_s= 1 ms, the total number of samples is T_a/T_s=104, giving $f_{min}=f_{max}/(T_a/2T_s)$=0.1 Hz, where the extra factor of 2 arises from negative frequencies for real signals[71]. A comparable measurement in the frequency domain would require at least 10 cycles for each frequency point, leading to >100s for just the 0.1 Hz point alone, underscoring the greater speed of FTIS. This is because the pulse that generates *s(t)* is broadband i.e. contains a large range of frequencies by Fourier's theorem.[71]

These ranges are ideal for characterizing polymer and composite materials with typical response times in the ms-mins range[11,57,73]. The low frequency range is particularly tantalizing given the challenges in generating stable waveform inputs at low frequencies and small amplitudes[71] using mechanical chopping, or digital modulation for photoexcitation. In our measurements, typical photocurrent signal levels for transient measurements lie in the nA-μA range, whereas higher frequency measurements provide pA level currents[26], requiring sensitive lock-in techniques.

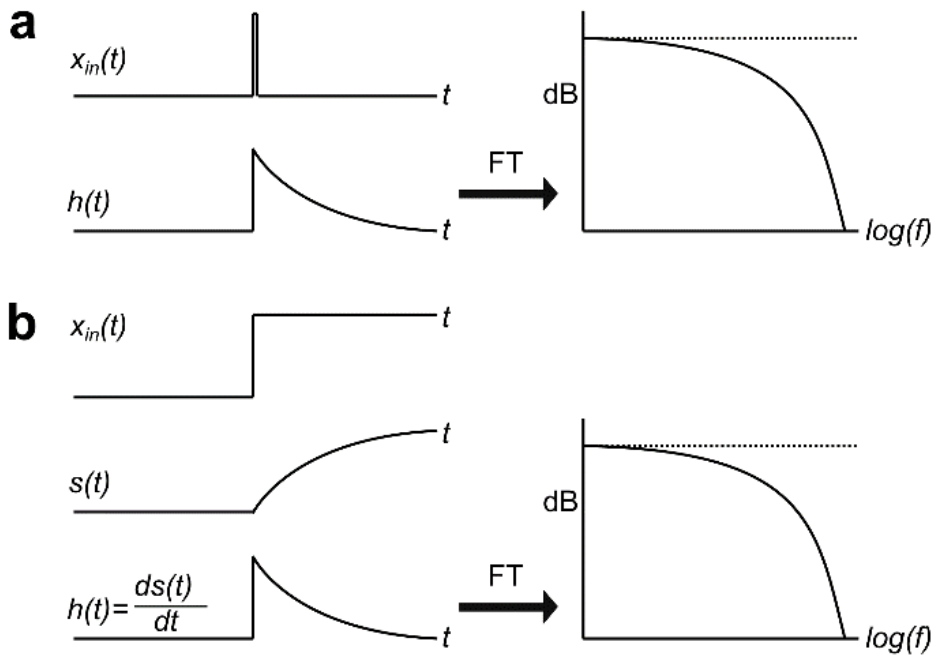

Figure 3.1: Fourier Transform Impedance Spectroscopy concept graphic. Graphic illustrating the application of Fourier theorem and the transformation to achieve the frequency response from (a) an impulse response and (b) a step-up response.

The higher overall signal levels in the FTIS technique presents another advantage. Fourier transforms have been used in infrared[74], Raman[75], and electrochemical impedance[76] spectroscopies owing to the same data acquisition speed and other advantages outlined here. Fourier transform methods have also been applied to voltage

and optical step function excitation of polymer solar cells,[64] but is here combined with localized excitation to isolate a single planar interface by probing lateral signal propagation.

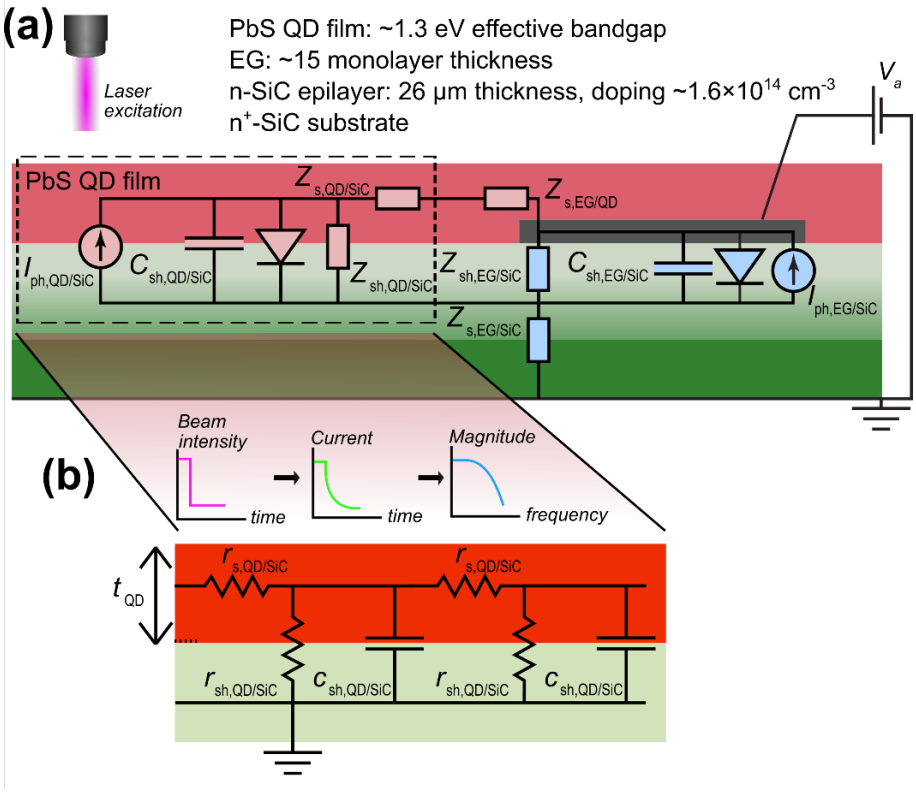

Figure. 3.2: QD/EG/SiC device schematic for FTIS studies. (a) Equivalent circuit diagram of the QD/EG/SiC hybrid device with the QD/SiC interface outlined by the dashed box. Diode elements and associated photocurrents are also indicated. (b) Transmission line model showing series impedances of the QD film and shunt impedances and shunt capacitances for the QD/SiC interface, per unit width.

3.2: RESULTS AND DISCUSSION

We targeted QD/SiC photodiodes as a representative test platform to apply this transient Fourier technique. We have recently demonstrated that p-type PbS QDs can form an IR-sensitive photodiode junction with an n-type single crystal SiC substrate. As shown in **Figure 3.2a**, our device includes epitaxial graphene (EG) electrodes, grown on the substrate prior to QD deposition as an effective ohmic contact to the QD film. The

EG forms a Schottky contact to the SiC, such that current at reverse bias (and small forward bias) is dominated by the QD/SiC junction. PbS QD/SiC junctions with epitaxial graphene (EG) electrodes are formed upon deposition of the QD layer. Previously, we showed that these devices exhibit photoresponses determined by the PbS QD's effective bandgap, while the effective transport length is the transfer length (L_T) of the QD/SiC heterojunction, determined by transmission line effects rather than diffusion/drift, from which we determined the shunt and sheet resistances[7]. Because L_T extends to many microns at low frequency, we are able to selectively excite the QD/SiC interface in spatially resolved FTIS measurements. We demonstrate that, in this manner, FTIS can be used to additionally obtain the junction capacitance. We validate FTIS independently with IMPS, yielding cutoff frequencies in the ~10 kHz regime. The bandwidth of EG/SiC heterostructures[25,77] and QD detectors[78] is such that scanning FTIS offers a substantial speed advantage in accomplishing the measurement.

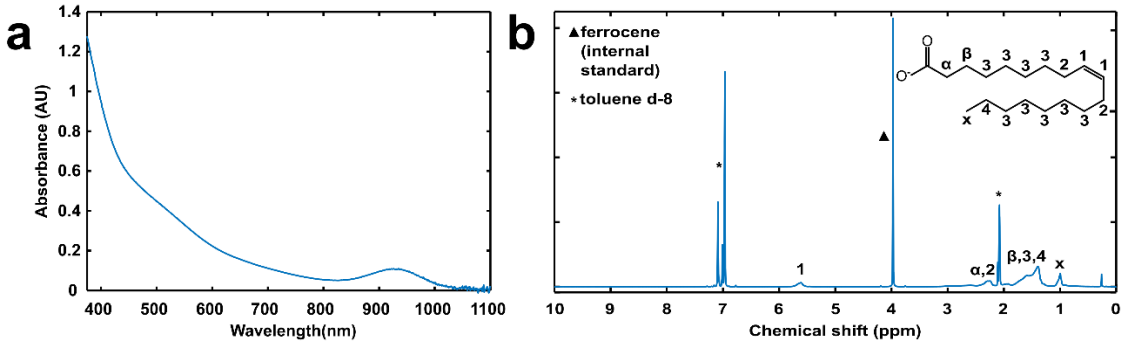

Figure 3.3: PbS QD characterization. (a) absorbance spectrum of GPC-purified, colloidal PbS QDs in octane. (b) 1H NMR spectrum of the QDs in d-8 toluene with ferrocene internal standard.

PbS QDs with an effective bandgap of ~927 nm (~1.3 eV, diameter ~3 nm) were synthesized as reported in[14] The QDs were then purified using gel permeation chromatography,[7–9,35] arriving at an oleate surface ligand population of ~110/QD as

determined by NMR (**Figure 3.3**), consistent with PbS QDs prepared from colloidal PbO precursor methods.[9] The diameter was estimated from a sizing curve based on the lowest-energy excitonic absorption peak.[14] Using a n^+ 4HSiC substrate with an n-type epilayer, EG/n-SiC Schottky diodes were grown and then patterned by photolithography. The state of the devices was characterized prior to QD deposition (**Figure 3.4**) by spot *I-V* measurements and scanning photocurrent microscopy (SPCM) at

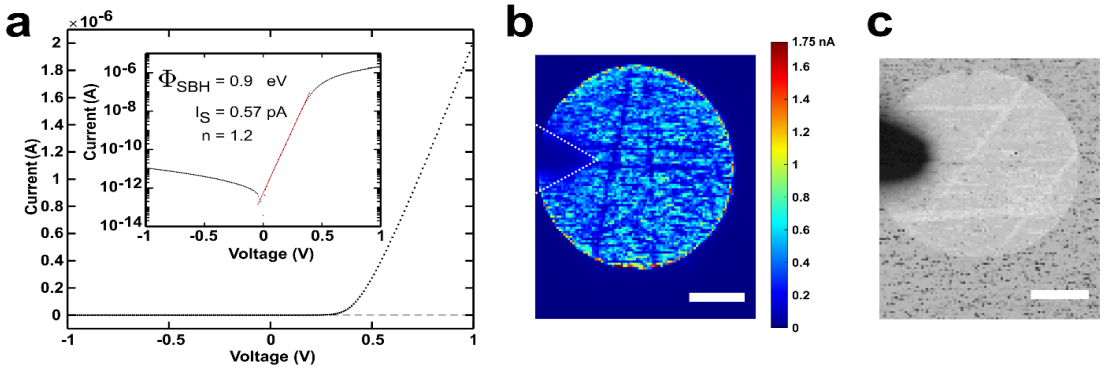

Figure 3.4: Bare EG/SiC Schottky diode characterization. (a) shows the dark *I-V* characteristic of a ~175 µm diameter EG mesa device. Inset in (a) shows the *I-V* sweep on a semilogarithmic scale with annotated diode parameters, where Φ_{SBH}, I_S, and n indicate the Schottky barrier height, reverse saturation current, and diode ideality, respectively. Scanning photocurrent microscopy (SPCM) photocurrent and reflected signal images are displayed in (b) and (c), respectively, for the same device at 20 V reverse bias under 444 nm excitation (90 µW) modulated at 137 Hz. White scalebars are 50 µm, and dotted white lines in (b) indicate the location of the tungsten probe contact.

444 nm, with results consistent with our previous report.[7] A layer-by-layer spin coating process (3 cycles total, in a nitrogen filled glovebox) was used to deposit a QD film and accomplish ligand exchange with 1,2-ethanedithiol (EDT) to form the QD/EG/SiC hybrid device structure. Atomic force microscopy was taken in the same manner as before. Spot *I-V*s, FTIS, and IMPS were acquired in the same manner as for the bare EG/SiC control.[7] FTIS with spot illumination was undertaken as follows. Devices were held under a

constant bias with the digitally modulated 444 nm diode laser defocused to form a ~25 μm spot size through an objective lens (20x, 0.42 NA). Photocurrent was routed through a current preamplifier to a digital oscilloscope to record transients. For comparison, IMPS spectra with spot illumination were obtained by routing photocurrent through a current preamplifier to a network analyzer. FTIS, IMPS, and spot *I-Vs* were conducted under the same illumination conditions and locations under ambient conditions.

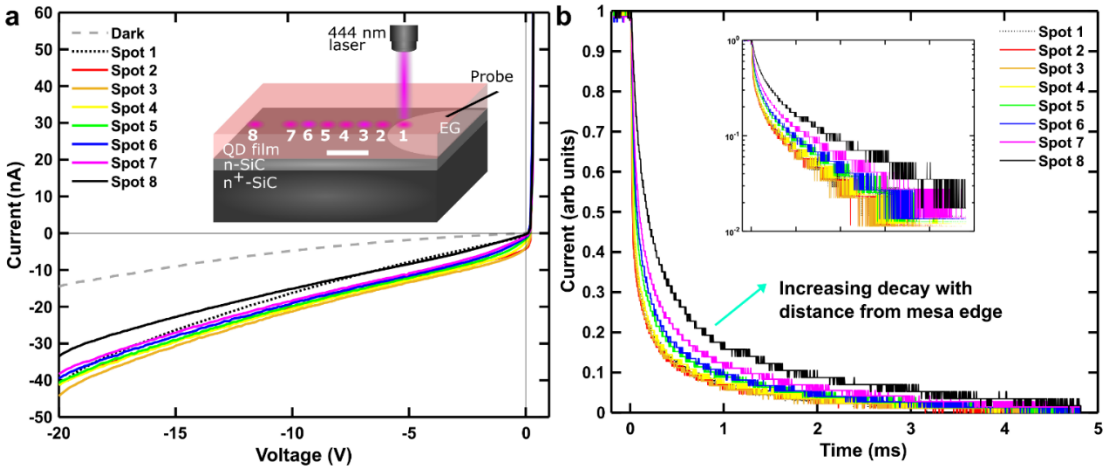

Figure 3.5: Spot *I-Vs* and photocurrent transients. (a) Static *I-V* curves with spot illumination at 444 nm (~186 μW). Inset shows the device schematic and general spot illumination regions for *I-Vs*, FTIS, and IMPS measurements. (b) Normalized 20 V reverse bias photocurrent transients under the same spot illumination intensity and locations. Inset shows transients on a semilogarithmic scale.

Figure 3.5 shows static *I-V* curves of the QD/EG/SiC photodiodes in the dark, and under illumination at various distances from the edge of the ~250 μm diameter EG electrode. The DC photocurrent decreases away from the EG electrode edge. A traditional explanation would attribute this decay to charge collection near the electrode.[79] However, in our previous paper, we demonstrated that this was due to transmission line effects instead.[7] The characteristic length scale for a transmission line is L_T which describes the transfer of electrical current across an electrical interface. For a

lumped element resistance-conductance-capacitance (*RGC*) transmission line model (**Figure 3.2b**):[50,80]

$$\frac{1}{L_T} = \sqrt{r_s\left(\frac{1}{r_{sh}} + j\omega c_{sh}\right)} = \sqrt{\frac{\rho_{QD}}{t_{QD}}\left(\frac{1}{R_{sh,QD/SiC}} + j\omega C_{sh,QD/SiC}\right)} \quad (Equation\ 10)$$

where ρ_{QD} is the 3D resistivity of the QD film, and t_{QD} is the thickness of the QD film. Shunting conductances denoted by G in the RGC model are represented here by resistive elements per $G=1/R$, with $R_{sh,QD/SiC}$ specifying the specific shunt resistance at the QD/SiC interface (in Ω-cm^2), and $C_{sh,QD/SiC}$ as the specific areal shunting capacitance (in F·cm^{-2}). At low frequencies, shunting capacitances are open circuits, and only the resistances are needed to quantify L_T as in our prior work.[7] At high frequencies, the capacitances short out and dominate current flow through the QD/SiC junction, leading to shorter L_T. The cutoff angular frequency $\omega_c = (R_{sh,QD/SiC}C_{sh,QD/SiC})^{-1}$, at which the phase change is 22.5 degrees for transmission lines, rather than the 45 degrees for a proper single pole response.[71]

In the low frequency regime, using t_{QD}~140 nm (**Figure 3.6**), L_T ~270 μm from SPCM (**Figure 3.7**) as defining the active device area, and the total shunt resistance R_{sh} ~270 MΩ from *I-V* measurements (**Figure 3.5a**) of the QD/EG/SiC device, we obtain a $R_{sh,QD/SiC}$ ~1.2 MΩ-cm^2, larger than the 260 kΩ-cm^2 obtained in our previous work. The extracted ρ_{QD} of ~22 kΩ-cm was comparable to our previous report with larger PbS QDs (4.5nm diameter).[7]

The comparable ρ_{QD}, but ~5x larger $R_{sh,QD/SiC}$. suggests the formation of a cleaner QD/SiC interface. The ligand exchange conditions could have facilitated this. A systematic study by Kirmani[81] indicated optimal conditions for solid-state exchanged PbS

QD (3.2 nm size) films with EDT included ligand solution concentrations ~0.01 % *v/v*. The ligand concentration here was lower (~0.4 % *v/v*) than our previous work (1 % *v/v*) with larger QDs.[7] We speculate that implementing a more optimal ligand exchange process and better infilling[81,82] by smaller QDs on the rough (~10 nm rms) SiC[36] surface facilitated the formation of a superior QD/SiC junction.

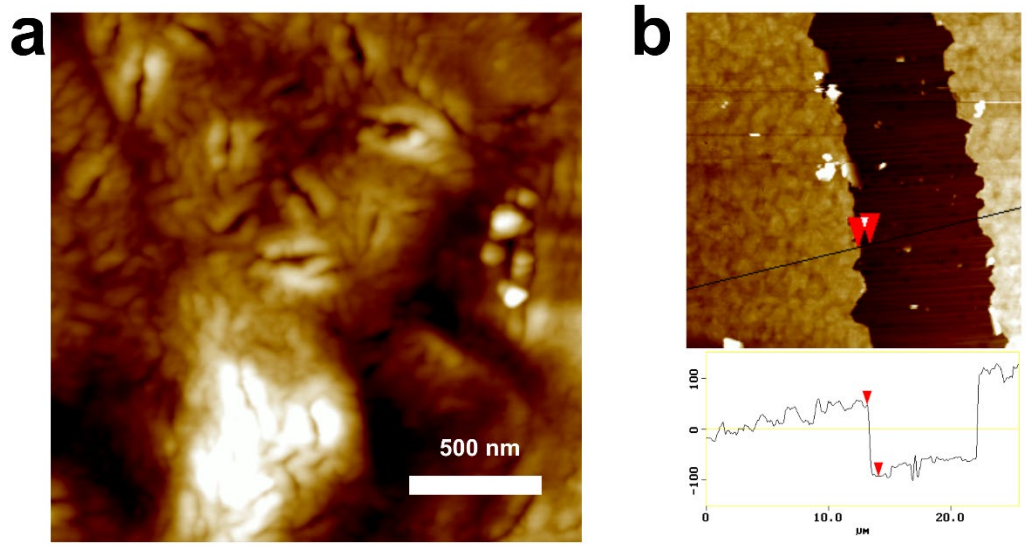

Figure 3.6: QD film structural data. (a) Atomic force microscopy (AFM) image of the PbS QD film deposited on the EG/SiC substrate. (b) AFM image and line profile used to extract the QD film thickness.

Photocurrent transients at 20 V reverse bias for each location displayed in **Figure 3.5** show multi-exponential decays, as observed previously.[7] These decays increased distinctly in lifetime with distance from the EG edge. Although variations in photocurrent decays have been affiliated with localized defects in transient photocurrent mapping reports on organic photovoltaics[83], we do not attribute the increase in decay times to such imperfections given the broadly homogeneous decay of the SPCM signal (**Figure 3.7**) from the EG edge. We reason that the increase in photocurrent decay times with distance indicated an increasing series resistance in the QD film (**Figure 2**), consistent with our

past report. Contributions to the photoresponse from absorption in the underlying SiC substrate were negligible: in bare EG/SiC devices (**Figure 3.8**), a low but nonzero

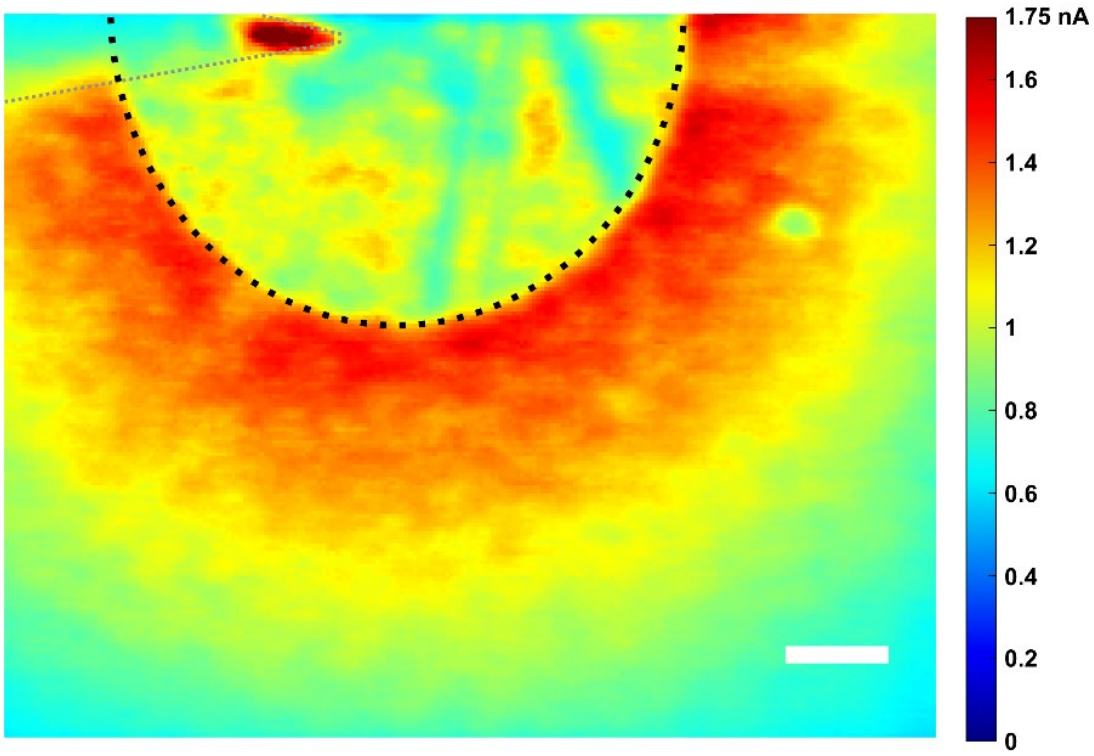

Figure 3.7: QD/EG/SiC SPCM image. The QD/EG/SiC device was held under 20 V reverse bias with 444 nm excitation (~186 µW) modulated at 77 Hz. The white scalebar is 50 µm. The black dotted hemispherical outline indicates the edge of the ~250 µm diameter EG mesa probed for contact, and grey dotted lines indicate the location of the tungsten probe.

photocurrent transient with lifetime <0.1 ms off the edge of the EG mesa region was observed, contrasting with larger photocurrent and relatively longer lifetimes (~2 ms) observed in QD/EG/SiC hybrids.

The Fourier transform of photocurrent transients was used to obtain corresponding frequency responses of the QD/SiC devices. **Figure 3.9** and **Figure 3.11** show the frequency dependence measured explicitly by IMPS (~90 s for each measurement), and that extracted from FTIS (< 3.5 s for each measurement) overlaid.

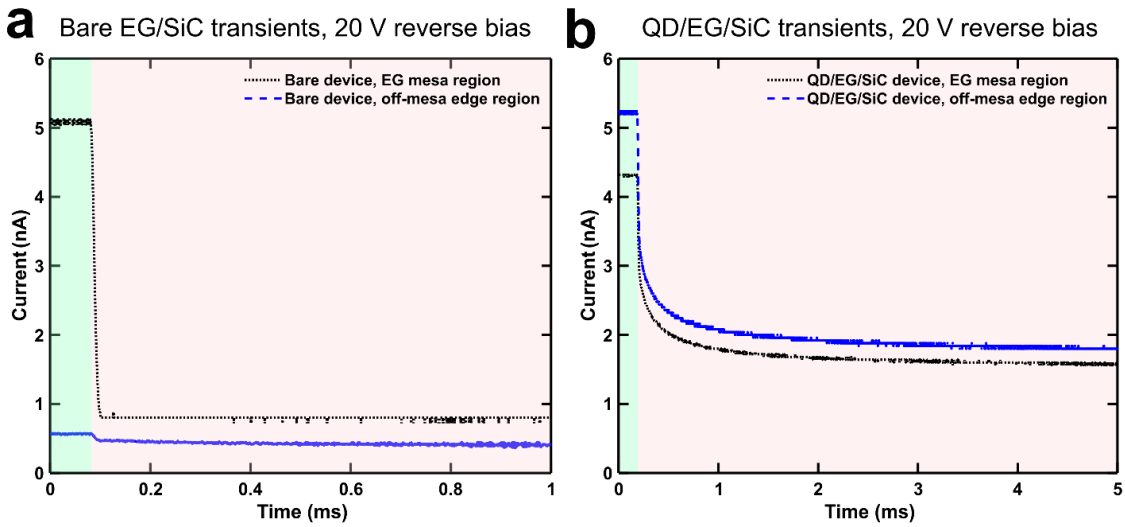

Figure 3.8: Raw transients of bare EG/SiC and QD/EG/SiC devices. (a) bare EG/SiC device transients with 444 nm excitation (~460 µW). (b) QD/EG/SiC device transients with 444 nm excitation (~186 µW). Both devices were held at 20 V reverse bias with localized photoexcitation as indicated in the legend. Green and red shading indicate illuminated and non-illuminated states, respectively.

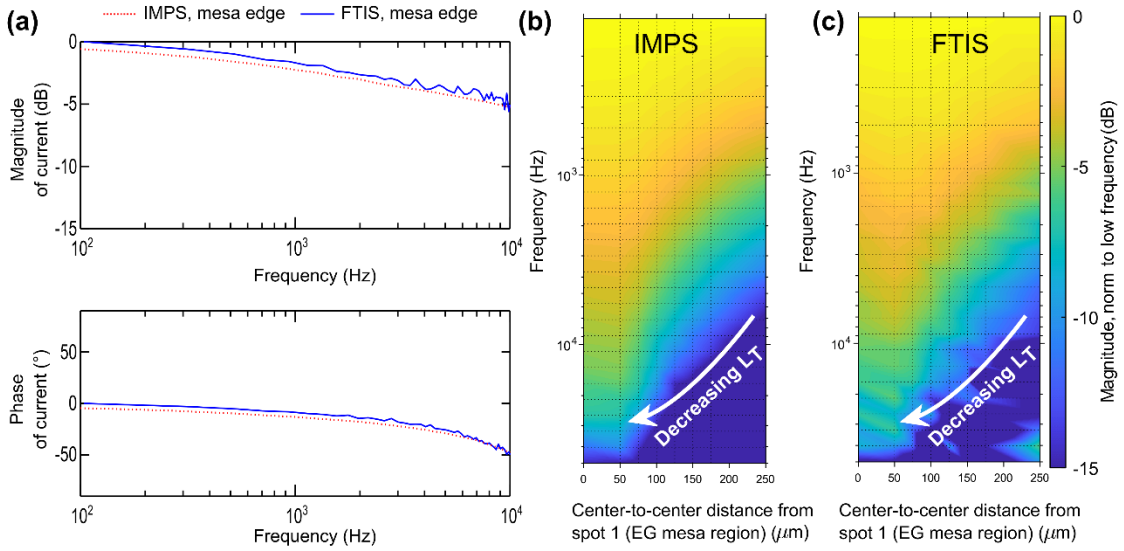

Figure 3.9: IMPS and FTIS comparison. Spatially resolved photocurrent by IMPS and FTIS at 20 V reverse bias with 444 nm excitation (~186 µW). (a, top) shows the IMPS spot 2 spectra overlaid with the FTIS spectrum, with (a, bottom) displaying the corresponding phase spectra. (b) IMPS heat map showing position dependent photocurrent magnitude. (c) FTIS heat map. Magnitude spectra in (a-c) are normalized at low frequency for clarity.

The two methods have excellent agreement both in magnitude and phase, showing the simplicity, accuracy, and speed of FTIS over more complex traditional frequency domain techniques. The frequency response of the bare EG/SiC photodiode was consistent for both FTIS and IMPS (**Figure 3.10**). Notably, the f_{3dB} bandwidth of both bare and QD/SiC photodiodes was ~10 kHz, comparable to other heterostructure optoelectronics employing low dimensional materials.[73,78]

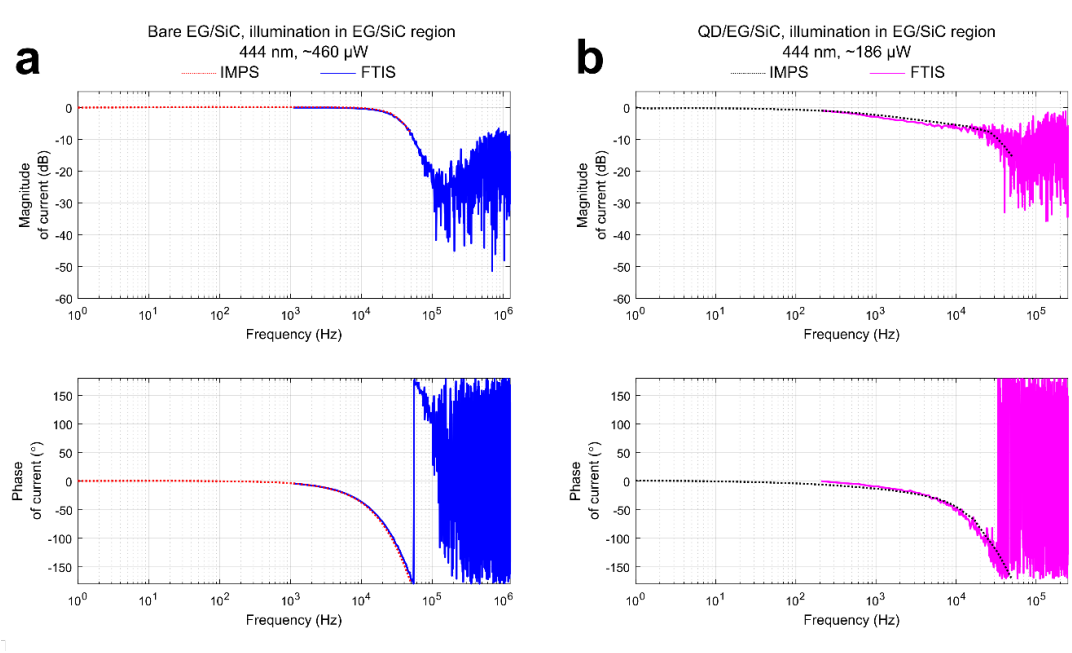

Figure 3.10: Frequency response of a bare EG/SiC and a QD/EG/SiC device. (a) shows FTIS and IMPS magnitude (top) and phase (bottom) spectra for a bare ~175 μm diameter EG/SiC device at 20 V reverse bias. (b) shows FTIS and IMPS magnitude (top) and phase (bottom) spectra for a QD/EG/SiC device (~250 μm diameter EG mesa) at 20 V reverse bias. Both devices were illuminated in the EG mesa region with a 444 nm diode laser. Magnitude spectra are normalized at low frequency.

Spatial and frequency dependencies obtained by the two methods are combined in **Figure 3.9b-c**. The L_T for each frequency is the distance that the signal decreases to $1/e$, or a power loss of $1/e^2$ (i.e. $20 \cdot log_{10}(e)$=~8.7 dB) from the EG mesa edge.[50,80] The trend is shown in both IMPS and FTIS where low and high frequencies correspond to resistive

and capacitive dominated regimes, respectively. Bias-dependent mapping of the QD/EG/SiC photodiode frequency response was employed to characterize capacitive elements. **Figure 3.14** shows L_T extracted from **Figure 3.9** and **Figure 3.12** plotted as a function of frequency for 3 different QD/SiC photodiode biases, with overlaid lines indicating fits

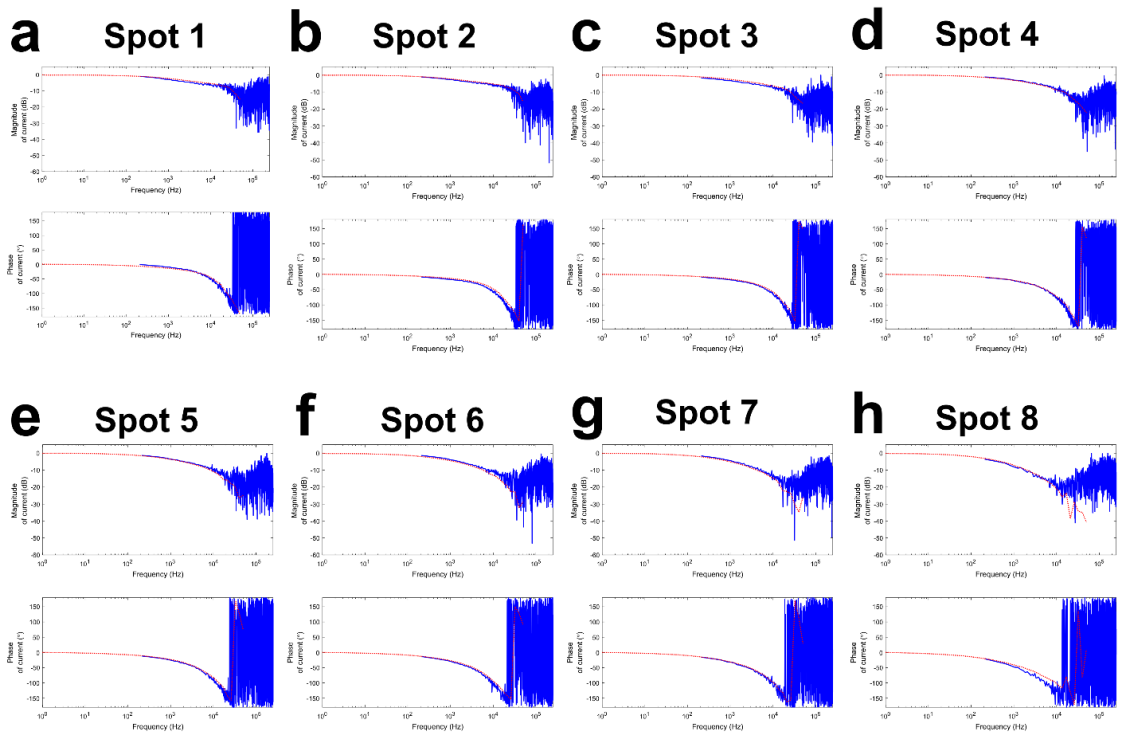

Figure 3.11: FTIS and IMPS spectra for 20 V reverse bias. Panels (a)-(h) display magnitude and phase spectra for spots 1-8. Solid blue lines and dotted red lines correspond to FTIS and IMPS spectra, respectively. Spectra are normalized at low frequency. Spot locations and measurement conditions correspond to data illustrated in **Figure 3.5**.

from Equation 5 to obtain the QD/SiC specific junction capacitances. We infer a decrease in $C_{sh,QD/SiC}$ with increasing reverse bias. We note that slower device transients with increasing reverse bias (**Figure 3.13**) were observed. Although such behavior is atypical of photodiodes, we attribute the observation to an increase in the device area and via L_T

(**Figure 3.13, Figure 3.12**). Given that $C_{sh,QD/SiC}$ decreases with increased reverse bias, it suggests that the key capacitance is the geometric depletion capacitance arising primarily from depletion in the n-SiC epitaxial layer. We do not see excess

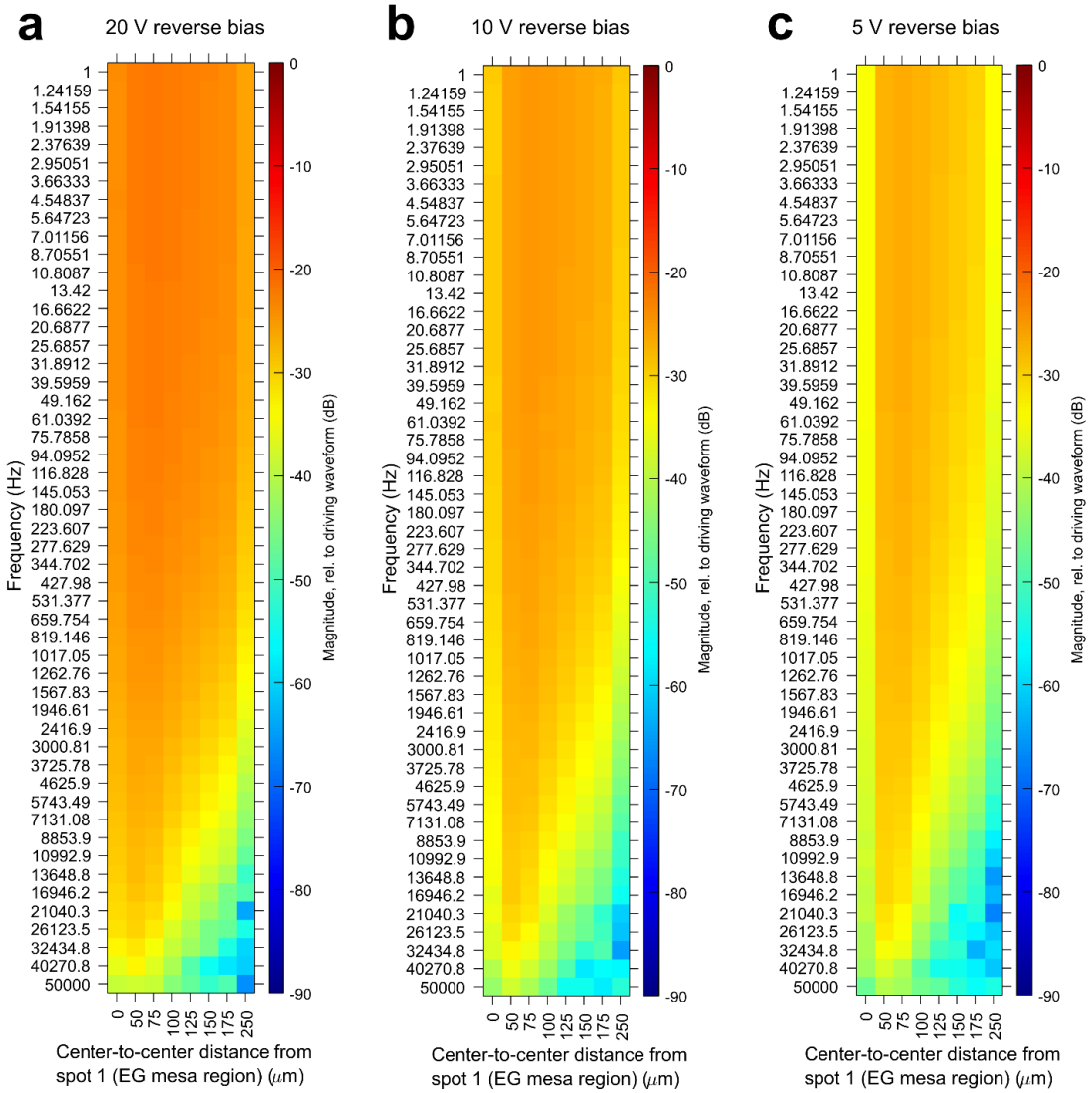

Figure 3.12: Bias dependent, spatially resolved IMPS heat maps. (a), (b), and (c) correspond to IMPS measurements taken at 20 V, 10 V, and 5 V reverse bias, respectively. Raw magnitude values are shown.

capacitance from trapping effects in the PbS CQD film, indicating that ligand-exchange[81,84], and packing density[10] have been well optimized. For the SiC geometrical

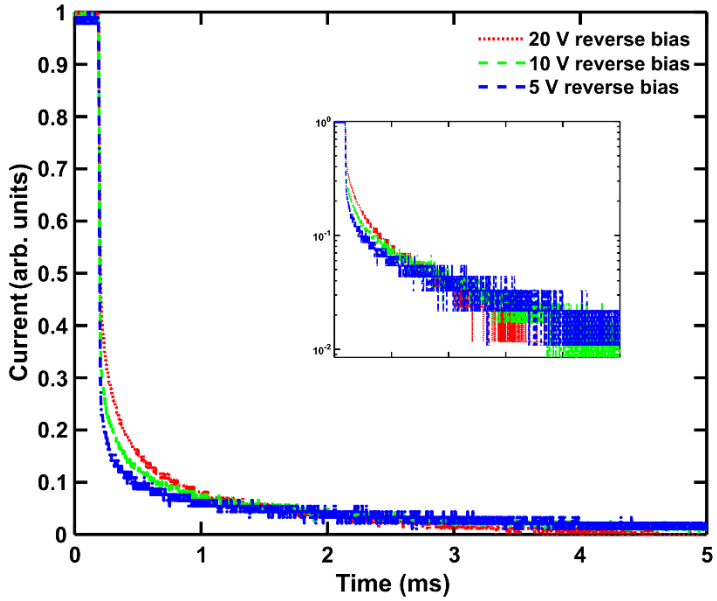

Figure 3.13: Bias dependent photocurrent transients for a QD/EG/SiC device. Transients correspond to the spot location at the off-mesa edge region. Inset shows decays on a semilogarithmic scale. Decays are normalized for clarity.

capacitance (**Experimental**), accounting for a bare surface barrier of ~1 eV, comparable to the EG/SiC barrier, we estimate:

$$C_{sh,sp} = \frac{\epsilon_{SiC} \cdot \epsilon_0}{\sqrt{\frac{2 \cdot \epsilon_{SiC} \cdot \epsilon_0}{q \cdot N_d}(1 + V_R)}} \quad (Equation\ 11)$$

which produces a value slightly (<50%) larger than experimental capacitance. The discrepancies may be due to: i) uncertainty in the SiC epitaxial layer doping extracted by capacitance-voltage at 100kHz, and/or ii) the use of a one-dimensional approximation for the TLM, which may become inaccurate at distances much greater than the device radius. Despite these uncertainties, the TLM model enabled the conclusive identification of

geometrical capacitance as the limiting factor in the bandwidth of the CQD/EG/SiC photodiode. This is consistent with findings here and our previous results[7], where SPCM at frequencies (~77-113 Hz) well below the cutoff ~10kHz (**Figure 3.9**) enabled us to safely treat the capacitances in the TLM as open circuits.

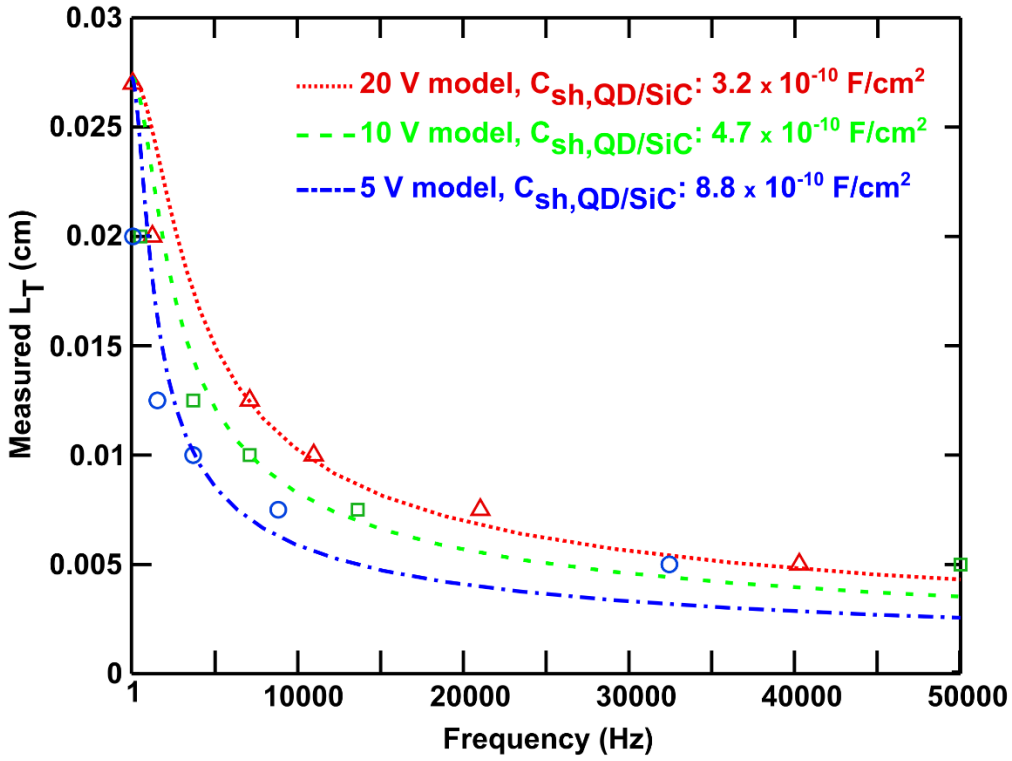

Figure 3.14: Extraction of the QD/SiC junction capacitance. Extracted transfer lengths (LT) as a function of frequency for 20 V (▲), 10 V (■), and 5 V (●) reverse bias conditions in a QD/EG/SiC hybrid device.

Key device features of the QD/EG/SiC hybrid studied here suggest the formation of a cleaner interface between the assembled QD film and underlying crystalline SiC layer than in our previous work. response (fall) times for this device were less than ~2 ms, over an order of magnitude faster. However, lower responsivities were observed, suggesting lower trap assisted photoconductive gain at the heterojunction.[11,23,66,85] Finally, the fivefold larger $R_{sh,QD/SiC}$ than previously[7] signifies a superior interface with

reduced shunting conductance from traps.[23,85] Ultimately, these results highlight the importance of nanocrystal preparation (e.g. purification[4,8], film assembly[81]) for combining solution processed materials with single crystal substrates[85,86] to form clean heterojunctions. This is particularly attractive for wide bandgap (WBG) platforms, where dual functionality of the WBG material as an optical window and photoactive layer could be used in fast devices compatible with multiple wavelengths. Given notable advances in micropatterning[87–90] and inkjet printing[91] for solution processed materials, monolithic photonics with pixel densities rapidly optimized by L_T through FTIS to balance sensitivity and bandwidth can be envisioned.

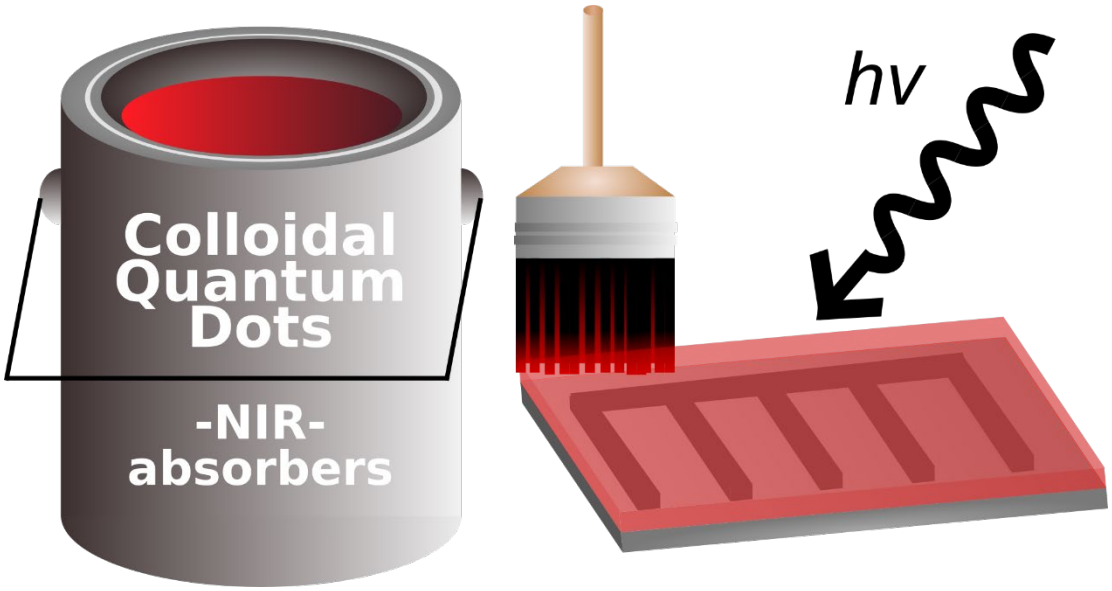

Figure 3.15: Concept graphic for strip-contact photovoltaics with printable or paintable QD layers. Stripe contacts shown underneath the red QD film. Existing photovoltaic technologies such as stripe contact Si p-n heterojunctions are envisioned as a possible platform to leverage FTIS to achieve maximal charge collection upon deposition of bandgap engineered, solution-processed layers.

3.3: CONCLUSION

The proof-of-concept scanning FTIS technique presented here demonstrates that rapid spatial mapping of composite interfaces is possible. The method may be used for

the extraction of characteristic lengths and interfacial properties, making it particularly advantageous as a rapid diagnostic method to merge speed, accuracy, and spatial registry vs. conventional time domain techniques. In the present case, a smaller area ohmic contact (EG) is used to extract current from a larger area QD/SiC rectifying junction. FTIS revealed the SiC geometric capacitance at the QD/SiC heterojunction to be the primary limiting factor of the device bandwidth. This was achieved without evaporation of a top contact, typically an architectural necessity in planar QD systems. Using small PbS QDs, we find that our QD/SiC interface is superior to our previous report, possibly due to favorable post-synthetic purification[4,8] and/or ligand exchange.[81] These findings underscore the ability to form clean junctions to single crystals with chemically prepared QDs. We anticipate that FTIS is applicable to other complex interfaces, including scalable solar cells and photodetectors with stripe contacts (**Figure 3.15**) that diminish the need for transparent conductors, making it valuable beyond the platform studied here.

3.4: EXPERIMENTAL

Estimation of $C_{sh,QD/SiC}$: To estimate the geometric depletion capacitance, we model the QD/SiC interface as a one sided, p^+n abrupt heterojunction[92] per the higher carrier concentrations (~10^{16}-10^{17} cm^{-3}) in the *p*-type PbS QD film[12] over the underlying *n*-type SiC epilayer (~10^{14} cm^{-3}) . We use the expression for junction capacitance

$$C = \frac{\epsilon_{SiC} \cdot \epsilon_0}{W} \quad (Equation\ 12)$$

, where ϵ_{SiC} is the relative permittivity of silicon carbide, ϵ_0 is the permittivity of vacuum, and W is the depletion width in SiC. For a one-sided abrupt junction, the expression for W is

$$W = \sqrt{\frac{2 \cdot \epsilon_{SiC} \cdot \epsilon_0}{q \cdot N_D}(V_{bi} - V_R)} \quad (Equation\ 13)$$

, where q is the fundamental electronic charge, N_D is the donor carrier density, V_R is the applied reverse bias potential, and V_{bi} is the built-in voltage at the interface, taken to be ~1 eV for the bare surface barrier of SiC.

CHAPTER 4: DEVELOPMENT OF LEAD-FREE QUANTUM DOT INKS AND OPTOELECTRONICS[3]

4.1: INTRODUCTION

As introduced in other earlier chapters, colloidal semiconductor quantum dots (QDs) have garnered great interest for next generation solar cells and photodetectors in recent decades due to their size tunable optical properties, compatibility with solution processing, and applicability to flexible substrates. These favorable characteristics engender the realization of low cost and scalable devices with architectures inaccessible to conventional crystalline semiconductors. Although lead and cadmium chalcogenide QDs are the most widely studied and well-understood types of QDs,[94] the advancement of environmentally friendly alternatives is crucial to minimize toxicity hazards and achieve compliance with regulatory directives. This chapter will introduce two thrusts of research: (1) the formulation of environmentally-benign $AgBiS_2$ quantum dot inks for the direct deposition of photoconductive thin films, and (2) the development of hybrid III-V quantum dot/graphene phototransistors for NIR photodetection.

4.2: $AgBiS_2$ QUANTUM DOT INKS AND PHOTOCONDUCTOR DEVICES

The ternary semiconductor $AgBiS_2$ is an appealing ecofriendly candidate for

[3] Reprinted with permission from Kelley, M. L.; Ahmed, F.; Abiodun, S. L.; Usman, M.; Jewel, M. U.; Hussain, K.; zur Loye, H.-C.; Chandrashekhar, M. V. S.; Greytak, A. B. Photoconductive Thin Films Composed of Environmentally Benign AgBiS2 Nanocrystal Inks Obtained through a Rapid Phase Transfer Process. ACS Appl. Electron. Mater. 2021, 3 (4), 1550–1555. https://doi.org/10.1021/acsaelm.0c01107. Copyright 2021, American Chemical Society.

optoelectronics. $AgBiS_2$ is a type I-III-VI semiconductor with a favorable characteristics for solar photovoltaics including a narrow bulk bandgap of ~0.8 eV,[95] a large absorption coefficient (~10^5 cm^{-1}),[96] and giant dielectric constant (~10^5).[97] $AgBiS_2$-based devices have demonstrated promising performance in recent studies. Notably, heterojunction solar photovoltaics with an $AgBiS_2$ active layer achieved a power conversion efficiency of 6.3 %,[96] and hybrid $AgBiS_2$ QD/graphene phototransistors[98] with responsivities of ~10^5 A/W were reported. However, nearly all $AgBiS_2$ device reports to date have undertaken a solid-state ligand exchange (SSLE) step during film assembly to achieve conductive thin films. Although the native long-chain ligands terminating the surface of QDs maintain colloidal stability in nonpolar solvents after synthesis, the ligands function as electrically insulating media in assembled films and impede carrier collection, which limits the device performance.[10] The ubiquitous strategy to overcome this is to replace the bulky ligands with shorter ligands, which reduces the separation distance between neighboring QDs and enhances electronic coupling, ultimately improving charge transport in the film. Although SSLE processes by spin coating are effective strategies in laboratory contexts, on larger scales throughput is limited by successive multilayer deposition iterations, which ensures that film continuity is maintained and not impinged by the stochastic formation of cracks and voids that emerge during SSLE steps. In addition, SSLE methods are completely incompatible with large area fabrication, underscoring its confinement to research settings.[99] To achieve widespread deployment of QD-based devices, it is critical to develop solution-phase exchange approaches compatible with high output single-step deposition processes such as inkjet printing or spray coating.

Many approaches for solution-phase replacement of native, long chain, electrically insulating ligands at QD surfaces have been developed. In early work by the Kagan and Murray groups[100], a flocculation-based method was utilized to exchange trioctylphosphine oxide or oleic acid ligands at semiconductor and metallic nanocrystal surfaces with thiocyanate ligands, with suspension in polar solvents such as dimethyl sulfoxide. Lateral thin film photodetectors of thiocyanate-capped CdSe QDs using this

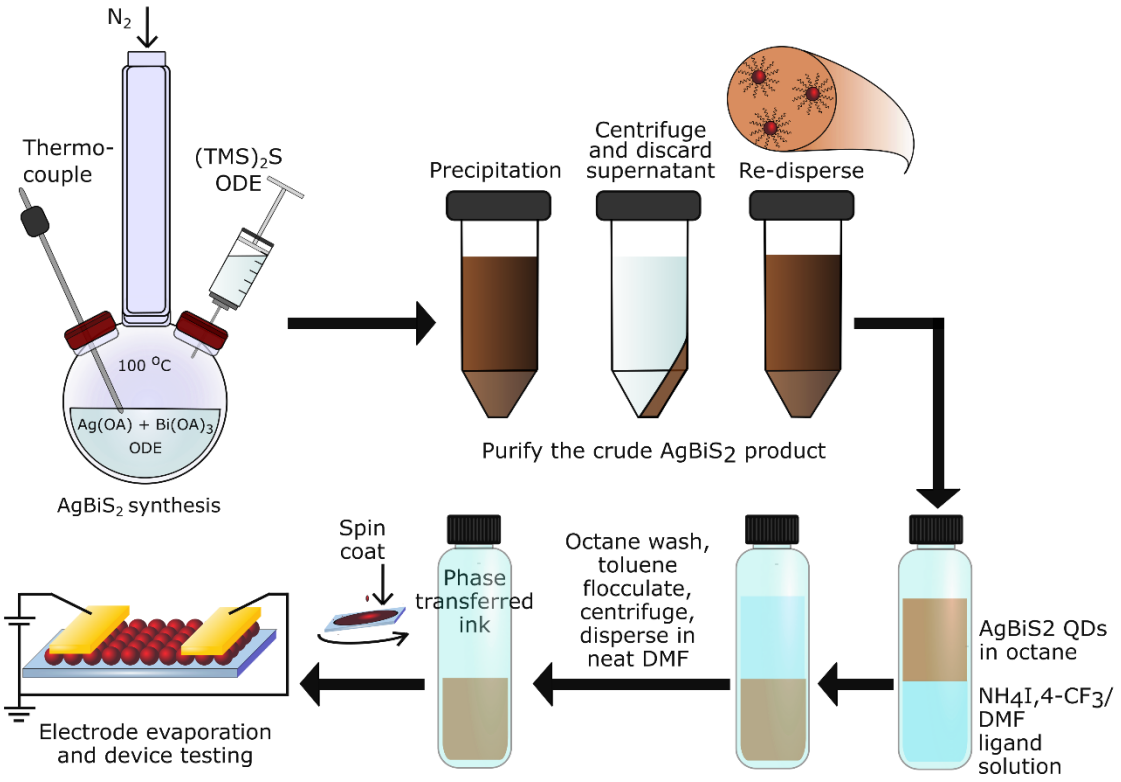

Figure 4.1: Schematic for $AgBiS_2$ ink production and device fabrication. Formation of $AgBiS_2$ QD synthesis, purification, phase transfer ligand exchange steps, and film formation are shown.

method achieved a photoconductivity as high as 10^{-5} Ω^{-1}- cm^{-1}.[100] A flocculation-based approach was also applied to oleate capped PbSe QDs[101], wherein treatment with ammonium halides yielded electrostatically stabilized dispersions in several polar solvents including *N*-methyl formamide, propylene carbonate, *N*,*N*-dimethyl formamide,

and formamide.[101] The Talapin group utilized a phase transfer method to exchange native ligands at nanocrystal surfaces with short metal chalcogenide, halide, pseudohalide, and halometallate ligands.[102,103] The method was successful in generating stable dispersions of metal chalcogenide QDs and was extended to III-V QDs and CdSe nanorods.[102,103] In PbS QDs, direct mixing of ligand solutions with QDs capped with native ligands has proven successful with cinnamic acid derivatives[22] as well as benzoic acid and 4-methylbenzoic acid.[104] Solution phase exchange of oleate with functionalized arenethiolate ligands was also reported for PbS QDs,[105] where a triethylammonium additive was employed to drive equilibrium toward generation of free thiolates and promote the displacement of bound oleate ligands. A two-step surface modification strategy was applied to InAs[106] QDs to tune the absolute band edge energy levels in assembled films. Finally, a two-step[107] cascade ligand treatment sequence was used to generate PbS QD inks suitable for bulk heterojunction solar photovoltaics in a recent report. By and large, phase transfer[108] ligand exchange methods have dominated the QD solar photovoltaic domain, with lead halides[109] most frequently used to stabilize n-type PbS QD inks and passivate the QD surfaces.

Although PbS QDs are the most widely studied semiconductor for QD optoelectronics, innovations in solution phase exchange techniques have been developed for ternary QDs as well. Choi et al. applied a phase transfer process to $AgSbS_2$ QDs[110] to generate stable dispersions in *N*-methyl formamide. Reinhold et al. applied a new strategy to $CuInS_2$ nanoparticles by directly combining the dried particles with pure 4-methylbenzenethiol with subsequent dispersion in chlorobenzene.[111] Very recently, the generation of $AgBiS_2$ inks was demonstrated using halometallate-based ligands in a

phase transfer process, and the authors achieved power-conversion efficiencies as high as 4.08% in vertical photovoltaic devices.[112] Inspired by recent advancements in producing ternary QD inks for optoelectronics, we sought a strategy to accelerate the generation of stable $AgBiS_2$ inks and investigate the fundamental properties and response of films in photodetection contexts. It was recently found that the addition of hydroiodic acid during PbS QD phase transfer ligand exchanges with lead halides strongly accelerated the transfer of QDs to the polar solvent phase.[113] The hydroiodic acid served a dual functionality where it simultaneously behaved as a strong proton source to liberate bound olefin species and provided additional iodide ions to passivate the QD surface. However, despite the promising mechanism of the acid-assisted phase transfer exchange, strong acids such as hydroiodic acid pose nontrivial safety risks, and we were motivated to identify alternatives to apply to a ternary, environmentally benign QD system. Here, we find that the inclusion of a cinnamic acid derivative to ammonium halide ligand solutions dramatically accelerates the phase transfer ligand exchange process and yields stable colloidal inks. We assemble lateral thin film devices from the inks, study the fundamental conductivity and photoconductive behavior of the films by scanning photocurrent microscopy (SPCM), and find that fast (~ms) photoresponse times are achieved in simple photodetector devices.

Preparation of our $AgBiS_2$ ink was as follows (**Figure 4.1**). Oleate-capped $AgBiS_2$ QDs were synthesized following a reported colloidal method with slight modifications.[96] The crude QD product was purified by a single precipitation-centrifugation-redispersion cycle under air-free conditions using low toxicity methyl acetate[114] as the antisolvent with a final dispersion in octane. **Figure 4.2a** shows the

powder X-ray diffraction (XRD) pattern of purified QDs overlaid with the calculated pattern for cubic $AgBiS_2$,[98,115,116] confirming the structure and phase purity of the material. To generate ligand exchanged $AgBiS_2$ inks, a phase transfer process using NH_4I salts in *N*,*N*-dimethylformamide (DMF) was adapted from the literature.[117] In brief, ammonium iodide was dissolved in DMF at a concentration of ~34 g/mL. Purified QDs in octane (~7 mg/mL) were added to the DMF solution, and the biphasic mixture was shaken vigorously to facilitate complete transfer to the DMF phase. Notably, we found that the inclusion of *trans*-4-(trifluoromethyl) cinnamic acid (4-CF3) to the ammonium iodide ligand solution rapidly accelerated the phase transfer process from over an hour to less than five seconds, similar to acid-assisted phase transfer processes with PbS QDs.[113]

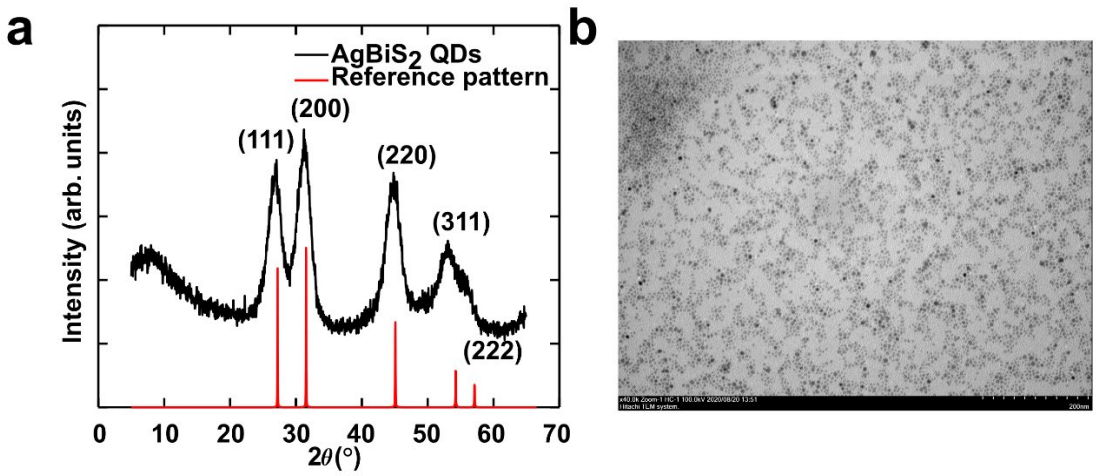

Figure 4.2: Structural information for $AgBiS_2$ QDs. (a) XRD patterns of phase-transferred AgBiS2 QDs and calculated cubic AgBiS2 reference (ICSD #AgBiS2-1959).25 (b) TEM image of phase transferred AgBiS2 QDs.

Transmission electron microscopy (TEM) confirmed the phase transfer to DMF while retaining nanoparticle form (**Figure 4.2b**), indicating that the phase transfer process has not caused significant agglomeration. We propose that the 4-CF3 additive functions similarly to hydroiodic acid in phase transfer processes, where the acidic 4-CF3 proton

liberates oleate ligands from the $AgBiS_2$ QDs and co-passivates the surfaces with iodide ligands.

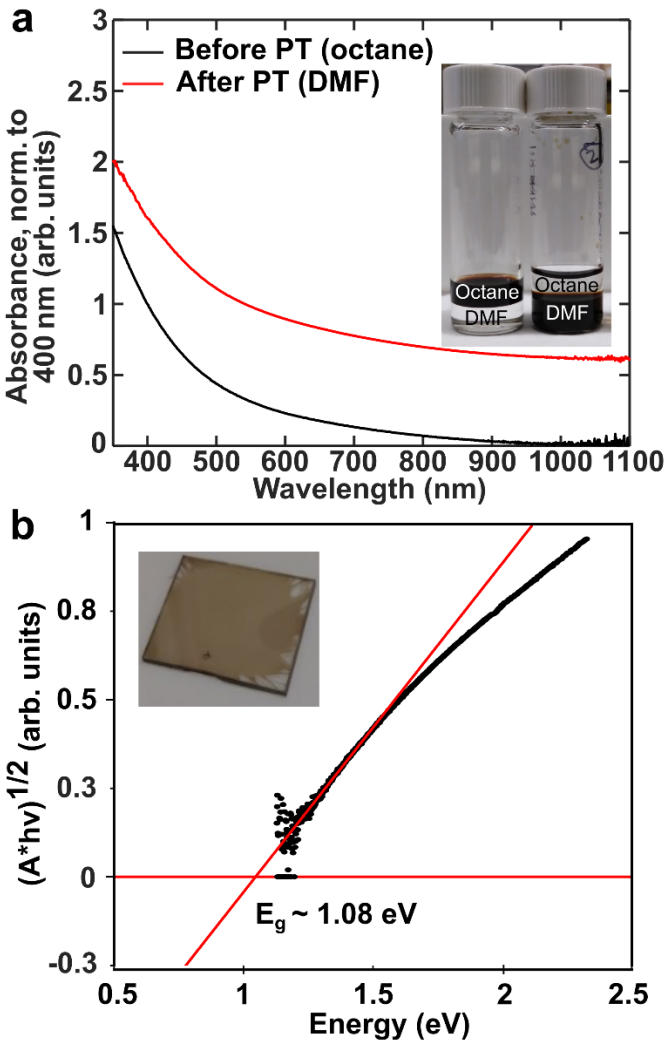

Figure 4.3: Absorbance spectra of $AgBiS_2$ QDs. (a) Absorbance spectra of AgBiS2 QDs pre-phase transfer (black) and post-phase transfer. Spectra are normalized to 400 nm and vertically offset for clarity. Inset: images of pre-phase transfer and post-phase transfer QDs showing transfer to the ligand-DMF phase. (b) Tauc plot of a AgBiS2 QD film generated from the ink. The bandgap (Eg) is obtained from linear extrapolation to the baseline. Inset: image of a phase-transferred AgBiS2 film deposited on a transparent glass sub-state.

The phase-transferred $AgBiS_2$ QDs were also characterized by absorbance spectroscopy (**Figure 4.3, 4.5**). The pre- and post-phase transfer absorbance profiles of

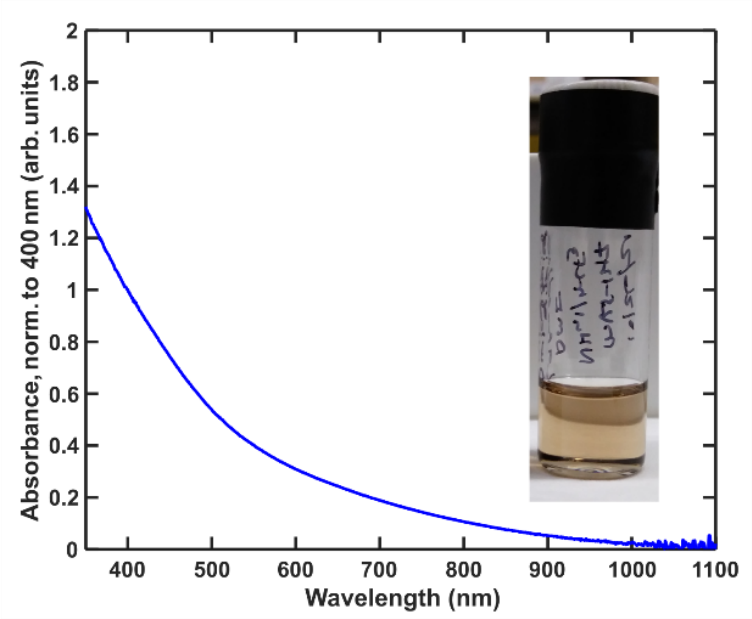

Figure 4.4: $AgBiS_2$ absorbance spectrum after several days' storage time. Absorbance spectrum is normalized at 400 nm. Inset shows the diluted $AgBiS_2$ ink in DMF.

dispersed samples were free of obvious changes, signifying that the phase transfer did not diminish the optical properties of the $AgBiS_2$ QDs. We also observed that the phase transferred $AgBiS_2$ was relatively stable, as noted by the absorption profile of dispersed QDs after several days storage time shown in **Figure 4.4**, although aggregation occurred over a period of several days.

To obtain chemical information on the $AgBiS_2$ ink, we employed scanning electron microscopy (SEM) and Energy dispersive X-ray spectroscopy (EDX) elemental mapping. **Figure 4.6a** shows a scanning electron micrograph of a spin coated phase transfer film deposited onto a cleaned glass slide. We purposely chose this region of the sample to differentiate the film from the substrate, which was partially exposed by a scratch. The elemental maps for localized Ag, Bi, and S signals are consistent with the

SEM micrograph. Importantly, elemental maps for I and F confirmed the presence of iodine and fluorine as anticipated from the halide and 4-CF3 ligands used for the phase transfer exchange. We also observed that thicker (thinner) regions of the film were

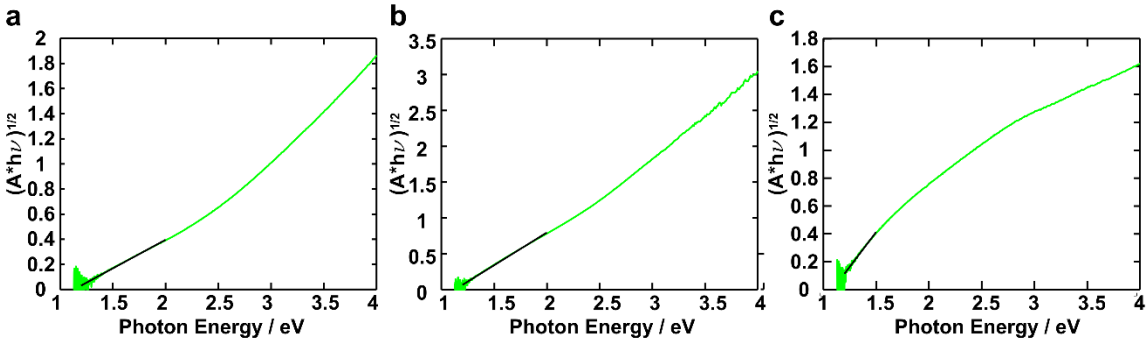

Figure 4.5: Tauc plots of AgBiS2 nanocrystal dispersions and thin film. (a) purified sample in octane, (b) phase-transferred sample in DMF, (c) thin film on transparent substrate. Extracted bandgaps for (a), (b), and (c) were 1.13 eV, 1.12 eV, and 1.08 eV, respectively.

clearly distinguished by relatively higher (lower) localized signals in the Ag, Bi, S, I, and F elemental maps. Finally, the higher intensity signal in the Si elemental map showed a clear contrast between regions holding the continuous film and the exposed underlying substrate, confirming that other signals originated from the deposition of the phase transferred $AgBiS_2$ QD film.

Having ascertained the optical and chemical characteristics of the phase transferred ink, simple two terminal devices were used to examine the optoelectronic responses of films cast from the $AgBiS_2$ ink. Glass substrates were cleaned by successive 5-minute sonication cycles in detergent, acetone, ethanol, and deionized water before blowing dry with N_2. Films were then deposited on the cleaned glass substrates under ambient conditions in a single spin coating deposition step. Metal top contacts were then evaporated directly onto the film through a shadow mask to define device regions.

Current-voltage (*I-V*) measurements at dc were taken to investigate the fundamental conductivity of the films and the dc photoresponse. From the dark *I-V* curves of these lateral devices (**Figure 4.7a**), the conductivity (σ) was obtained by the relation $\sigma = \rho^{-1}$, with $\rho = R \cdot (A/L)$, R is the resistance in ohms, L is the channel length between contacts, and A is the cross sectional film area defined by the film thickness and channel width. The σ of films was ~3×10^{-7} S/cm, comparable to early PbS QD[12] films generated in SSLE processes with dithiols and recently published work on dip-coated, ternary $NaBiS_2$ QD thin films.[118] A modest photocurrent of ~1 nA at 10 V bias was observed under wide area steady-state illumination at 444 nm (power density ~2.7 mW/cm^2). High on/off ratios ~20 for the devices were observed from the photocurrent to dark current ratio

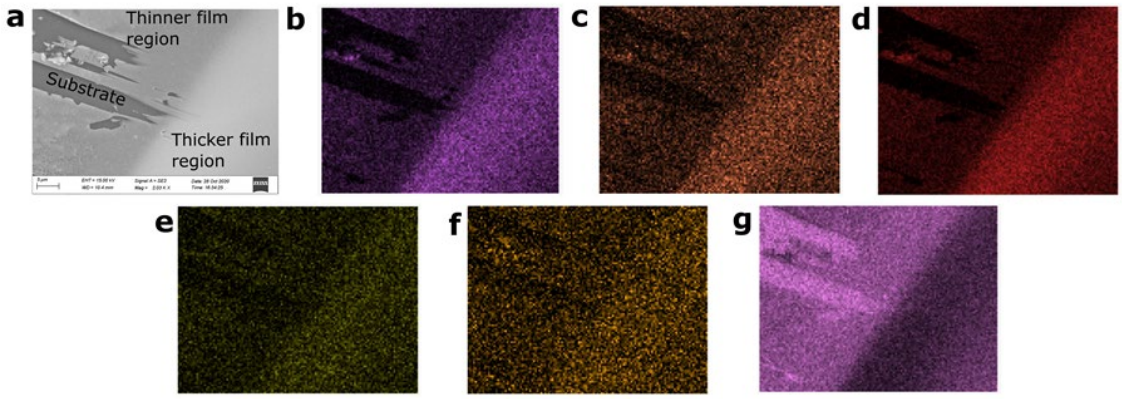

Figure 4.6: EDX spectroscopy of a phase transferred AgBiS2 QD thin film. (a) shows the scanning electron microscopy (SEM) image taken at the edge of the substrate region with a scratch for contrast. SEM-EDX elemental mapping images for (b) S, (c) Ag, (d) Bi, (e) I, (f) F, and (g) Si for the film view shown in (a). The elevated Si intensity in (g) at the location where the film has been scratched away arises from the underlying glass substrate.

(I_{ph}/I_{dark} ~ 1 nA/0.05 nA). Notably, the on/off ratios were relatively higher than lateral $AgBiS_2$ thin films formed from molecular precursors at higher temperatures and in multilayer deposition steps.[115,119]

We employed SPCM to examine the localized photocurrent generation in our lateral $AgBiS_2$ devices. SPCM is a powerful imaging technique that has been used to reveal information on carrier collection and local device responses in PbS QD devices.[120]

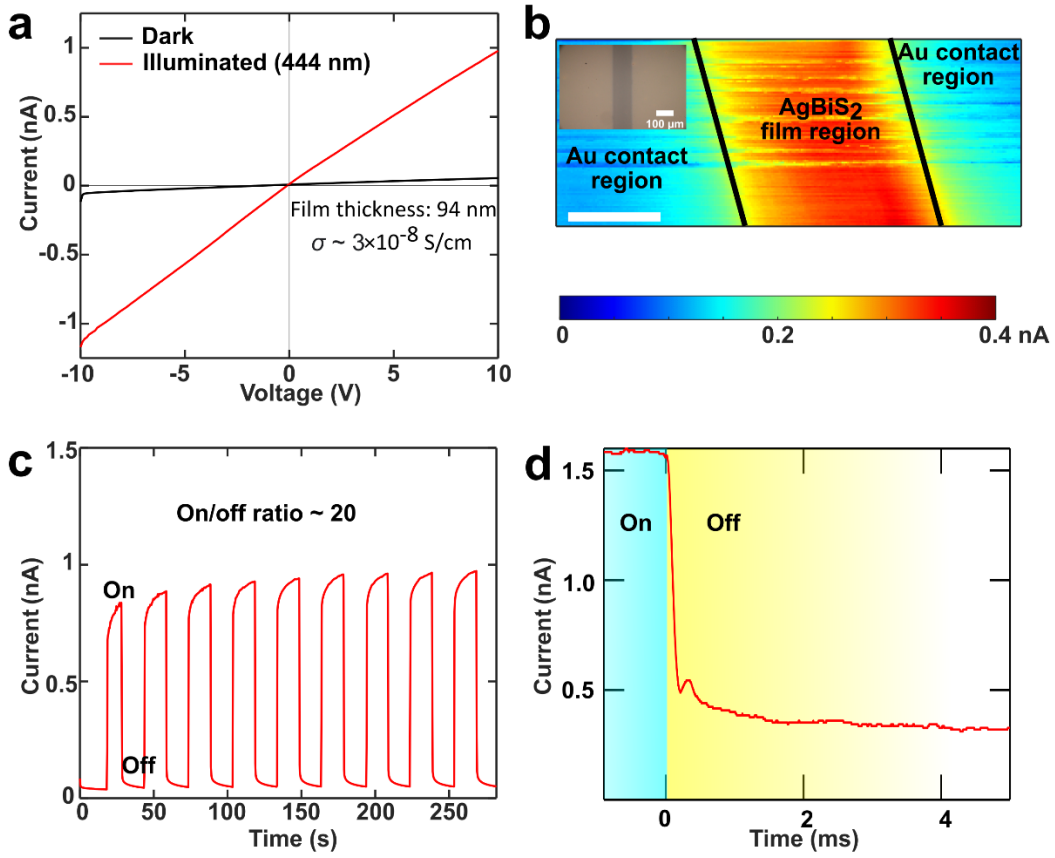

Figure 4.7: Optoelectronic characterization of $AgBiS_2$ QD thin films. (a) dark (black) and 444 nm-illuminated (red) *I-V* curves for a thin film device obtained from the NH_4I/4-CF3-$AgBiS_2$ ink. (b) SPCM of $AgBiS_2$ device (444 nm, 71 Hz). Black lines indicate electrode edges. Scalebar is 50 μm. Inset: optical microscope image of a lateral $AgBiS_2$ device showing Au contacts and the bridging $AgBiS_2$ film region; scalebar 100 μm. (c) Photocurrent transients taken on a thin film device at 10 V bias with 444 nm photoexcitation. (d) Transient at millisecond timescale.

Figure 4.7b shows a SPCM map of a $AgBiS_2$ device under 444 nm photoexcitation. We observed that the majority of photocurrent is generated within the channel region, indicative of photoconductive behavior.[120] In the context of photodetection, consistent and repeatable responses to input stimuli are necessary to achieve. To examine the

reversibility and stability of our device photoresponses, we conducted photocurrent transient measurements on the devices. As displayed in **Figure 4.7c**, the reproducibility in the device response was evident in the photocurrent transients taken under 444 nm wide area illumination (power density ~6.7 mW/cm^2), and consistent on/off ratios ~20 were maintained for several cycles. Another metric for photodetection contexts is the device response time. We found that our $AgBiS_2$ QD photoconductors were fast, with ~90% of the photocurrent decays occurring within <~4 ms as shown in **Figure 4.7d**. The fast response speed, high on/off ratio, and reversible photocurrent response highlight the promise of these environmentally benign $AgBiS_2$ inks for use in solution processed optoelectronics.

In conclusion, we have demonstrated a method for the rapid generation of eco-friendly $AgBiS_2$ QD inks. A fast phase transfer process was used to generate the QD ink, and suspensions of the phase transferred QDs were colloidally stable for several days. We have shown that photoconductivity in thin films formed from the ligand exchanged nanocrystal ink may be achieved from a single deposition step, without the need for multiple layer-by-layer deposition cycles often implemented in QD devices. The lateral photoconductive devices formed from the inks showcase high on/off ratios and fast response times, highlighting the applicability in photodetection domain. Given the established role of surface ligands in tuning band edge energy levels in deposited films[22], we postulate that the inclusion of mild proton donating additives during phase transfer ligand exchange processes could offer benefits in both the processing time and tuning the electronic properties of QD films. Overall, this work provides encouraging evidence for further developments in environmentally benign ternary QD inks for

solution-processed optoelectronics, where the advantages in scalable deposition processes such as inkjet printing or spray coating may be realized to overcome limitations encountered in commonplace solid-state ligand exchange methods. We speculate that these findings could be applicable to QD materials beyond the $AgBiS_2$ studied here.

4.3: III-V QD/GRAPHENE PHOTOTRANSISTOR DEVELOPMENT

This section describes collaborative work undertaken during my 2019 research internship at Sungkyunkwan University in Suwon, South Korea under the advisement of Dr. Sohee Jeong with support by a National Science Foundation Integrative Graduate Education and Research Traineeship (NSF IGERT) fellowship. During my stay, I had fortunate opportunities to collaborate with Dr. Munseok Jeong's and Dr. Wan Ki Bae's research teams as well as gain experience in III-V nanocrystal synthesis, purification, microfabrication, and spectroscopy. An overview of an interdisciplinary project that I worked on will be described herein.

As highlighted in earlier sections, there is strong motivation in the field to explore eco-friendly materials beyond widely studied semiconductors that contain lead, cadmium, and mercury. In NIR technologies, indium pnictogenides are appealing candidates over lead and mercury chalcogenides. Specifically, indium arsenide is a type III-V direct bandgap semiconductor that holds desirable characteristics for NIR optoelectronics including a low bulk bandgap of 0.35 eV and a low exciton binding energy of 1.87 meV that is comparable to the 4 meV exciton binding energy of PbS.[121] In addition, the large hole effective mass (m_h) of 0.40 m_h/m_0 affords flexibility in synthetic control over the particle size and effective bandgap due to strong confinement of carriers.[92] However, despite these attractive properties, the incorporation of InAs QDs in optoelectronics and

electronics has remained largely elusive in comparison to lead chalcogenides. These considerations motivated the work presented here, where we sought to study charge separation in InAs QD/graphene mixed-dimensional heterostructures and develop hybrid InAs QD/graphene phototransistors for amplified NIR photodetection, which was an interface unexplored at the time of this work.

For this work, we chose the colloidal synthetic method developed by Tamang et al.[122] and Song et al.[106] due to the capacity to achieve high quality InAs QDs with narrow size distributions via precise control over the particle sizes by continuous flow injection

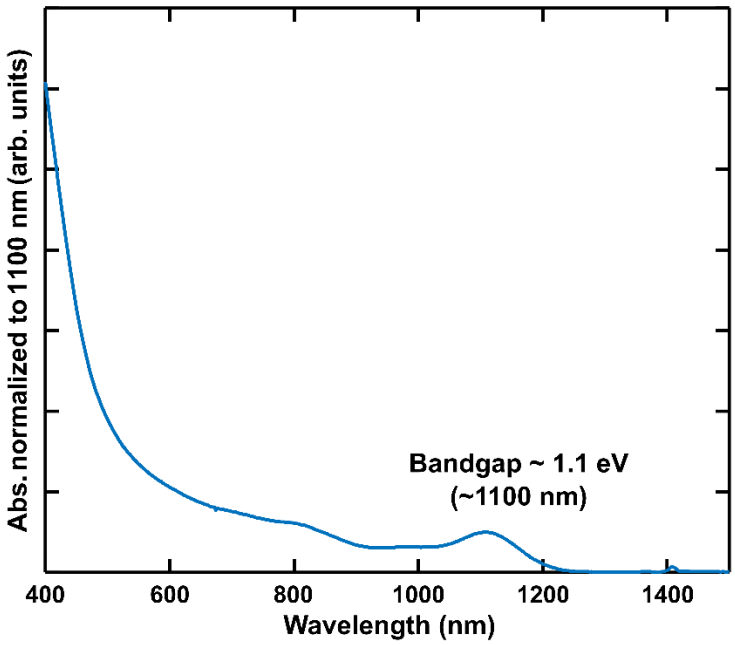

Figure 4.8: Absorbance spectra of InAs QDs. The spectrum has been normalized to the absorbance at the bandgap energy of 1.1 eV.

of pnictogen precursor. Oleate-capped InAs QDs with an effective bandgap of ~1.1 eV (**Figure 4.8**) were synthesized and purified them in a multi-step precipitation-based method[106] en route to surface modification and deposition on graphene transistors.

Prior to incorporating the InAs QDs with graphene, the characteristics of bare graphene were established. Single crystal graphene was grown by chemical vapor deposition (CVD) by collaborators. The graphene was transferred to insulating Si/SiO_2 (dry, 300 nm) substrates in a wet transfer method by Dr. Duc Anh Nguyen. Optical images of transferred graphene indicated high areal density with individual flake areas on the order of 10s of microns (**Figure 4.9**). Dr. Nguyen determined the quality, uniformity,

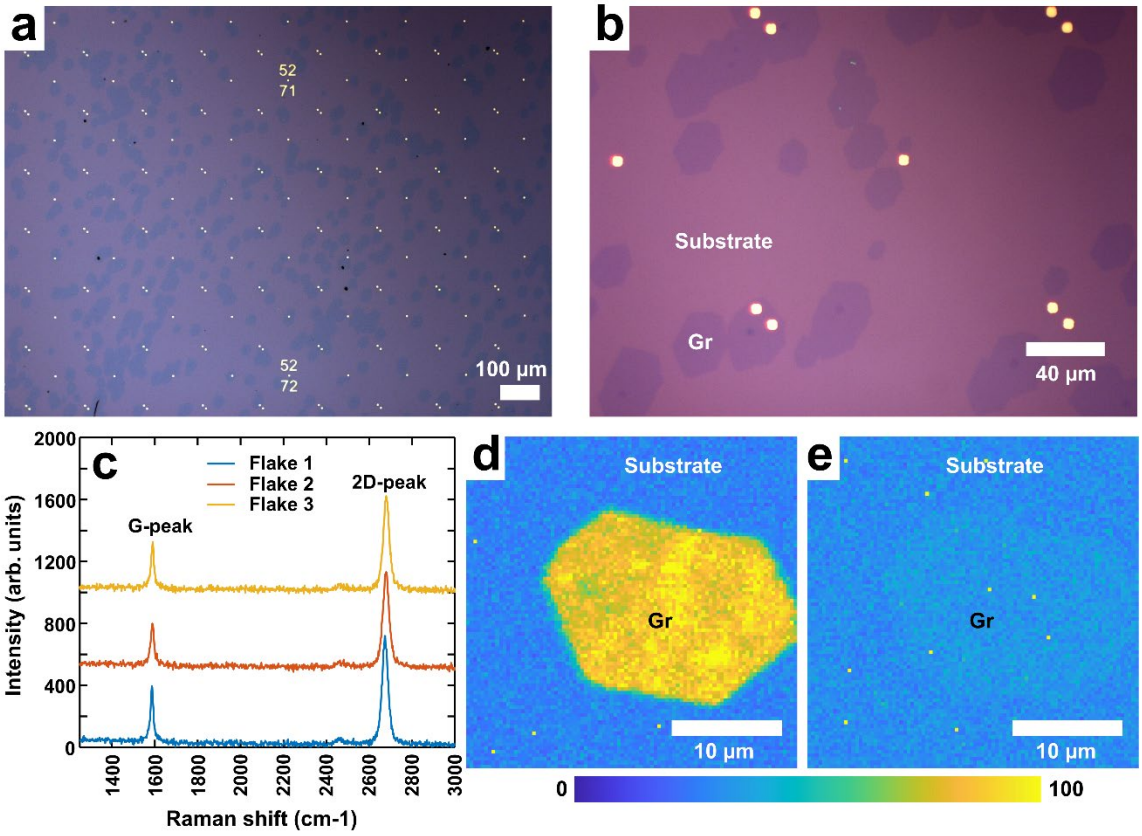

Figure 4.9: Graphene characterization. Optical microscope images of transferred graphene on SiO_2/Si substrates are shown in (a) and (b). Gold dots and numbers are lithographically defined alignment marks. (c) representative Raman spectra for 3 graphene flakes. (d) G-band and (e) D-band intensity maps taken on the same graphene flake for a 30×30 µm field of view. A 532 nm laser was used for Raman spectroscopy and microscopy.

and thickness of the transferred graphene by Raman spectroscopy and scanning Raman microscopy, as shown in **Figure 4.9**. The intensity ratio between 2D and G bands (I_{2D}/I_G)

was ~1.84, which confirmed the monolayer thickness of graphene flakes.[123] Representative Raman spectra are shown in **Figure 4.9** The spatial uniformity of the graphene flakes was confirmed by minimal D-band intensity in scanning Raman maps, making it suitable for transistor fabrication and optoelectronic characterization.

Electron beam (e-beam) lithography was used to pattern electrodes for individual graphene transistor devices. A general schematic for this process is illustrated in **Figure 4.10**. In brief, we employed computer-aided design (CAD) software to design electrode patterns. Then, poly(methyl methacrylate) (PMMA) was deposited as a resist, and e-beam lithography was used to locally expose the PMMA film according to the CAD pattern.

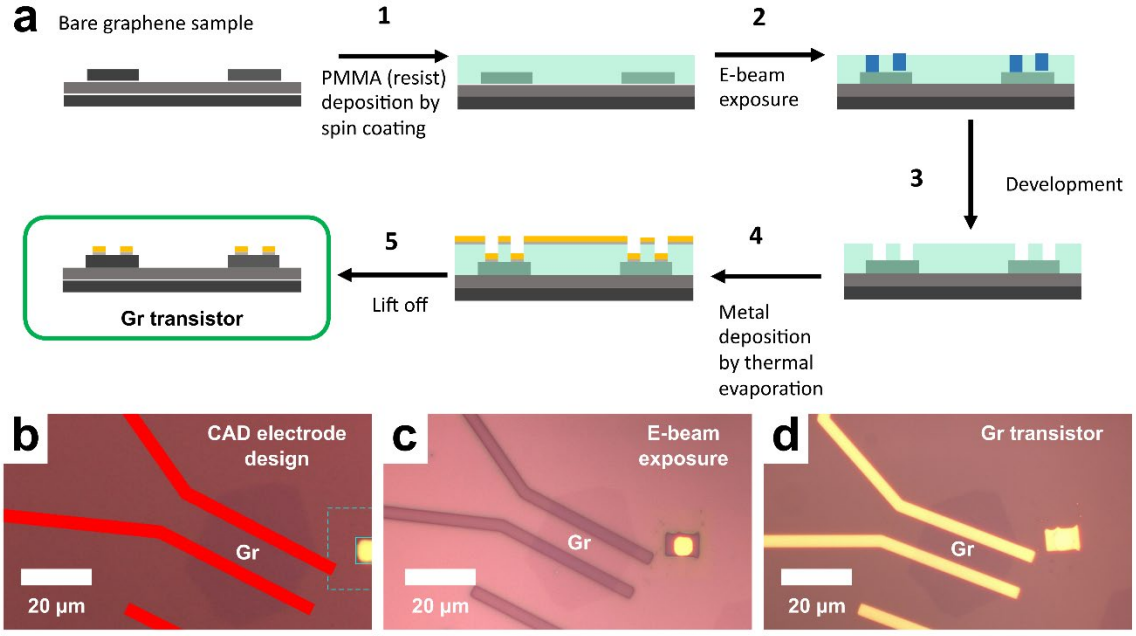

Figure 4.10: Graphene transistor fabrication. (a) schematic for graphene transistor fabrication steps following transfer to SiO_2/Si substrates. (b-d) optical microscope images of a graphene flake during various stages of the fabrication process.

The solubility of exposed PMMA differs such that it is selectively removed when submerged in a developer solution, leaving the sample exposed underneath. Thermal evaporation of Cr/Au (5 nm/45 nm) deposited the metals over the entire chip, and a final

lift-off step with acetone removed remaining PMMA leaving the metals deposited in regions exposed by the electron beam. Optical microscope images summarizing the process are also shown in **Figure 4.10**, where a representative individual graphene transistor with a channel length of ~5 μm was produced.

After successful fabrication of graphene transistors, optoelectronic characterization of the devices in the bare (pre-QD) state was undertaken. Samples were transferred to a vacuum probe station (VPS) and evacuated to a pressure of 6×10^{-3} torr. Representative transfer and *I-V* curves for a bare graphene transistor are shown in **Figure 4.11**. As shown in the transfer curves, the graphene demonstrated ambipolar conduction and was noted to be p-doped as indicated by the positive charge neutral point (CNP), which is the applied gate voltage that yields the minimum current in the graphene channel

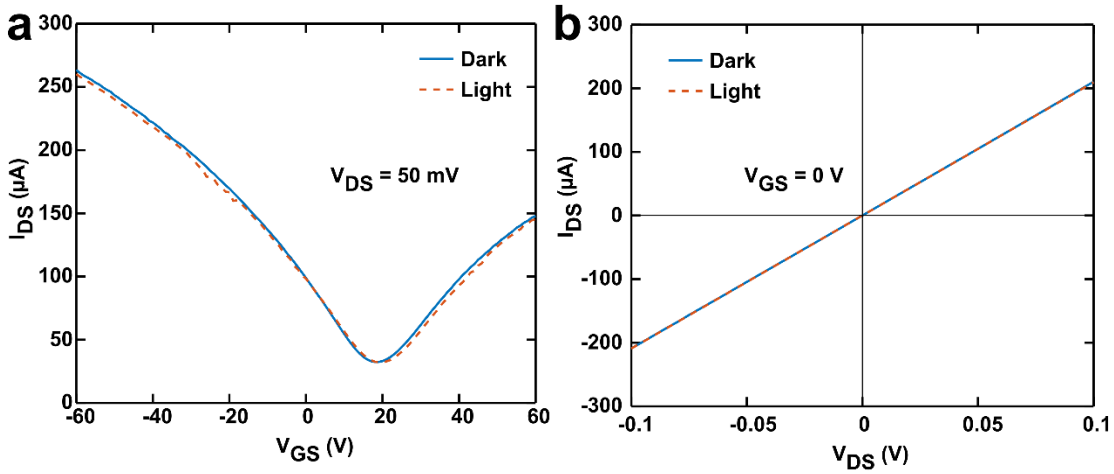

Figure 4.11: Bare graphene transistor optoelectronic characterization. (a) the drain-source current (I_{DS}) in the graphene channel is plotted against the applied gate-source voltage (V_{GS}) forming the transfer characteristic at a drain-source voltage (V_{DS}) of 50 mV. (b) shows I_{DS} as a function of V_{DS} at a constant V_{GS} of 0 V. A white light source on the vacuum probe station was used to define the light state.

and corresponds to a minimal carrier density. As expected, the bare graphene did not demonstrate a photoresponse under white light excitation. This was substantiated by

minimal or the absence of changes to the CNP in transfer curves and the slope of *I-V* curves.

Finally, InAs QDs were applied to bare graphene transistors to form the heterostructure. Notably, after QD deposition, the transfer curves showed a shift in the CNP to less positive gate voltages, suggesting relative n-doping of the graphene at equilibrium compared to the bare state. Under illumination conditions with white light, we observed an additional shift in the CNP to lower gate voltages, suggesting efficient photoinduced electron transfer across the InAs QD/graphene heterojunction. Output curves of the heterostructure are consistent with the shifts in the CNP.

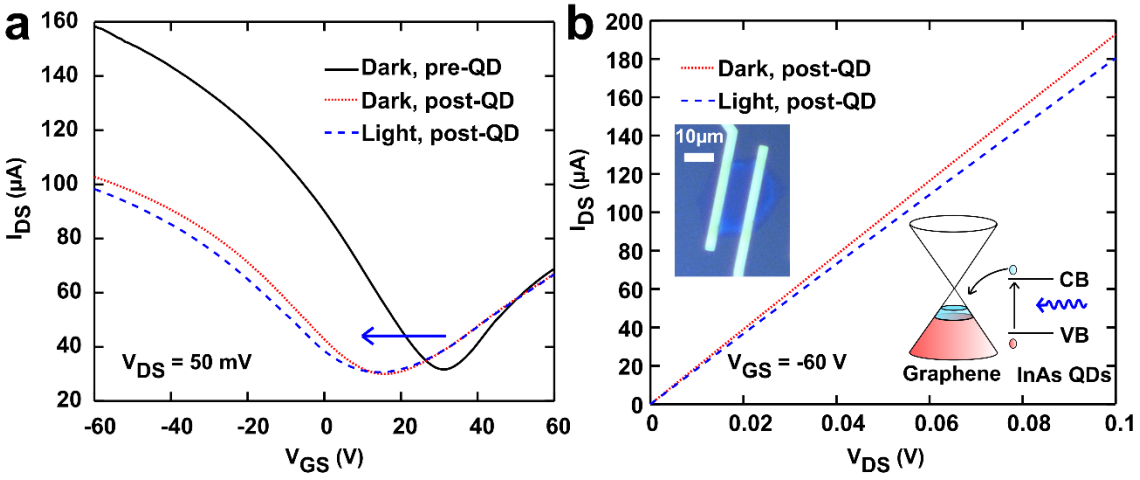

Figure 4.12: InAs QD/graphene phototransistor optoelectronic characterization (a) transfer curves of the bare graphene transistor and InAs QD/graphene hybrid phototransistor. Blue arrow shows the shift in the CNP upon deposition with QDs. Inset: optical microscope image of the InAs QD/graphene hybrid device. (b) output curves for the InAs QD/graphene hybrid device at a constant gate bias of -60 V. Optical microscope image inset shows the QD/Gr device. Cartoon graphic depicts a proposed band diagram for the interface and indicates photoinduced electron transfer from InAs QDs to the graphene channel.

Bare graphene output curves are the same The surfaces of InAs QDs were modified by etching with nitrosyltetrafluoroborate. We propose the following band diagram for the

InAs QD/graphene heterojunction, showing efficient electron transfer from the InAs QD layer to the graphene channel following photoexcitation of the QDs.

4.4: CONCLUSION

We have demonstrated two key contributions to environmentally benign QD chemistry and optoelectronics: (1) we have formulated strategies to modify surfaces of eco-friendly $AgBiS_2$ QDs generating colloidally stable inks for the direct deposition of photoconductive thin films, and (2) we have acquired evidence for photoinduced interfacial charge transfer in InAs QD/graphene heterojunctions.

4.5: EXPERIMENTAL

$AgBiS_2$ chemicals: Silver(I) acetate (Ag(OAc), ≥99 %), Bismuth(III) acetate ($Bi(OAc)_3$, ≥99 %), and ammonium iodide (NH_4I, ≥99.0 %) were purchased from BeanTown Chemical. *N*,*N*-dimethylformamide (DMF, ≥99.5 %) was obtained from Fischer Scientific. Oleic acid (≥90 %) and *trans*-4-(trifluoromethyl)cinnamic acid (4-CF3, 98 %) was purchased from Alfa Aesar. Bis(trimethylsilyl) sulfide ($(TMS)_2S$, 95 %), n-octane (97 %), and 1-octadecene (ODE, 90 %) were purchased from Acros Organics. Methyl acetate (MeOAc, 99 %) was purchased from Millipore Sigma. Octane, ODE and MeOAc were dried over activated 4A molecular sieves in a nitrogen glovebox, following degassing under partial vacuum, prior to use. All other reagents were used as received without further modification.

Synthesis and purification of colloidal AgBiS2 nanocrystals: Colloidal $AgBiS_2$ nanocrystals were synthesized using a reported procedure[96] with modifications. In a nitrogen glovebox, $Bi(OAc)_3$ (1 mmol, 386 mg), 0.8 mmol Ag(OAc) (0.8 mmol, 134 mg), and ODE (2 mL) were loaded to a 100 mL 3-neck round bottom flask. Oleic acid

(17 mmol, 4.974 g) was then added under ambient conditions, and the reaction mixture was degassed under vacuum at 100°C for 30 minutes with stirring to form silver and bismuth precursors. The reaction vessel was then charged with nitrogen gas, and TMS_2S (1 mmol, 210 μL) diluted in 5 mL of ODE was swiftly injected at an injection temperature of 100°C, forming the crude, brown reaction product. The crude product was cooled to room temperature with the heating mantle in place. The flask was protected from light until the precipitation step.

$AgBiS_2$ nanocrystals were purified under air free conditions using MeOAc and octane as the antisolvent and solvent, respectively. The purified sample was stored in a nitrogen glovebox in octane until further use.

$AgBiS_2$ phase transfer ligand exchange and ink formation: In a typical phase transfer ligand exchange process, purified $AgBiS_2$ nanocrystals in octane (~7 mg/mL) were added to a single solution of NH_4I (~34 mg/mL) and 4-CF3 (~10 mg/mL) in DMF under ambient conditions. The phase transfer vessel was then shaken vigorously for ~5 seconds, and the $AgBiS_2$, and the nanocrystals completely transferred to the bottom DMF phase to leave a clear top phase. The top phase was removed with a pipette, and the dark DMF phase was rinsed twice with neat octane.

To form the ink used for photoconductive thin films, the washed DMF phase was flocculated with toluene, centrifuged, and separated from the supernatant. The remaining $AgBiS_2$ was dried under vacuum for ~20 minutes and re-dispersed in neat DMF to achieve a concentration of 150 mg/mL. The ink was then centrifuged for 2 minutes and the supernatant carefully separated from any sediment to a new vessel. The ink was filtered through a 0.1 μm PTFE syringe filter prior to spin coating.

$AgBiS_2$ device fabrication and electronic measurements: Films were deposited on rotating glass substrates using a single step deposition. Metal (Au) contacts were evaporated on top of the film through a shadow mask, forming lateral 2-terminal devices ~200-400 μm wide at various spacings ~115 μm. Contact pads were gently probed with flexible tungsten microprobes to avoid damage to films.

A Keithley Source meter unit was used to record *I-V* measurements in the dark, and under wide area illumination (444 nm, ~2.7 mW/cm^2) with a diode laser (Toptica). The optical power density was calibrated using a silicon power meter (Thorlabs). Photocurrent transient measurements were conducted with the Keithley Source meter unit with dark states achieved by chopping the beam (set to ~6.7 mW/cm^2) with a custom-built optical shutter. Scanning photocurrent microscopy was undertaken using our previously reported setup with 444 nm photoexcitation modulated at a frequency of 71 Hz.[7,26]

$AgBiS_2$ materials characterization: UV-visible absorbance spectra were taken on a Thermo Scientific Evolution Array spectrometer. TEM was taken on a Hitachi HT7800 TEM using carbon coated copper grids (Ted Pella) as supports. PXRD was obtained on a Bruker D2 Phaser using a Cu source (K-α: 1.5418 Å) and step size of 0.02° at an operating voltage and current of 30 kV and 10 mA, respectively. SEM and EDX maps were taken on a Zeiss Gemini500 Thermal Field Emission Scanning Electron Microscope.

InAs QD chemicals: All reagents for the synthesis, purification, and surface modification of InAs QDs were obtained and used as described in Song et al.[106]

InAs QD synthesis and purification: InAs QDs were synthesized using the method established by Song et al.[106] In brief, seed InAs nanocrystals were prepared as follows. Indium precursor was generated by dissolving indium(III) acetate (1 mmol, 0.29 g) and oleic acid (3 mmol, 0.85 g) in degassed 1-octadecene (5 mL) in a three-neck round bottom flask (100 mL) equipped with a Teflon stirring bar. The reaction mixture was degassed at 120 C under vacuum for 2 hours under stirring to form the white transparent In-oleate precursor. Dioctylamine (1.5 mmol, 0.36 g) and distilled tris(trimethylsilyl) arsine (TMS_3As) (0.5 mmol, 0.14 g) were dissolved in 1 mL of degassed 1-octadecene in a nitrogen glovebox forming the brown As precursor and heated at 60 C on a hotplate for 10 minutes. After degassing the In-precursor, the temperature was elevated to 300 C and the flask was switched to a nitrogen environment, followed by swift injection of the As precursor. The flask was maintained at 300 C under stirring until introduction of InAs nanoclusters.

InAs nanoclusters were prepared as follows. In a 100 mL three neck round bottom flask, indium(III) acetate (6 mmol, 1.75 g) and oleic acid (18 mmol, 5.18 g) were dissolved in 30 mL 1-octadecene and stirred under vacuum for 2 hours at 120 C. The As precursor was prepared in a nitrogen glovebox by dissolving TMS_3As (3 mmol, 0.84 g) and dioctylamine (9 mmol, 2.16 g) in 6 mL 1-octadecene with heating at 60 C for 10 minutes. The reaction mixture was switched to a nitrogen environment and stirred at room temperature prior to fast injection of the As precursor.

For forming InAs QDs, the dark tan InAs nanocluster solution was loaded to a 20 mm diameter 24 mL syringe. The nanoclusters were injected to InAs seeds at 300 C at a continuous rate of 0.45 mL/min.

The crude InAs QDs were purified by four successive precipitation and redispersion cycles as follows. The crude InAs QDs were partitioned into three centrifuge tubes with QD volumes of ~15 mL each. Butanol was added to achieve a total volume of 40 mL, and the samples were centrifuged at 6000 rpm for 5 min. The supernatant was discarded, and the precipitate was dispersed in 10 mL hexane. Butanol was added to achieve a total volume of 25 mL, and the mixture was centrifuged at 4000 rpm for 5 min. The supernatant was collected, and 20 mL of butanol was added followed by centrifugation at 6000 rpm for 5 minutes. Finally, the precipitate was isolated from the supernatant and dispersed in 10 mL of hexane with 40 mL butanol added followed by centrifugation at 6000 rpm for 5 minutes. The final precipitate was collected and dispersed in octane until further use.

Surface modification of InAs QDs by $NOBF_4$: Prior to film formation, the surfaces of InAs QDs were etched following the procedure by Song et al.[106] In brief, to 4 mL of a 200 mg/mL solution of purified InAs QDs, 10 mL of 0.02 M $NOBF_4$ in DMF was added in a centrifuge tube. The QDs transferred to the polar DMF phase with mild shaking, and the clear top layer was removed by a pipette. Neat hexane was added to the dark DMF phase and the biphasic mixture was shaken. Upon settling to two phases, the clear hexane phase was removed, and this process was repeated two more times for a total of three hexane rinses. Finally, neat toluene was added to the DMF phase to precipitate the QDS, and the mixture was centrifuged at 6000 rpm for 5 minutes. The supernatant was discarded, and the etched InAs QD precipitate was dried under vacuum before final redispersion in neat DMF.

Film formation for InAs/QD phototransistors: A solid-state ligand treatment procedure was used to form films of InAs QDs on graphene transistors. To the substrate rotating continuously at 2500 rpm, 20 μL of etched QDs (~100 mg/mL) was administered. The substrate was stopped and annealed on a hotplate at 100 C for 2 minutes. The substrate then resumed rotation at 2500 rpm, and 6 drops of a 1 % (*w/v*) NH_4Cl/methanol solution was added drop-wise to the InAs QD film. The substrate was allowed to spin for 30 seconds to dry, and 10 drops of neat methanol was added dropwise to the rotating substrate to rinse away excess NH_4Cl, followed by 30 seconds of a rotating time for drying. The sample was then stored in a vacuum cabinet until optoelectronic device testing in a vacuum probe station.

CHAPTER 5: SELF-ASSEMBLY OF FLUORESCENT DIFFRACTIVE ELEMENTS FROM QUANTUM DOTS USING MAGNETIC NANOPARTICLE TEMPLATES

5.1: INTRODUCTION

This work describes ongoing efforts on an interdisciplinary collaboration with Dr. Thomas Crawford's research team at the University of South Carolina. The goal of this project is to interrogate nanoscale self-assembly in solution-processed materials, which can be challenging to achieve due to the diffusive motion of suspended particles in fluid media. We study the uptake of fluorescent semiconductor QDs holding well-defined surfaces onto magnetic nanoparticle arrays and investigate emergent diffractive and fluorescent phenomena, which can hold significance in the design of low-cost solution processed diffractive surfaces for spectroscopy, high precision lasing, and transparent holographic displays.

Diffraction is a phenomenon where a traveling wave encounters an aperture or obstacle resulting in a bent or spread path of propagation. Many sources including sound, light, and massive particles with wavelike properties (e.g. atoms, electrons, neutrons) diffract if the encountered apertures or obstacles are on the order of the source's wavelength. The wavelength of matter waves such as that for electrons is described by the de Broglie wavelength $\lambda = (h/mv)$, where h is Planck's constant, m is the particle mass, and v is the particle velocity. Taking electrons as an example, small wavelengths ($\sim 10^{-12}$ m) can be achieved depending on the particle velocity, which can be controlled by an applied electric field. This principle is widely leveraged in electron microscopy,

where high (~≤10^{-12} nm) resolution is achieved and surpasses diffraction limits of visible photons in optical microscopes. On the other hand, optical diffraction is commonly

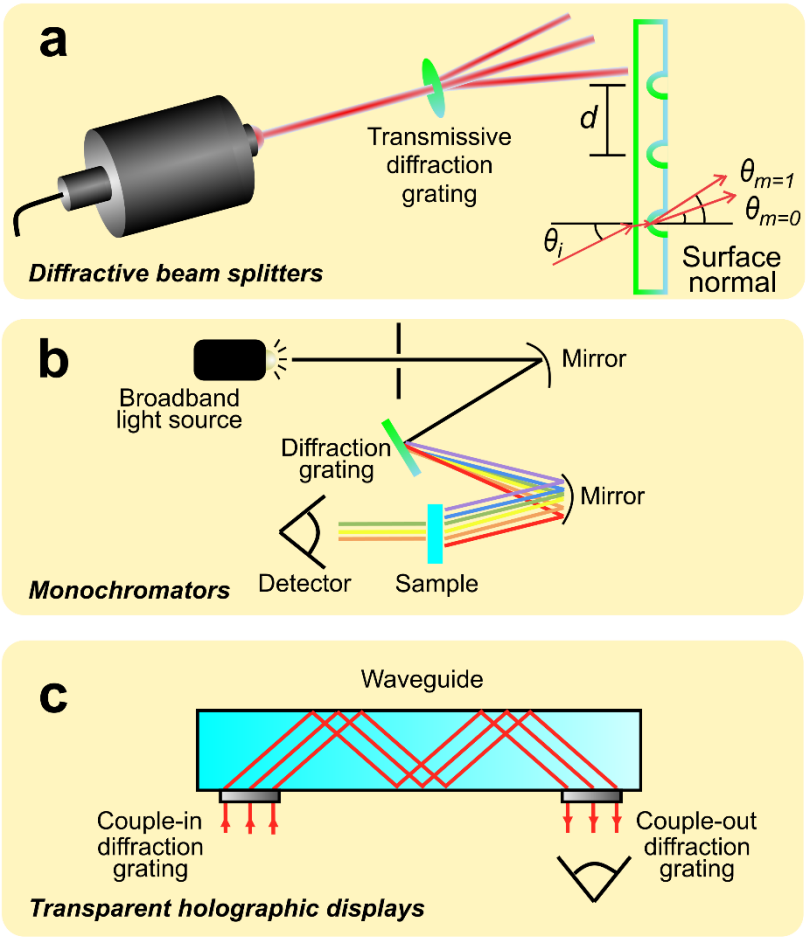

Figure 5.1: Optical diffractive elements and applications. (a) shows general concept for transmissive diffraction gratings, where d is the element spacing, θ_i is angle of incidence, and θ_m are the angles of diffraction for m modes. (b) illustrates an application of blazed diffraction gratings used in spectrometers. (c) highlights the concept of holographic waveguides with coupled input/output diffraction gratings where internal reflection within the waveguide is maintained in accordance to Snell's law.

utilized in diffraction gratings, which may be conceptualized as an optically flat surface containing uniformly spaced protrusions or slits that diffract light in a controllable manner for desired application needs (**Figure 5.1**). The classification of diffraction

gratings as transmissive or reflective depends on the propagation path of diffracted beams after encountering the diffraction grating.

$$\theta_m = \arcsin\left(sin\theta_i - \frac{m\lambda}{d}\right)$$

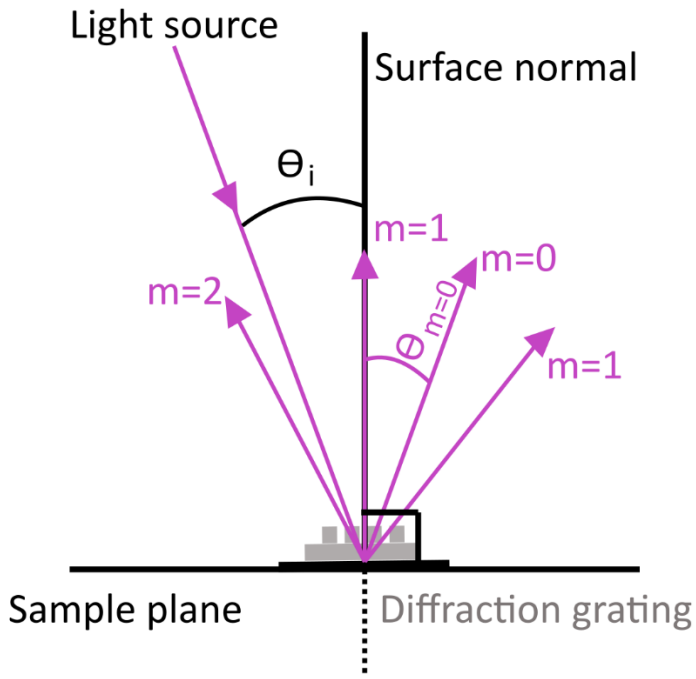

Figure 5.2: Ray optics diagram for a plane reflective type diffraction grating.

For reflective type diffraction gratings, the relationship between reflective diffraction gratings is expressed in **Equation 14**,

$$m\lambda = d(sin\theta_i - \theta_m) \quad (Equation\ 14)$$

where m is the diffraction order, λ is the wavelength of incident or diffracted light, d is the pitch distance between repetitive elements (e.g. grooves or slits) defining the grating, θ_i is the angle of incident light relative to the grating normal, and θ_m is the angle of diffracted light relative to the grating normal. This is shown conceptually in **Figure 5.2**,

where ray diagrams for diffraction modes of a plane reflective type diffraction grating are illustrated.

Because optical diffractive elements operate with visible wavelength photons, uniform nanometer-scale fabrication of features on the grating surface is key. However, the reliable manufacturing of such features is burdened by costly fabrication methods including photolithography or ruling engines. To overcome this, there is motivation to develop approaches using solution-processed nanomaterials as building blocks to form diffractive optical surfaces. Shallcross et al.[124] demonstrated that mechanical methods such as microcontact molding are effective strategies to form diffraction gratings from colloidal CdSe QDs. The authors used a master poly(dimethylsiloxane) (PDMS) microstamp to form transmissive diffraction gratings and coupled in-out internal reflection elements on transparent substrates from dropcast CdSe QDs capped with trioctylphosphine oxide and hexadecylamine. The method afforded remarkable control over grating groove spacings *d* spanning ~270 - 840 nm, making it a viable method for diffraction in the visible regime.

Beyond mechanical methods, the formation of diffractive elements from solution-processed nanomaterials by self-assembly is a promising route for large area fabrication. Yang et al. formed diffraction gratings operating in the visible regime from self-assembled zirconia (ZrO_2) NP arrays.[125] The authors utilized polymer pen lithography (PPL) to define localized hydrophilic regions contrasting with hydrophobic regions passivated by 1-octadecanethiol. Submersion of the substrates in aqueous ZrO_2 dispersions facilitated local assembly of the nanoparticles to the hydrophilic regions defined by PPL. Similarly, directed assembly of polystyrene microspheres has been

reported on substrates with patterned hydrophobicity[126], and hydrophobic effects have been reported to reversibly induce the self-assembly of gold nanoparticles stabilized with hydrophobic polystyrene.[127] It would be valuable to obtain further information on the fundamental interactions and rates of assembly for colloidal nanomaterials to aid in the

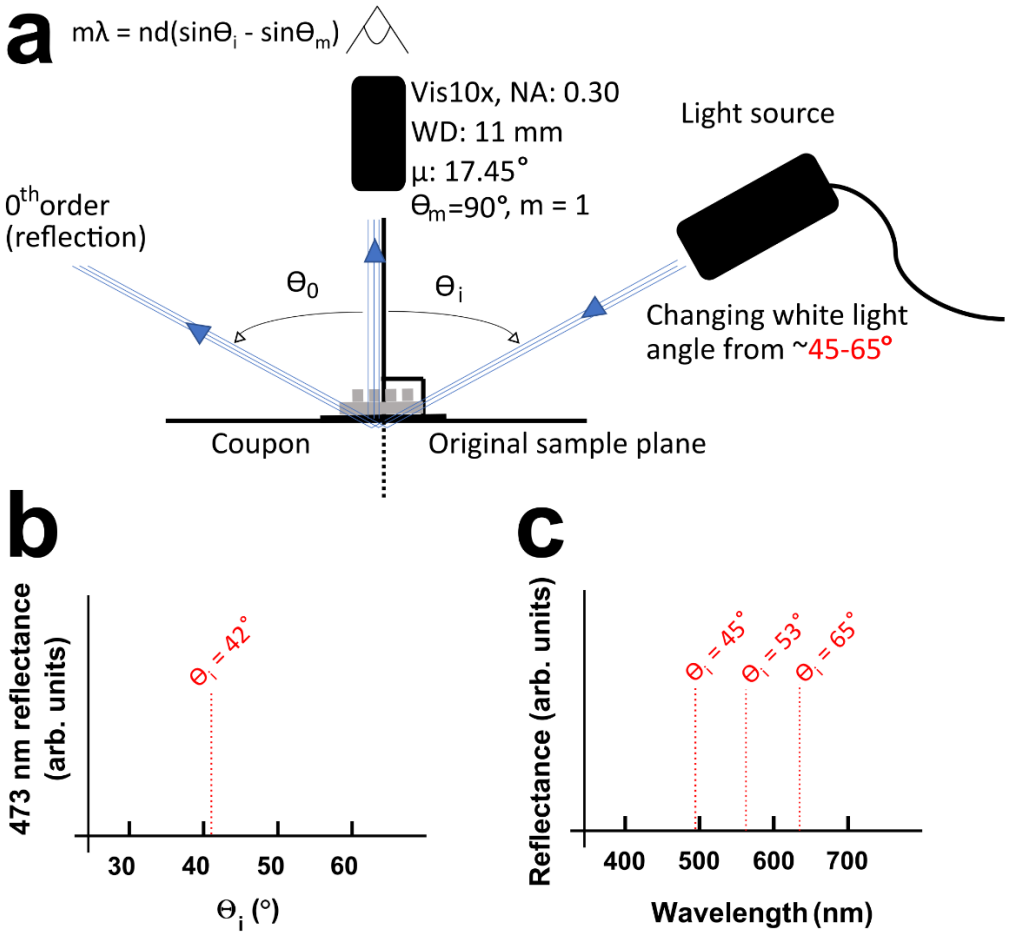

Figure 5.3: Pre-QD ray optics diagram and goniometer experimental setup.(a) shows a general schematic for measuring Fe_3O_4 nanoparticle diffraction gratings with line spacing d = 700 nm. (b) shows a simulated relative intensity of diffracted 473 nm light from a white light source for a d = 700 nm grating. (c) shows simulated reflectance spectra for the same grating under different θ_i conditions.

design of ordered structures including diffractive optical elements. Taken into consideration, this project seeks to uncover such insights on hydrophobic self-assembly

by examining the uptake and fluorescent behavior of oleate-capped QDs assembled onto magnetically patterned diffractive arrays of oleate-capped Fe_3O_4 nanoparticles.

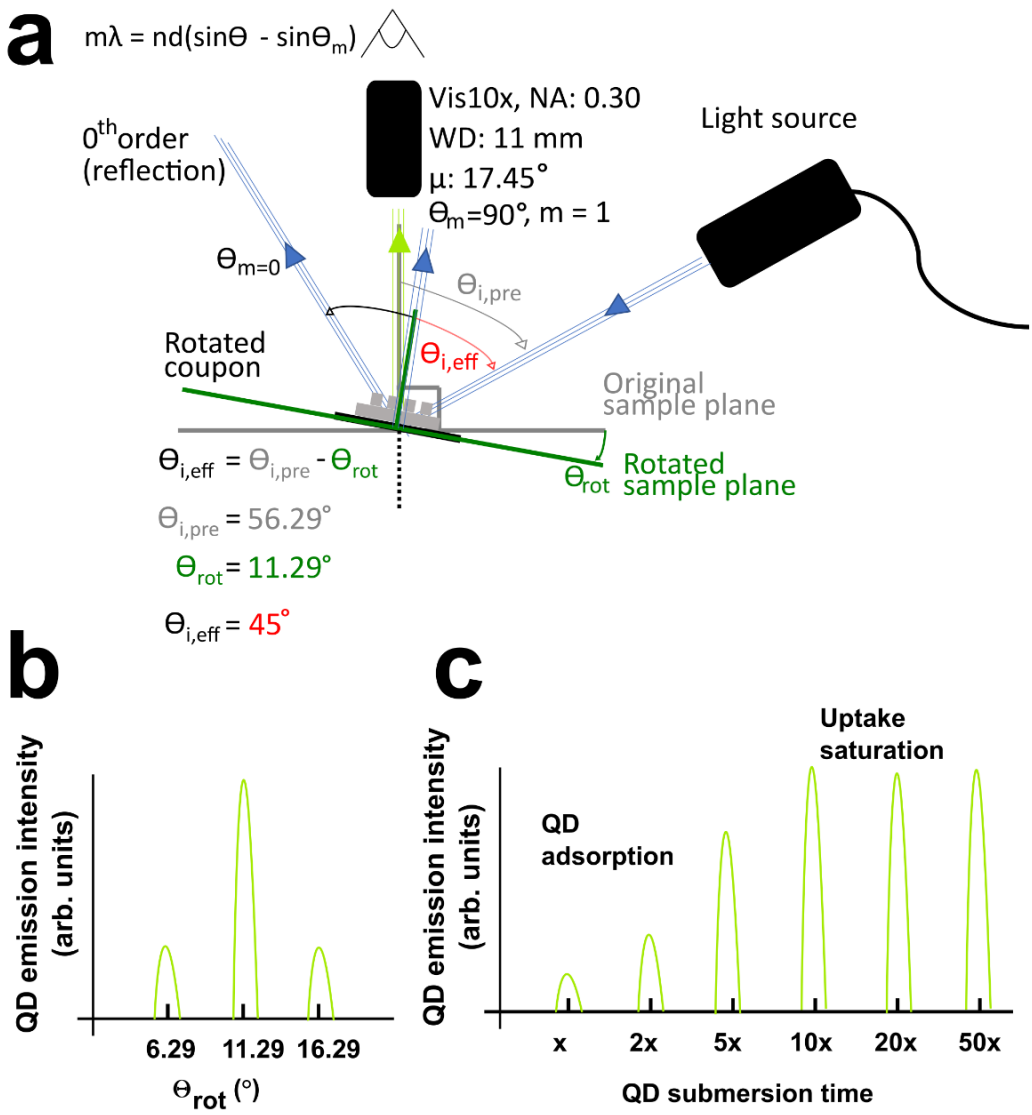

Figure 5.4: Post-QD ray optics diagram and goniometer experimental setup. (a) shows a general schematic for the exotic optical phenomena arising from in-plane fluorescence of self-assembled QD arrays spaced by distance d = 700 nm. (b) Relative intensity of QD fluorescence as a function of the stage rotation angle from the original sample plane, showing enhanced intensity of 563 nm. (c) concept graphic for evolution of the enhanced fluorescence intensity for a series of gratings submerged in QD dispersions at times showing initial uptake and saturation regimes.

To study the diffractive behavior of Fe_3O_4 gratings, a microspectrometer setup equipped with a custom-built goniometer stage will be employed. A general schematic of the setup is illustrated in **Figure 5.3**. In brief, θ_i is modulated by rotating the illumination source with a rotation stage. The stationary objective lens on the microspectrometer constrains θ_m to an angle of 90°, allowing the evolution of the wavelength of diffracted light from an incident broadband white light source to be detected exclusively as a function of θ_i.

Hydrophobic self-assembly of fluorescent QDs onto the Fe_3O_4 nanoparticles is hypothesized to impart an exotic optical fluorescence effect following submersion of the Fe_3O_4 nanoparticle gratings in QD dispersions. A schematic of the behavior is illustrated in **Figure 5.4**. In brief, if localized hydrophobic self-assembly of QDs onto regions holding the Fe_3O_4 nanoparticles occurs, the formation of QD arrays defined by the patterned Fe_3O_4 nanoparticles will be achieved. In addition to diffraction of incident light, in-plane fluorescence of the patterned QDs may provide enhanced intensity of light at the QD emission maximum depending on the diffraction grating pitch, wavelength of incident light, and wavelength of QD fluorescence. Such an effect could be observed by judiciously choosing these parameters (**Figure 5.7**) in order to resolve the fluorescence signal from background, which is composed of the emission from QDs in all directions. If observed, there should be a distinct difference in fluorescence intensity that may be monitored under a series of conditions for assembly. The submersion time of Fe_3O_4 gratings in QD dispersions could yield detectable differences in the uptake of the QDs, which may reach a saturation state on long timescales (**Figure 5.4)**. Monitoring this uptake saturation in different solvents could provide information on the rates of

hydrophobic self-assembly. Here, preliminary results on research efforts in processing visibly fluorescent QDs and assembly onto the Fe_3O_4 nanoparticle arrays will be shown.

5.2: PRELIMINARY RESULTS

The initial step of this project was to isolate visibly fluorescent and stable QDs using a repeatable process suitable for further experimentation. Initially, CdSe/CdS QDs with an effective bandgap of 564 nm and emission maximum of 573 nm were synthesized by John following reported methods. Then, I purified the QDs by GPC using reported techniques with a toluene mobile phase.[7,8] The proton NMR spectra in **Figure 5.5** indicate that the purified QDs were free of unbound olefin ligands and the ODE growth solvent. The optical characteristics of the QDs were preserved following GPC purification as shown by the absence of changes to the pre- and post-GPC absorbance and fluorescence profiles in **Figure 5.5**.

Having validated the processing steps to establish an initial state of the QDs, the assembly of the QDs on Fe_3O_4 nanoparticle diffraction gratings was investigated. Firstly, diffraction gratings were prepared by Abdul Rahman Mohtasebzadeh.[128] A dark field optical microscope image of the investigated diffraction gratings with spacings *d* spanning 25 nm to 3000 nm is shown in **Figure 5.6**. The GPC purified toluene stock solution was diluted heavily in neat toluene to for a submersion stock. After submersion in the diluted QD stock solution, gratings were preserved, and the dark field optical microscopy image indicated the formation of coffee-ring regions of accumulated QDs due to the drying process (**Figure 5.6**). The presence of QDs in the coffee-ring region was confirmed by fluorescence microscopy.

Notably, not only were patterned features of the Fe_3O_4 nanoparticle gratings preserved after submersion in QDs, the localized self-assembly of QDs was confirmed by fluorescence microscopy, as shown in **Figure 5.6**. In addition, the emission spectra of the grating post-QDs showed strong agreement with standalone QD dispersions in **Figure 5.5**, further validating the presence of the QDs. In contrast, the bare diffraction grating

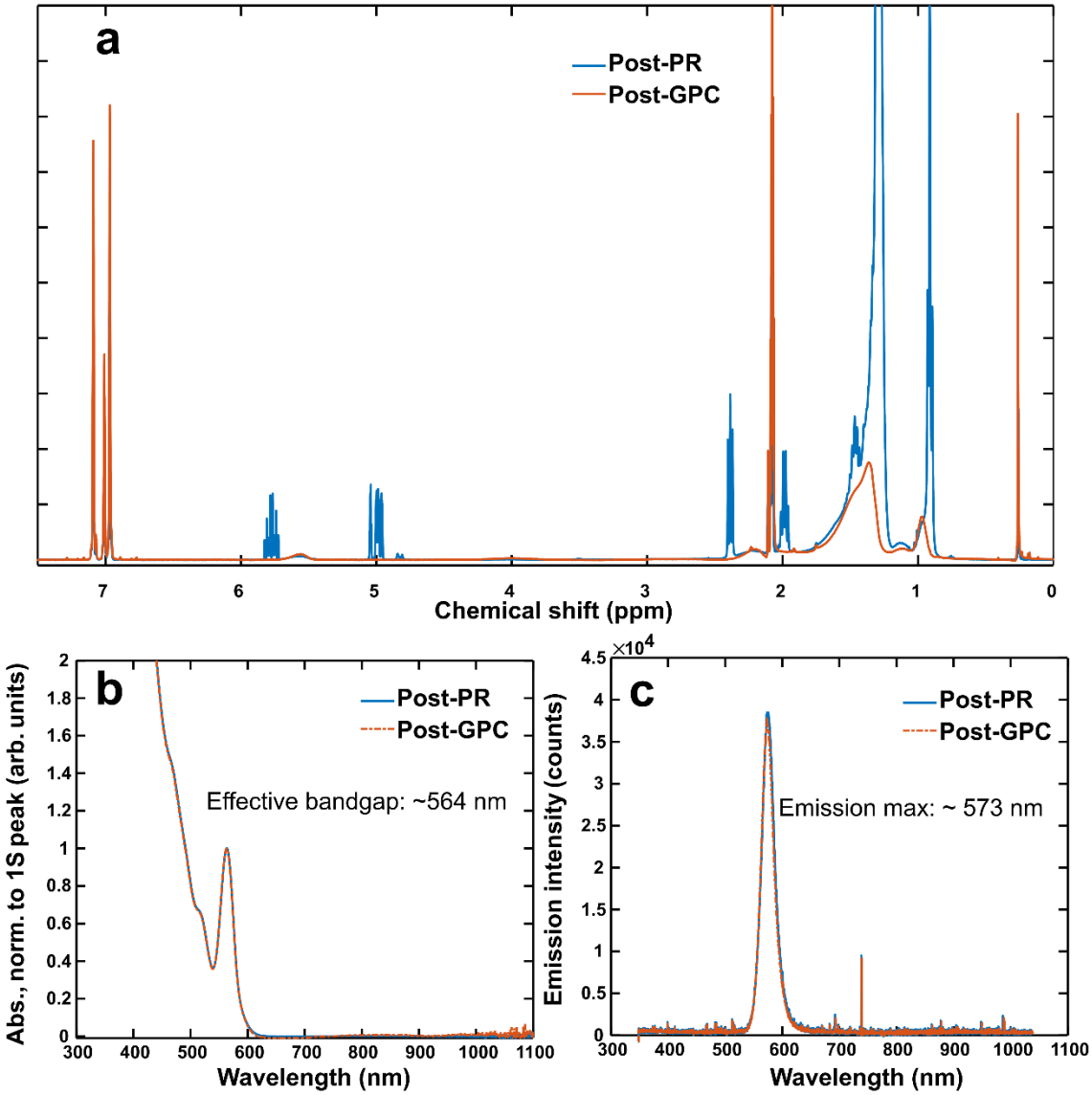

Figure 5.5: CdSe/CdS QD characterization. (a) shows representative proton NMR spectra for oleate-capped CdSe/CdS QDs in toluene-d_8 pre- and post-GPC purification. (b) normalized absorbance spectra for the QDs. (c) photoluminescence spectra for the QDs.

without QD treatment showed no fluorescence signal. These results confirmed the promise of this approach for forming fluorescent surfaces with sub-micron features by hydrophobic self-assembly.

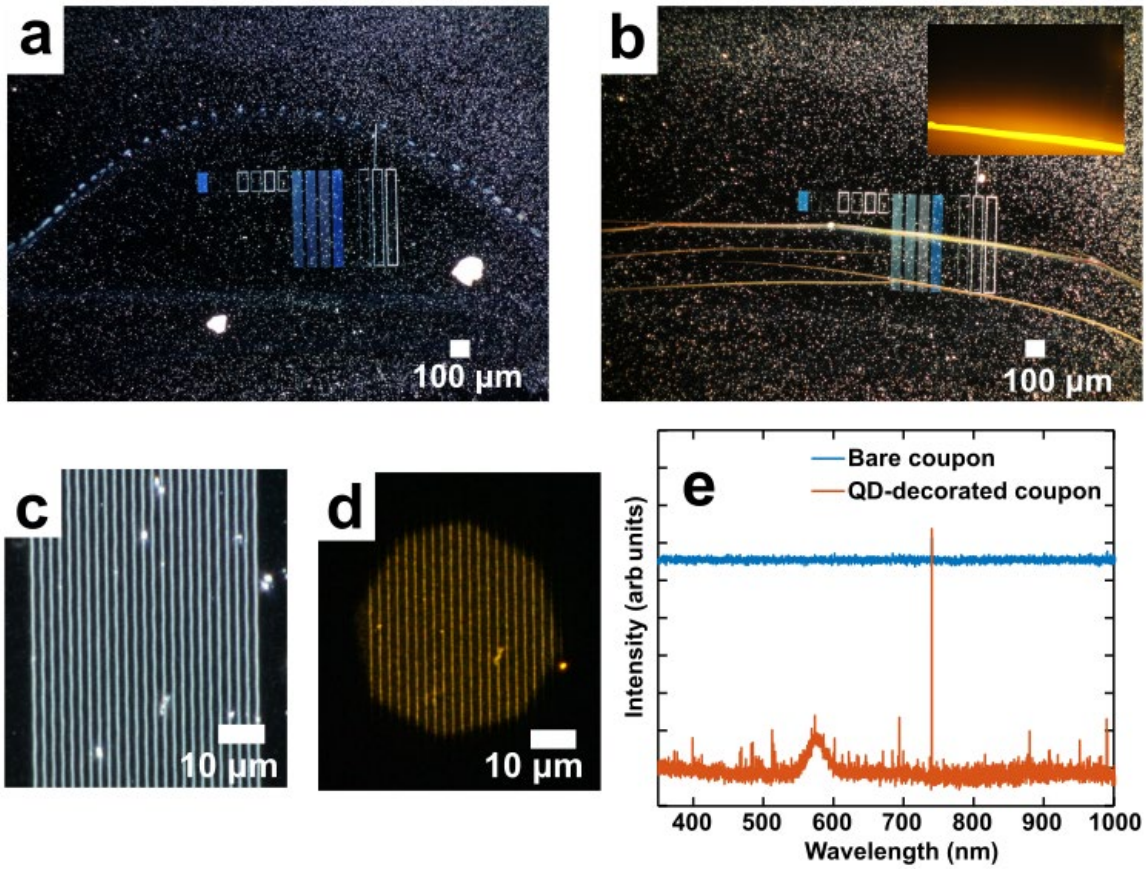

Figure 5.6: Assembly of CdSe/CdS QDs to magnetic nanoparticle templates. (a) dark-field optical microscope image of gratings, pre-QDs. (b) dark field optical microscope image of the same gratings, post-QDs. Inset: fluorescence microscopy image of coffee-ring QD region. (c) zoomed dark-field optical microscope image of a grating with sub-micron spacing, post QDs. (d) fluorescence microscopy image of the same grating in (c). (e) fluorescence spectra for (a) and (d).

5.3: CONCLUSION AND NEXT STAGES

In the prototype experiments described here, we have discovered that QDs terminated with hydrophobic ligands assemble and form fluorescent arrays with sub-micron features. Future work will prioritize more detailed examination of gratings with

spacing d = 700 nm, which was chosen specifically due to the projected feasibility in isolating diffraction of the m = 1 mode (**Figure 5.7**) from fluorescence and diffraction of 473 nm incident light that would be used to excite QDs. Transfer of the patterns to an appropriate waveguide may afford the study of holographic phenomena.

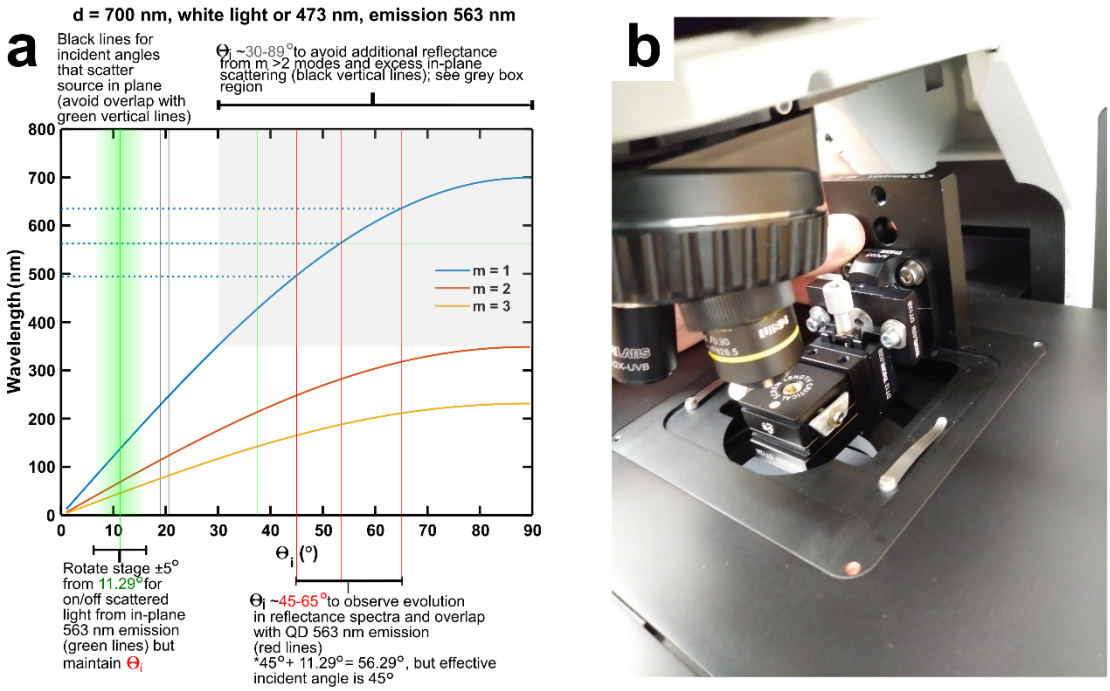

Figure 5.7: Annotated diffraction mode graph and goniometer. (a) Diffraction mode graph. Data pertains to a diffraction grating holding a spacing of d = 700 nm and QDs with emission maximum of 563 nm. (b) shows an image of the home-assembled goniometer stage.

5.4: EXPERIMENTAL

Materials: Cadmium oxide (CdO; 99.999%) and trioctylphosphine oxide (TOPO; 99%) were purchased from STREM Chemicals. Oleic acid (99%), 1-octadecene (ODE; 90% technical grade), 1-tetradecylphosphonic acid (TDPA; 98%), selenium (Se; 99.999%) were purchased from Alfa Aesar. Bio-Beads S-X1 GPC medium were purchased from Bio-Rad Laboratories, Inc. Toluene-d_8 (D, 99.5%) was purchased from

Cambridge Isotope Laboratories, Inc., and bis(trimethylsilyl) sulfide ($(TMS)_2S$; 95%) was purchased from Acros Organics. Oleic acid coated Fe_3O_4 nanoparticles (PrecisionMRX) were purchased from Imagion Biosystems.

Preparation of CdSe QD cores: CdSe QD cores passivated with tetradecylphosphine (TDPA) ligands were synthesized as follows. Prior to preparing the Cd precursor, the selenium precursor was prepared by stirring selenium shot in TOPO at 95 C overnight, generating TOPSe. Then, to a 50 mL 3-neck round bottom flask equipped with a magnetic Teflon stir bar, CdO (60 mg), TDPA (275 mg), TOPO (3 g), and TOP (3 mL) were combined successively and heated at 75 C while stirring under partial vacuum on a Schlenk line until the solid matter melted. The reaction flask was then heated to 350 C and switched to a nitrogen environment en route at 130 C. Formation of the $Cd(TDPA)_2$ was signified by the generation of a clear reaction mixture, and the flask was stirred for 5 minutes before removing the heating mantle and cooling the reaction mixture with an air gun to 170 C. Upon reaching this temperature, the flask was switched back to partial vacuum to drive off water. Next, the flask was cooled by an air gun and evacuated at 170 C for 30 minutes to remove water. The flask was switched to a nitrogen environment and heated to the growth temperature of 360 C before swiftly injecting the Se precursor (2.2 M). The reaction vessel was then cooled to room temperature while stirring. The crude CdSe QD product was stored in the dark under ambient conditions until further use.

CdS shell overcoating to CdSe QD cores: The growth of a cadmium oleate shell to CdSe QDs was conducted following reported methods.[8]

Preparation of Fe_3O_4 nanoparticle assemblies: Magnetic nanoparticle diffraction gratings were prepared following reported methods.[128]

REFERENCES

(1) *Annual Energy Outlook 2021*; Unites States Energy Information Administration, 2021.

(2) Kuno, M. *Introductory Nanoscience*, 1st ed.; Garland Science, 2012.

(3) Hetsch, F.; Zhao, N.; Kershaw, S. V.; Rogach, A. L. Quantum Dot Field Effect Transistors. *Materials Today* **2013**, *16* (9), 312–325. https://doi.org/10.1016/j.mattod.2013.08.011.

(4) Kim, T.; Kelley, M. L.; Kim, D.; Greytak, A. B.; Jeong, S. Purification of Colloidal Nanocrystals Along the Road to Highly Efficient Photovoltaic Devices. *Int. J. of Precis. Eng. and Manuf.-Green Tech.* **2020**. https://doi.org/10.1007/s40684-020-00231-5.

(5) Hassinen, A.; Moreels, I.; De Nolf, K.; Smet, P. F.; Martins, J. C.; Hens, Z. Short-Chain Alcohols Strip X-Type Ligands and Quench the Luminescence of PbSe and CdSe Quantum Dots, Acetonitrile Does Not. *J. Am. Chem. Soc.* **2012**, *134* (51), 20705–20712. https://doi.org/10.1021/ja308861d.

(6) Kelley, M. L. Inorganic Nanocrystals And Their Applications In Hybrid 0D:2D Material Optoelectronics, University of South Carolina - Columbia, Columbia, SC, 2018.

(7) Kelley, M. L.; Letton, J.; Simin, G.; Ahmed, F.; Love-Baker, C. A.; Greytak, A. B.; Chandrashekhar, M. V. S. Photovoltaic and Photoconductive Action Due to PbS Quantum Dots on Graphene/SiC Schottky Diodes from NIR to UV. *ACS Appl. Electron. Mater.* **2020**, *2* (1), 134–139. https://doi.org/10.1021/acsaelm.9b00651.

(8) Shen, Y.; Gee, M. Y.; Tan, R.; Pellechia, P. J.; Greytak, A. B. Purification of Quantum Dots by Gel Permeation Chromatography and the Effect of Excess Ligands on Shell Growth and Ligand Exchange. *Chem. Mater.* **2013**, *25* (14), 2838–2848. https://doi.org/10.1021/cm4012734.

(9) Roberge, A.; Dunlap, J. H.; Ahmed, F.; Greytak, A. B. Size-Dependent PbS Quantum Dot Surface Chemistry Investigated via Gel Permeation Chromatography. *Chem. Mater.* **2020**, *32* (15), 6588–6594. https://doi.org/10.1021/acs.chemmater.0c02024.

(10) Kagan, C. R.; Murray, C. B. Charge Transport in Strongly Coupled Quantum Dot Solids. *Nat Nano* **2015**, *10* (12), 1013–1026. https://doi.org/10.1038/nnano.2015.247.

(11) Konstantatos, G.; Badioli, M.; Gaudreau, L.; Osmond, J.; Bernechea, M.; de Arquer, F. P. G.; Gatti, F.; Koppens, F. H. L. Hybrid Graphene-Quantum Dot Phototransistors with Ultrahigh Gain. *Nat Nano* **2012**, *7* (6), 363–368. https://doi.org/10.1038/nnano.2012.60.

(12) Klem, E. J. D.; Shukla, H.; Hinds, S.; MacNeil, D. D.; Levina, L.; Sargent, E. H. Impact of Dithiol Treatment and Air Annealing on the Conductivity, Mobility, and

Hole Density in PbS Colloidal Quantum Dot Solids. *Appl. Phys. Lett.* **2008**, *92* (21), 212105. https://doi.org/10.1063/1.2917800.
(13) Kelley, M. L.; Letton, J.; Simin, G.; Ahmed, F.; Love-Baker, C. A.; Greytak, A. B.; Chandrashekhar, M. V. S. Photovoltaic and Photoconductive Action Due to PbS Quantum Dots on Graphene/SiC Schottky Diodes from NIR to UV; 2020. https://doi.org/10.1021/scimeetings.0c00011.
(14) Zhang, J.; Crisp, R. W.; Gao, J.; Kroupa, D. M.; Beard, M. C.; Luther, J. M. Synthetic Conditions for High-Accuracy Size Control of PbS Quantum Dots. *J. Phys. Chem. Lett.* **2015**, *6* (10), 1830–1833. https://doi.org/10.1021/acs.jpclett.5b00689.
(15) Moreels, I.; Lambert, K.; Smeets, D.; De Muynck, D.; Nollet, T.; Martins, J. C.; Vanhaecke, F.; Vantomme, A.; Delerue, C.; Allan, G.; Hens, Z. Size-Dependent Optical Properties of Colloidal PbS Quantum Dots. *ACS Nano* **2009**, *3* (10), 3023–3030. https://doi.org/10.1021/nn900863a.
(16) Tvrdy, K.; Kamat, P. Quantum Dot Solar Cells. In *Comprehensive Nanoscience and Technology*; 2010; Vol. 1–5, pp 257–275.
(17) Kamat, P. V. Quantum Dot Solar Cells. Semiconductor Nanocrystals as Light Harvesters. *J. Phys. Chem. C* **2008**, *112* (48), 18737–18753.
(18) King, L. A.; Riley, D. J. Importance of QD Purification Procedure on Surface Adsorbance of QDs and Performance of QD Sensitized Photoanodes. *J. Phys. Chem. C* **2012**, *116* (5), 3349–3355. https://doi.org/10.1021/jp210290j.
(19) Turyanska, L.; Makarovsky, O.; Svatek, S. A.; Beton, P. H.; Mellor, C. J.; Patanè, A.; Eaves, L.; Thomas, N. R.; Fay, M. W.; Marsden, A. J.; Wilson, N. R. Ligand-Induced Control of Photoconductive Gain and Doping in a Hybrid Graphene–Quantum Dot Transistor. *Advanced Electronic Materials* **2015**, *1* (7), 1500062. https://doi.org/10.1002/aelm.201500062.
(20) Campbell, S. A. The Science and Engineering of Microelectronic Fabrication (The Oxford Series in Electrical and Computer Engineering). **2001**.
(21) Brown, P. R.; Kim, D.; Lunt, R. R.; Zhao, N.; Bawendi, M. G.; Grossman, J. C.; Bulović, V. Energy Level Modification in Lead Sulfide Quantum Dot Thin Films through Ligand Exchange. *ACS Nano* **2014**, *8* (6), 5863–5872. https://doi.org/10.1021/nn500897c.
(22) Kroupa, D. M.; Vörös, M.; Brawand, N. P.; McNichols, B. W.; Miller, E. M.; Gu, J.; Nozik, A. J.; Sellinger, A.; Galli, G.; Beard, M. C. Tuning Colloidal Quantum Dot Band Edge Positions through Solution-Phase Surface Chemistry Modification. *Nature Communications* **2017**, *8*, 15257. https://doi.org/10.1038/ncomms15257.
(23) Omar, S. U.; Sudarshan, T. S.; Rana, T. A.; Song, H.; Chandrashekhar, M. V. S. Interface Trap-Induced Nonideality in as-Deposited Ni/4H-SiC Schottky Barrier Diode. *IEEE Transactions on Electron Devices* **2014**, *62* (2), 615–621.
(24) Chava, V. S. N.; Omar, S. U.; Brown, G.; Shetu, S. S.; Andrews, J.; Sudarshan, T. S.; Chandrashekhar, M. V. S. Evidence of Minority Carrier Injection Efficiency >90% in an Epitaxial Graphene/SiC Schottky Emitter Bipolar Junction Phototransistor for Ultraviolet Detection. *Appl. Phys. Lett.* **2016**, *108* (4), 043502. https://doi.org/10.1063/1.4940385.
(25) Chava, V. S. N.; Barker, B. G.; Balachandran, A.; Khan, A.; Simin, G.; Greytak, A. B.; Chandrashekhar, M. V. S. High Detectivity Visible-Blind SiF4 Grown

Epitaxial Graphene/SiC Schottky Contact Bipolar Phototransistor. *Appl. Phys. Lett.* **2017**, *111* (24), 243504. https://doi.org/10.1063/1.5009003.
(26) Barker, B. G.; Chava, V. S. N.; Daniels, K. M.; Chandrashekhar, M. V. S.; Greytak, A. B. Sub-Bandgap Response of Graphene/SiC Schottky Emitter Bipolar Phototransistor Examined by Scanning Photocurrent Microscopy. *2D Mater.* **2018**, *5* (1), 011003. https://doi.org/10.1088/2053-1583/aa90b1.
(27) Sun, Z.; Liu, Z.; Li, J.; Tai, G.; Lau, S.-P.; Yan, F. Infrared Photodetectors Based on CVD-Grown Graphene and PbS Quantum Dots with Ultrahigh Responsivity. *Adv. Mater.* **2012**, *24* (43), 5878–5883. https://doi.org/10.1002/adma.201202220.
(28) Robin, A.; Lhuillier, E.; Xu, X. Z.; Ithurria, S.; Aubin, H.; Ouerghi, A.; Dubertret, B. Engineering the Charge Transfer in All 2D Graphene-Nanoplatelets Heterostructure Photodetectors. *Scientific Reports* **2016**, *6*, 24909. https://doi.org/10.1038/srep24909.
(29) Makarovsky, O.; Turyanska, L.; Mori, N.; Greenaway, M.; Eaves, L.; Patané, A.; Mark Fromhold; Lara-Avila, S.; Kubatkin, S.; Yakimova, R. Enhancing Optoelectronic Properties of SiC-Grown Graphene by a Surface Layer of Colloidal Quantum Dots. *2D Mater.* **2017**, *4* (3), 031001. https://doi.org/10.1088/2053-1583/aa76bb.
(30) Yu, T.; Wang, F.; Xu, Y.; Ma, L.; Pi, X.; Yang, D. Graphene Coupled with Silicon Quantum Dots for High-Performance Bulk-Silicon-Based Schottky-Junction Photodetectors. *Advanced Materials* **2016**, *28* (24), 4912–4919. https://doi.org/10.1002/adma.201506140.
(31) Jahangir, I.; Uddin, M. A.; Singh, A. K.; Koley, G.; Chandrashekhar, M. V. S. Richardson Constant and Electrostatics in Transfer-Free CVD Grown Few-Layer MoS2/Graphene Barristor with Schottky Barrier Modulation >0.6eV. *Appl. Phys. Lett.* **2017**, *111* (14), 142101. https://doi.org/10.1063/1.5005796.
(32) Graetzel, M.; Janssen, R. A. J.; Mitzi, D. B.; Sargent, E. H. Materials Interface Engineering for Solution-Processed Photovoltaics. 2012.
(33) Rana, T.; Chandrashekhar, M. V. S.; Daniels, K.; Sudarshan, T. Epitaxial Growth of Graphene on SiC by Si Selective Etching Using SiF4 in an Inert Ambient. *Jpn. J. Appl. Phys.* **2015**, *54* (3), 030304. https://doi.org/10.7567/JJAP.54.030304.
(34) Shen, Y.; Roberge, A.; Tan, R.; Gee, M. Y.; Gary, D. C.; Huang, Y.; Blom, D. A.; Benicewicz, B. C.; Cossairt, B. M.; Greytak, A. B. Gel Permeation Chromatography as a Multifunctional Processor for Nanocrystal Purification and On-Column Ligand Exchange Chemistry. *Chem. Sci.* **2016**, *7* (9), 5671–5679. https://doi.org/10.1039/C6SC01301E.
(35) Roberge, A.; Stein, J. L.; Shen, Y.; Cossairt, B. M.; Greytak, A. B. Purification and In Situ Ligand Exchange of Metal-Carboxylate-Treated Fluorescent InP Quantum Dots via Gel Permeation Chromatography. *J. Phys. Chem. Lett.* **2017**, *8* (17), 4055–4060. https://doi.org/10.1021/acs.jpclett.7b01772.
(36) Balachandran, A. High Quality Low Offcut 4h-Sic Epitaxy and Integrated Growth of Epitaxial Graphene for Hybrid Graphene/Sic Devices. Doctoral dissertation, University of South Carolina, Columbia, SC, 2017.
(37) Balachandran, A.; Song, H. Z.; Sudarshan, T. S.; Shetu, S. S.; Chandrashekhar, M. V. S. Study of SiC Epitaxial Growth Using Tetrafluorosilane and Dichlorosilane in Vertical Hotwall CVD Furnace https://www.scientific.net/MSF.821-823.137

(accessed 2018 -06 -07). https://doi.org/10.4028/www.scientific.net/MSF.821-823.137.
(38) Rana, T.; Chandrashekhar, M. V. S.; Daniels, K.; Sudarshan, T. SiC Homoepitaxy, Etching and Graphene Epitaxial Growth on SiC Substrates Using a Novel Fluorinated Si Precursor Gas (SiF4). *Journal of Elec Materi* **2016**, *45* (4), 2019–2024. https://doi.org/10.1007/s11664-015-4234-2.
(39) Shetu, S. S.; Omar, S. U.; Daniels, K. M.; Daas, B.; Andrews, J.; Ma, S.; Sudarshan, T. S.; Chandrashekhar, M. V. S. Si-Adatom Kinetics in Defect Mediated Growth of Multilayer Epitaxial Graphene Films on 6H-SiC. *Journal of Applied Physics* **2013**, *114* (16), 1–10. https://doi.org/10.1063/1.4826899.
(40) Balachandran, A.; Song, H.; Sudarshan, T. S.; Chandrashekhar, M. V. S. 4H–SiC Homoepitaxy on Nearly on-Axis Substrates Using TFS-towards High Quality Epitaxial Growth. *Journal of Crystal Growth* **2016**, *448*, 97–104. https://doi.org/10.1016/j.jcrysgro.2016.05.018.
(41) Klem, E. J. D.; MacNeil, D. D.; Cyr, P. W.; Levina, L.; Sargent, E. H. Efficient Solution-Processed Infrared Photovoltaic Cells: Planarized All-Inorganic Bulk Heterojunction Devices via Inter-Quantum-Dot Bridging during Growth from Solution. *Applied Physics Letters* **2007**, *90* (18), 10–13. https://doi.org/10.1063/1.2735674.
(42) Bessonov, A. A.; Allen, M.; Liu, Y.; Malik, S.; Bottomley, J.; Rushton, A.; Medina-Salazar, I.; Voutilainen, M.; Kallioinen, S.; Colli, A.; Bower, C.; Andrew, P.; Ryhänen, T. Compound Quantum Dot–Perovskite Optical Absorbers on Graphene Enhancing Short-Wave Infrared Photodetection. *ACS Nano* **2017**, *11* (6), 5547–5557. https://doi.org/10.1021/acsnano.7b00760.
(43) Zaman, M. Y.; Perrone, D.; Ferrero, S.; Scaltrito, L.; Naretto, M. Evaluation of Correct Value of Richardson's Constant by Analyzing the Electrical Behavior of Three Different Diodes at Different Temperatures. *Materials Science Forum* **2012**. https://doi.org/10.4028/www.scientific.net/MSF.711.174.
(44) Konstantatos, G.; Sargent, E. H. PbS Colloidal Quantum Dot Photoconductive Photodetectors: Transport, Traps, and Gain. *Applied Physics Letters* **2007**, *91* (17), 1–4. https://doi.org/10.1063/1.2800805.
(45) Wiets, M.; Weinelt, M.; Fauster, T. Electronic Structure of SiC(0001) Surfaces Studied by Two-Photon Photoemission. *Phys. Rev. B* **2003**, *68* (12), 125321. https://doi.org/10.1103/PhysRevB.68.125321.
(46) Sze, S. M.; Ng, K. K. *Physics of Semiconductor Devices*; John wiley & sons, 2006.
(47) Hooge, F. N. 1/f Noise Sources. *IEEE Transactions on Electron Devices* **1994**, *41* (11), 1926–1935. https://doi.org/10.1109/16.333808.
(48) Balandin, A. A. Low-Frequency 1/f Noise in Graphene Devices. *Nat Nano* **2013**, *8* (8), 549–555. https://doi.org/10.1038/nnano.2013.144.
(49) Al-Zeben, M. Y.; Saleh, A. H. M.; Al-Omar, M. A. TLM Modelling of Diffusion, Drift and Recombination of Charge Carriers in Semiconductors. *International Journal of Numerical Modelling: Electronic Networks, Devices and Fields* **1992**, *5* (4), 219–225. https://doi.org/10.1002/jnm.1660050403.
(50) Shatalov, M.; Simin, G.; Adivarahan, V.; Chitnis, A.; Wu, S.; Pachipulusu, R.; Mandavilli, V.; Simin, K.; Zhang, J. P.; Yang, J. W.; Khan, M. A. Lateral Current

Crowding in Deep UV Light Emitting Diodes over Sapphire Substrates. *Jpn. J. Appl. Phys.* **2002**, *41* (8R), 5083. https://doi.org/10.1143/JJAP.41.5083.
(51) Ahmed, F.; Kelley, M. L.; Chandrashekhar, M. V. S.; Greytak, A. B. Improved Charge Transport in PbS Quantum Dot Thin Films Following Gel Permeation Chromatography Purification. *(under review)*.
(52) Henry, C. H. Limiting Efficiencies of Ideal Single and Multiple Energy Gap Terrestrial Solar Cells. *Journal of Applied Physics* **1980**, *51* (8), 4494–4500. https://doi.org/10.1063/1.328272.
(53) Green, M. A. Limiting Efficiency of Bulk and Thin-film Silicon Solar Cells in the Presence of Surface Recombination. *Progress in Photovoltaics: Research and Applications* **1999**, *7* (4), 327–330.
(54) Aldalbahi, A.; Li, E.; Rivera, M.; Velazquez, R.; Altalhi, T.; Peng, X.; Feng, P. X. A New Approach for Fabrications of SiC Based Photodetectors. *Sci Rep* **2016**, *6* (1), 1–10. https://doi.org/10.1038/srep23457.
(55) El Fatimy, A.; Nath, A.; Kong, B. D.; Boyd, A. K.; Myers-Ward, R. L.; Daniels, K. M.; Jadidi, M. M.; Murphy, T. E.; Gaskill, D. K.; Barbara, P. Ultra-Broadband Photodetectors Based on Epitaxial Graphene Quantum Dots. *Nanophotonics* **2018**, *7* (4), 735–740. https://doi.org/10.1515/nanoph-2017-0100.
(56) Kelley, M. L.; Simin, G.; Hussain, K.; Khan, A.; Greytak, A. B.; Chandrashekhar, M. V. S. Spatially Resolved Fourier Transform Impedance Spectroscopy: A Technique to Rapidly Characterize Interfaces, Applied to a QD/SiC Heterojunction. *Appl. Phys. Lett.* **2021**, *118* (22), 223102. https://doi.org/10.1063/5.0046439.
(57) Xiao, R.; Hou, Y.; Fu, Y.; Peng, X.; Wang, Q.; Gonzalez, E.; Jin, S.; Yu, D. Photocurrent Mapping in Single-Crystal Methylammonium Lead Iodide Perovskite Nanostructures. *Nano Lett.* **2016**, *16* (12), 7710–7717. https://doi.org/10.1021/acs.nanolett.6b03782.
(58) Rekemeyer, P. H.; Chuang, C.-H. M.; Bawendi, M. G.; Gradečak, S. Minority Carrier Transport in Lead Sulfide Quantum Dot Photovoltaics. *Nano Lett.* **2017**, *17* (10), 6221–6227. https://doi.org/10.1021/acs.nanolett.7b02916.
(59) Ecker, B.; Nolasco, J. C.; Pallarés, J.; Marsal, L. F.; Posdorfer, J.; Parisi, J.; Hauff, E. von. Degradation Effects Related to the Hole Transport Layer in Organic Solar Cells. *Advanced Functional Materials* **2011**, *21* (14), 2705–2711. https://doi.org/10.1002/adfm.201100429.
(60) Zolfaghari, Z.; Hassanabadi, E.; Pitarch-Tena, D.; Yoon, S. J.; Shariatinia, Z.; van de Lagemaat, J.; Luther, J. M.; Mora-Seró, I. Operation Mechanism of Perovskite Quantum Dot Solar Cells Probed by Impedance Spectroscopy. *ACS Energy Lett.* **2019**, *4* (1), 251–258. https://doi.org/10.1021/acsenergylett.8b02157.
(61) Rath, A. K.; Lasanta, T.; Bernechea, M.; Diedenhofen, S. L.; Konstantatos, G. Determination of Carrier Lifetime and Mobility in Colloidal Quantum Dot Films via Impedance Spectroscopy. *Appl. Phys. Lett.* **2014**, *104* (6), 063504. https://doi.org/10.1063/1.4865089.
(62) Tavakoli, M. M.; Simchi, A.; Tavakoli, R.; Fan, Z. Organic Halides and Nanocone Plastic Structures Enhance the Energy Conversion Efficiency and Self-Cleaning

Ability of Colloidal Quantum Dot Photovoltaic Devices. *J. Phys. Chem. C* **2017**, *121* (18), 9757–9765. https://doi.org/10.1021/acs.jpcc.7b02394.
(63) Fukuda, T.; Takahashi, A.; Wang, H.; Takahira, K.; Kubo, T.; Segawa, H. Impedance Analysis of PbS Colloidal Quantum Dot Solar Cells with Different ZnO Nanowire Lengths. *Jpn. J. Appl. Phys.* **2017**, *57* (3S2), 03EJ02. https://doi.org/10.7567/JJAP.57.03EJ02.
(64) Tessler, N. Experimental Techniques and the Underlying Device Physics. *Journal of Polymer Science Part B: Polymer Physics* **2014**, *52* (17), 1119–1152. https://doi.org/10.1002/polb.23550.
(65) Bozyigit, D.; Wood, V. Electrical Characterization of Nanocrystal Solids. *J. Mater. Chem. C* **2014**, *2* (17), 3172–3184. https://doi.org/10.1039/C3TC32235A.
(66) Konstantatos, G.; Clifford, J.; Levina, L.; Sargent, E. H. Sensitive Solution-Processed Visible-Wavelength Photodetectors. *Nat Photon* **2007**, *1* (9), 531–534. https://doi.org/10.1038/nphoton.2007.147.
(67) Krause, S.; Talabani, H.; Xu, M.; Moritz, W.; Griffiths, J. Scanning Photo-Induced Impedance Microscopy—an Impedance Based Imaging Technique. *Electrochimica Acta* **2002**, *47* (13), 2143–2148. https://doi.org/10.1016/S0013-4686(02)00088-9.
(68) Gao, Y.; Wise, A. J.; Thomas, A. K.; Grey, J. K. Spectroscopic and Intensity Modulated Photocurrent Imaging of Polymer/Fullerene Solar Cells. **2015**. https://doi.org/10.1021/acsami.5b08724.
(69) Bozyigit, D.; Volk, S.; Yarema, O.; Wood, V. Quantification of Deep Traps in Nanocrystal Solids, Their Electronic Properties, and Their Influence on Device Behavior. *Nano Lett.* **2013**, *13* (11), 5284–5288. https://doi.org/10.1021/nl402803h.
(70) Bozyigit, D.; Jakob, M.; Yarema, O.; Wood, V. Deep Level Transient Spectroscopy (DLTS) on Colloidal-Synthesized Nanocrystal Solids. *ACS Appl. Mater. Interfaces* **2013**, *5* (8), 2915–2919. https://doi.org/10.1021/am400326t.
(71) Ulaby, F.; Maharbiz, M.; Furse, C. *Circuit Analysis and Design*; Michigan Publishing, 2018.
(72) von Hauff, E. Impedance Spectroscopy for Emerging Photovoltaics. *J. Phys. Chem. C* **2019**, *123* (18), 11329–11346. https://doi.org/10.1021/acs.jpcc.9b00892.
(73) Nikitskiy, I.; Goossens, S.; Kufer, D.; Lasanta, T.; Navickaite, G.; Koppens, F. H. L.; Konstantatos, G. Integrating an Electrically Active Colloidal Quantum Dot Photodiode with a Graphene Phototransistor. *Nature Communications* **2016**, *7*, 11954. https://doi.org/10.1038/ncomms11954.
(74) Guerrero-Pérez, M. O.; Patience, G. S. Experimental Methods in Chemical Engineering: Fourier Transform Infrared Spectroscopy—FTIR. *The Canadian Journal of Chemical Engineering* **2020**, *98* (1), 25–33. https://doi.org/10.1002/cjce.23664.
(75) Dzsaber, S.; Negyedi, M.; Bernáth, B.; Gyüre, B.; Fehér, T.; Kramberger, C.; Pichler, T.; Simon, F. A Fourier Transform Raman Spectrometer with Visible Laser Excitation. *Journal of Raman Spectroscopy* **2015**, *46* (3), 327–332. https://doi.org/10.1002/jrs.4641.
(76) Yoo, J.-S.; Park, S.-M. An Electrochemical Impedance Measurement Technique Employing Fourier Transform. *Anal. Chem.* **2000**, *72* (9), 2035–2041. https://doi.org/10.1021/ac9907540.

(77) Yang, J.; Guo, L.; Guo, Y.; Hu, W.; Zhang, Z. Epitaxial Graphene/SiC Schottky Ultraviolet Photodiode with Orders of Magnitude Adjustability in Responsivity and Response Speed. *Appl. Phys. Lett.* **2018**, *112* (10), 103501. https://doi.org/10.1063/1.5019435.
(78) Rauch, T.; Böberl, M.; Tedde, S. F.; Fürst, J.; Kovalenko, M. V.; Hesser, G.; Lemmer, U.; Heiss, W.; Hayden, O. Near-Infrared Imaging with Quantum-Dot-Sensitized Organic Photodiodes. *Nature Photonics* **2009**, *3* (6), 332–336. https://doi.org/10.1038/nphoton.2009.72.
(79) Graham, R.; Yu, D. SPCM in Semiconductor Nanostructures. *Modern Physics Letters B* **2013**, *27* (25).
(80) Steer, M. *Microwave and RF Design: A Systems Approach*, 1st ed.; SciTech Publishing, Inc.: Raleigh, NC, 2010.
(81) Kirmani, A. R.; Walters, G.; Kim, T.; Sargent, E. H.; Amassian, A. Optimizing Solid-State Ligand Exchange for Colloidal Quantum Dot Optoelectronics: How Much Is Enough? *ACS Appl. Energy Mater.* **2020**, *3* (6), 5385–5392. https://doi.org/10.1021/acsaem.0c00389.
(82) Kausch, H. H.; Fesko, D. G.; Tschoegl, N. W. The Random Packing of Circles in a Plane. *Journal of Colloid and Interface Science* **1971**, *37* (3), 603–611. https://doi.org/10.1016/0021-9797(71)90338-9.
(83) Wood, S.; O'Connor, D.; Jones, C. W.; Claverley, J. D.; Blakesley, J. C.; Giusca, C.; Castro, F. A. Transient Photocurrent and Photovoltage Mapping for Characterisation of Defects in Organic Photovoltaics. *Solar Energy Materials and Solar Cells* **2017**, *161*, 89–95. https://doi.org/10.1016/j.solmat.2016.11.029.
(84) Nguyen, H. T.; Ryu, S. Y.; Duong, A. T.; Lee, S. Effects of 1,2-Ethanedithiol Concentration on Performance Improvement of Quantum-Dot LEDs. *RSC Adv.* **2019**, *9* (66), 38464–38468. https://doi.org/10.1039/c9ra08411h.
(85) Masala, S.; Adinolfi, V.; Sun, J.-P.; Gobbo, S. D.; Voznyy, O.; Kramer, I. J.; Hill, I. G.; Sargent, E. H. The Silicon:Colloidal Quantum Dot Heterojunction. *Adv. Mater.* **2015**, *27* (45), 7445–7450. https://doi.org/10.1002/adma.201503212.
(86) Adinolfi, V.; Sargent, E. H. Photovoltage Field-Effect Transistors. *Nature* **2017**, *542* (7641), 324–327. https://doi.org/10.1038/nature21050.
(87) Yang, J.; Hahm, D.; Kim, K.; Rhee, S.; Lee, M.; Kim, S.; Chang, J. H.; Park, H. W.; Lim, J.; Lee, M.; Kim, H.; Bang, J.; Ahn, H.; Cho, J. H.; Kwak, J.; Kim, B.; Lee, C.; Bae, W. K.; Kang, M. S. High-Resolution Patterning of Colloidal Quantum Dots via Non-Destructive, Light-Driven Ligand Crosslinking. *Nat. Commun.* **2020**, *11* (1). https://doi.org/10.1038/s41467-020-16652-4.
(88) Dieleman, C. D.; Ding, W.; Wu, L.; Thakur, N.; Bespalov, I.; Daiber, B.; Ekinci, Y.; Castellanos, S.; Ehrler, B. Universal Direct Patterning of Colloidal Quantum Dots by (Extreme) Ultraviolet and Electron Beam Lithography. *Nanoscale* **2020**, *12* (20), 11306–11316. https://doi.org/10.1039/d0nr01077d.
(89) Zhou, W.; Zheng, L.; Cheng, X.; Zhou, W.; Xiao, X.; Xu, K.; Xin, W.; Ye, P.; Yu, Y. PbS Colloidal Quantum Dots Patterning Technique with Low Vertical Leakage Current for the Photodetection Applications. *J. Mater. Sci.-Mater. Electron.* **2020**, *31* (8), 5900–5906. https://doi.org/10.1007/s10854-019-02819-3.
(90) Chen, J.; Wu, Y.; Li, X.; Cao, F.; Gu, Y.; Liu, K.; Liu, X.; Dong, Y.; Ji, J.; Zeng, H. Simple and Fast Patterning Process by Laser Direct Writing for Perovskite

Quantum Dots. *Advanced Materials Technologies* **2017**, *2* (10), 1700132. https://doi.org/10.1002/admt.201700132.
(91) Sliz, R.; Lejay, M.; Fan, J. Z.; Choi, M.-J.; Kinge, S.; Hoogland, S.; Fabritius, T.; de Arguer, F. P. G.; Sargent, E. H. Stable Colloidal Quantum Dot Inks Enable Inkjet-Printed High-Sensitivity Infrared Photodetectors. *ACS Nano* **2019**, *13* (10), 11988–11995. https://doi.org/10.1021/acsnano.9b06125.
(92) Sze, S. M. *Physics of Semiconductor Devices*, 2nd ed.; Wiley, 1988.
(93) Kelley, M. L.; Ahmed, F.; Abiodun, S. L.; Usman, M.; Jewel, M. U.; Hussain, K.; zur Loye, H.-C.; Chandrashekhar, M. V. S.; Greytak, A. B. Photoconductive Thin Films Composed of Environmentally Benign AgBiS2 Nanocrystal Inks Obtained through a Rapid Phase Transfer Process. *ACS Appl. Electron. Mater.* **2021**, *3* (4), 1550–1555. https://doi.org/10.1021/acsaelm.0c01107.
(94) Talapin, D. V.; Lee, J.-S.; Kovalenko, M. V.; Shevchenko, E. V. Prospects of Colloidal Nanocrystals for Electronic and Optoelectronic Applications. *Chem. Rev.* **2010**, *110* (1), 389–458. https://doi.org/10.1021/cr900137k.
(95) Öberg, V. A.; Johansson, M. B.; Zhang, X.; Johansson, E. M. J. Cubic AgBiS2 Colloidal Nanocrystals for Solar Cells. *ACS Appl. Nano Mater.* **2020**, *3* (5), 4014–4024. https://doi.org/10.1021/acsanm.9b02443.
(96) Bernechea, M.; Miller, N. C.; Xercavins, G.; So, D.; Stavrinadis, A.; Konstantatos, G. Solution-Processed Solar Cells Based on Environmentally Friendly $AgBiS_2$ Nanocrystals. *Nature Photonics* **2016**, *10* (8), 521–525. https://doi.org/10.1038/nphoton.2016.108.
(97) Chen, C.; Qiu, X.; Ji, S.; Jia, C.; Ye, C. The Synthesis of Monodispersed AgBiS2 Quantum Dots with a Giant Dielectric Constant. *CrystEngComm* **2013**, *15* (38), 7644–7648. https://doi.org/10.1039/C3CE41304G.
(98) Mak, C. H.; Qian, J.; Rogée, L.; Lai, W. K.; Lau, S. P. Facile Synthesis of AgBiS2 Nanocrystals for High Responsivity Infrared Detectors. *RSC Adv.* **2018**, *8* (68), 39203–39207. https://doi.org/10.1039/C8RA08509A.
(99) Kirmani, A. R. Commercializing Colloidal Quantum Dot Photovoltaics. *MRS Bulletin* **2019**, *44* (7), 524–525. https://doi.org/10.1557/mrs.2019.163.
(100) Fafarman, A. T.; Koh, W.; Diroll, B. T.; Kim, D. K.; Ko, D.-K.; Oh, S. J.; Ye, X.; Doan-Nguyen, V.; Crump, M. R.; Reifsnyder, D. C.; Murray, C. B.; Kagan, C. R. Thiocyanate-Capped Nanocrystal Colloids: Vibrational Reporter of Surface Chemistry and Solution-Based Route to Enhanced Coupling in Nanocrystal Solids. *J. Am. Chem. Soc.* **2011**, *133* (39), 15753–15761. https://doi.org/10.1021/ja206303g.
(101) Sayevich, V.; Gaponik, N.; Plötner, M.; Kruszynska, M.; Gemming, T.; Dzhagan, V. M.; Akhavan, S.; Zahn, D. R. T.; Demir, H. V.; Eychmüller, A. Stable Dispersion of Iodide-Capped PbSe Quantum Dots for High-Performance Low-Temperature Processed Electronics and Optoelectronics. *Chem. Mater.* **2015**, *27* (12), 4328–4337. https://doi.org/10.1021/acs.chemmater.5b00793.
(102) Nag, A.; Kovalenko, M. V.; Lee, J.-S.; Liu, W.; Spokoyny, B.; Talapin, D. V. Metal-Free Inorganic Ligands for Colloidal Nanocrystals: S2–, HS–, Se2–, HSe–, Te2–, HTe–, TeS32–, OH–, and NH2– as Surface Ligands. *J. Am. Chem. Soc.* **2011**, *133* (27), 10612–10620. https://doi.org/10.1021/ja2029415.

(103) Zhang, H.; Jang, J.; Liu, W.; Talapin, D. V. Colloidal Nanocrystals with Inorganic Halide, Pseudohalide, and Halometallate Ligands. *ACS Nano* **2014**, *8* (7), 7359–7369. https://doi.org/10.1021/nn502470v.
(104) Lee, S.; Choi, M.-J.; Sharma, G.; Biondi, M.; Chen, B.; Baek, S.-W.; Najarian, A. M.; Vafaie, M.; Wicks, J.; Sagar, L. K.; Hoogland, S.; de Arquer, F. P. G.; Voznyy, O.; Sargent, E. H. Orthogonal Colloidal Quantum Dot Inks Enable Efficient Multilayer Optoelectronic Devices. *Nat. Commun.* **2020**, *11* (1), 4814. https://doi.org/10.1038/s41467-020-18655-7.
(105) Giansante, C.; Carbone, L.; Giannini, C.; Altamura, D.; Ameer, Z.; Maruccio, G.; Loiudice, A.; Belviso, M. R.; Cozzoli, P. D.; Rizzo, A.; Gigli, G. Colloidal Arenethiolate-Capped PbS Quantum Dots: Optoelectronic Properties, Self-Assembly, and Application in Solution-Cast Photovoltaics. *J. Phys. Chem. C* **2013**, *117* (25), 13305–13317. https://doi.org/10.1021/jp403066q.
(106) Song, J. H.; Choi, H.; Pham, H. T.; Jeong, S. Energy Level Tuned Indium Arsenide Colloidal Quantum Dot Films for Efficient Photovoltaics. *Nature Communications* **2018**, *9* (1), 4267. https://doi.org/10.1038/s41467-018-06399-4.
(107) Choi, M.-J.; García de Arquer, F. P.; Proppe, A. H.; Seifitokaldani, A.; Choi, J.; Kim, J.; Baek, S.-W.; Liu, M.; Sun, B.; Biondi, M.; Scheffel, B.; Walters, G.; Nam, D.-H.; Jo, J. W.; Ouellette, O.; Voznyy, O.; Hoogland, S.; Kelley, S. O.; Jung, Y. S.; Sargent, E. H. Cascade Surface Modification of Colloidal Quantum Dot Inks Enables Efficient Bulk Homojunction Photovoltaics. *Nature Communications* **2020**, *11* (1), 103. https://doi.org/10.1038/s41467-019-13437-2.
(108) Lin, Q.; Yun, H. J.; Liu, W.; Song, H.-J.; Makarov, N. S.; Isaienko, O.; Nakotte, T.; Chen, G.; Luo, H.; Klimov, V. I.; Pietryga, J. M. Phase-Transfer Ligand Exchange of Lead Chalcogenide Quantum Dots for Direct Deposition of Thick, Highly Conductive Films. *J. Am. Chem. Soc.* **2017**, *139* (19), 6644–6653. https://doi.org/10.1021/jacs.7b01327.
(109) Liu, M.; Voznyy, O.; Sabatini, R.; García de Arquer, F. P.; Munir, R.; Balawi, A. H.; Lan, X.; Fan, F.; Walters, G.; Kirmani, A. R.; Hoogland, S.; Laquai, F.; Amassian, A.; Sargent, E. H. Hybrid Organic-Inorganic Inks Flatten the Energy Landscape in Colloidal Quantum Dot Solids. *Nat Mater* **2017**, *16* (2), 258–263. https://doi.org/10.1038/nmat4800.
(110) Choi, H.; Kim, S.; Luther, J. M.; Kim, S.-W.; Shin, D.; Beard, M. C.; Jeong, S. Facet-Specific Ligand Interactions on Ternary AgSbS2 Colloidal Quantum Dots. *Chemistry – A European Journal* **2017**, *23* (70), 17707–17713. https://doi.org/10.1002/chem.201703681.
(111) Reinhold, H.; Mikolajczak, U.; Brand, I.; Dosche, C.; Borchert, H.; Parisi, J.; Scheunemann, D. Shorter Is Not Always Better: Analysis of a Ligand Exchange Procedure for CuInS2 Nanoparticles as the Photovoltaic Absorber Material. *J. Phys. Chem. C* **2020**, *124* (37), 19922–19928. https://doi.org/10.1021/acs.jpcc.0c04489.
(112) Bae, S. Y.; Oh, J. T.; Park, J. Y.; Ha, S. R.; Choi, J.; Choi, H.; Kim, Y. Improved Eco-Friendly Photovoltaics Based on Stabilized AgBiS2 Nanocrystal Inks. *Chem. Mater.* **2020**. https://doi.org/10.1021/acs.chemmater.0c03126.
(113) Jo, J. W.; Choi, J.; García de Arquer, F. P.; Seifitokaldani, A.; Sun, B.; Kim, Y.; Ahn, H.; Fan, J.; Quintero-Bermudez, R.; Kim, J.; Choi, M.-J.; Baek, S.-W.;

Proppe, A. H.; Walters, G.; Nam, D.-H.; Kelley, S.; Hoogland, S.; Voznyy, O.; Sargent, E. H. Acid-Assisted Ligand Exchange Enhances Coupling in Colloidal Quantum Dot Solids. *Nano Lett.* **2018**, *18* (7), 4417–4423. https://doi.org/10.1021/acs.nanolett.8b01470.

(114) Ming, S.; Liu, X.; Zhang, W.; Xie, Q.; Wu, Y.; Chen, L.; Wang, H.-Q. Eco-Friendly and Stable Silver Bismuth Disulphide Quantum Dot Solar Cells via Methyl Acetate Purification and Modified Ligand Exchange. *J. Clean Prod.* **2020**, *246*, 118966. https://doi.org/10.1016/j.jclepro.2019.118966.

(115) van Embden, J.; Della Gaspera, E. Ultrathin Solar Absorber Layers of Silver Bismuth Sulfide from Molecular Precursors. *ACS Appl. Mater. Interfaces* **2019**, *11* (18), 16674–16682. https://doi.org/10.1021/acsami.8b22414.

(116) Geller, S.; Wernick, J. H. Ternary Semiconducting Compounds with Sodium Chloride-like Structure: AgSbSe2, AgSbTe2, AgBiS2, AgBiSe2. *Acta Crystallographica* **1959**, *12* (1), 46–54. https://doi.org/10.1107/S0365110X59000135.

(117) Jia, D.; Chen, J.; Zheng, S.; Phuyal, D.; Yu, M.; Tian, L.; Liu, J.; Karis, O.; Rensmo, H.; Johansson, E. M. J.; Zhang, X. Highly Stabilized Quantum Dot Ink for Efficient Infrared Light Absorbing Solar Cells. *Adv. Energy Mater.* 1902809. https://doi.org/10.1002/aenm.201902809.

(118) Medina-Gonzalez, A. M.; Rosales, B. A.; Hamdeh, U. H.; Panthani, M. G.; Vela, J. Surface Chemistry of Ternary Nanocrystals: Engineering the Deposition of Conductive NaBiS2 Films. *Chem. Mater.* **2020**. https://doi.org/10.1021/acs.chemmater.0c01689.

(119) Gu, E.; Lin, X.; Tang, X.; Matt, G. J.; Osvet, A.; Hou, Y.; Jäger, S.; Xie, C.; Karl, A.; Hock, R.; Brabec, C. J. Single Molecular Precursor Ink for AgBiS2 Thin Films: Synthesis and Characterization. *J. Mater. Chem. C* **2018**, *6* (28), 7642–7651. https://doi.org/10.1039/C8TC01195H.

(120) Strasfeld, D. B.; Dorn, A.; Wanger, D. D.; Bawendi, M. G. Imaging Schottky Barriers and Ohmic Contacts in PbS Quantum Dot Devices. *Nano Lett.* **2012**, *12* (2), 569–575. https://doi.org/10.1021/nl204116b.

(121) Choi, H.; Jeong, S. A Review on Eco-Friendly Quantum Dot Solar Cells: Materials and Manufacturing Processes. *Int. J. of Precis. Eng. and Manuf.-Green Tech.* **2018**, *5* (2), 349–358. https://doi.org/10.1007/s40684-018-0037-2.

(122) Tamang, S.; Lee, S.; Choi, H.; Jeong, S. Tuning Size and Size Distribution of Colloidal InAs Nanocrystals via Continuous Supply of Prenucleation Clusters on Nanocrystal Seeds. *Chem. Mater.* **2016**, *28* (22), 8119–8122. https://doi.org/10.1021/acs.chemmater.6b03585.

(123) Yang, S.; Zhou, P.; Chen, L.; Sun, Q.; Wang, P.; Ding, S.; Jiang, A.; Zhang, D. W. Direct Observation of the Work Function Evolution of Graphene-Two-Dimensional Metal Contacts. *J. Mater. Chem. C* **2014**, *2* (38), 8042–8046. https://doi.org/10.1039/C4TC01613K.

(124) Shallcross, R. C.; Chawla, G. S.; Marikkar, F. S.; Tolbert, S.; Pyun, J.; Armstrong, N. R. Efficient CdSe Nanocrystal Diffraction Gratings Prepared by Microcontact Molding. *ACS Nano* **2009**, *3* (11), 3629–3637. https://doi.org/10.1021/nn900735y.

(125) Yang, M.-S.; Song, C.; Choi, J.; Jo, J.-S.; Choi, J.-H.; Moon, B. K.; Noh, H.; Jang, J.-W. Fabrication of Diffraction Gratings by Top-down and Bottom-up

Approaches Based on Scanning Probe Lithography. *Nanoscale* **2019**, *11* (5), 2326–2334. https://doi.org/10.1039/C8NR08499H.
(126) Fan, F.; Stebe, K. J. Assembly of Colloidal Particles by Evaporation on Surfaces with Patterned Hydrophobicity. *Langmuir* **2004**, *20* (8), 3062–3067. https://doi.org/10.1021/la030380c.
(127) Sánchez-Iglesias, A.; Grzelczak, M.; Altantzis, T.; Goris, B.; Pérez-Juste, J.; Bals, S.; Van Tendeloo, G.; Donaldson, S. H.; Chmelka, B. F.; Israelachvili, J. N.; Liz-Marzán, L. M. Hydrophobic Interactions Modulate Self-Assembly of Nanoparticles. *ACS Nano* **2012**, *6* (12), 11059–11065. https://doi.org/10.1021/nn3047605.
(128) Mohtasebzadeh, A. R.; Ye, L.; Crawford, T. M. Magnetic Nanoparticle Arrays Self-Assembled on Perpendicular Magnetic Recording Media. *International Journal of Molecular Sciences* **2015**, *16* (8), 19769–19779. https://doi.org/10.3390/ijms160819769.

APPENDIX A: COPYRIGHT PERMISSIONS

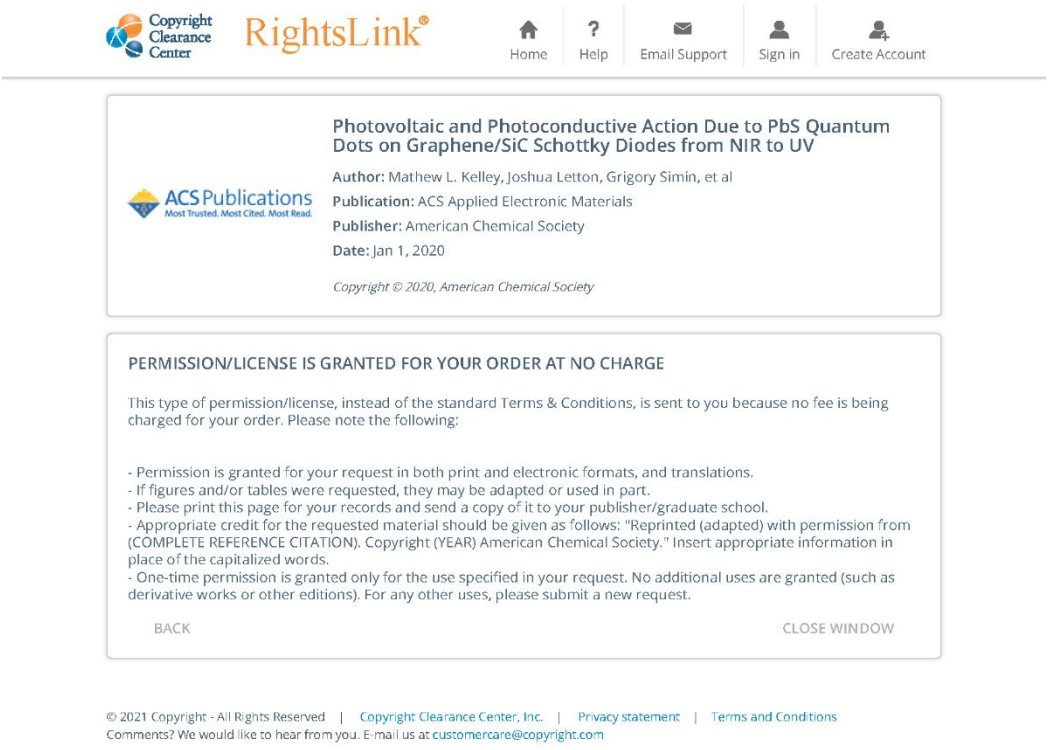

Copyright Clearance Center RightsLink®

Home | Help | Email Support | Sign in | Create Account

ACS Publications
Most Trusted. Most Cited. Most Read.

Photovoltaic and Photoconductive Action Due to PbS Quantum Dots on Graphene/SiC Schottky Diodes from NIR to UV

Author: Mathew L. Kelley, Joshua Letton, Grigory Simin, et al
Publication: ACS Applied Electronic Materials
Publisher: American Chemical Society
Date: Jan 1, 2020

Copyright © 2020, American Chemical Society

PERMISSION/LICENSE IS GRANTED FOR YOUR ORDER AT NO CHARGE

This type of permission/license, instead of the standard Terms & Conditions, is sent to you because no fee is being charged for your order. Please note the following:

- Permission is granted for your request in both print and electronic formats, and translations.
- If figures and/or tables were requested, they may be adapted or used in part.
- Please print this page for your records and send a copy of it to your publisher/graduate school.
- Appropriate credit for the requested material should be given as follows: "Reprinted (adapted) with permission from (COMPLETE REFERENCE CITATION). Copyright (YEAR) American Chemical Society." Insert appropriate information in place of the capitalized words.
- One-time permission is granted only for the use specified in your request. No additional uses are granted (such as derivative works or other editions). For any other uses, please submit a new request.

BACK CLOSE WINDOW

AIP PUBLISHING LICENSE
TERMS AND CONDITIONS

Jun 16, 2021

This Agreement between University of South Carolina -- Mathew Kelley ("You") and AIP Publishing ("AIP Publishing") consists of your license details and the terms and conditions provided by AIP Publishing and Copyright Clearance Center.

License Number	5090990026225
License date	Jun 16, 2021
Licensed Content Publisher	AIP Publishing
Licensed Content Publication	Applied Physics Letters
Licensed Content Title	Spatially resolved Fourier transform impedance spectroscopy: A technique to rapidly characterize interfaces, applied to a QD/SiC heterojunction
Licensed Content Author	Mathew L. Kelley, Grigory Simin, Kamal Hussain, et al
Licensed Content Date	May 31, 2021
Licensed Content Volume	118
Licensed Content Issue	22
Type of Use	Thesis/Dissertation
Requestor type	Author (original article)
Format	Electronic
Portion	Excerpt (> 800 words)
Will you be translating?	No
Title	COLLOIDAL SEMICONDUCTOR QUANTUM DOTS: SOLUTION PROCESSING AND HETEROSTRUCTURE-BASED OPTOELECTRONICS
Institution name	University of South Carolina
Expected presentation date	Aug 2021
Portions	Figures, text for chapter in thesis.
Requestor Location	University of South Carolina 3610 Timberlane Dr Apt E1 COLUMBIA, SC 29205 United States Attn: University of South Carolina
Total	0.00 USD